CELLULAR MECHANOTRANSDUCTION IN THE PATHOGENESIS AND TREATMENT OF CARDIAC FIBROSIS

By

Peter Adam Galie

A dissertation submitted in partial fulfillment
of the requirements for the degree of
Doctor of Philosophy
(Biomedical Engineering)
in the University of Michigan
2011

Doctoral Committee:

Associate Professor Jan Philip Stegemann, Chair
Professor James B. Grotberg
Professor Shuichi Takayama
Assistant Professor Margaret V. Westfall

To my wife and family,

For their love and guidance

Acknowledgements

I would first like to thank Dr. Jan Stegemann for giving me the opportunity to help him start his lab at the University of Michigan. He has been an exceptional mentor to me, and I have learned a tremendous amount from him. His lessons have extended beyond how to conduct sound and useful scientific research. Through his own example he taught me the importance of personal relationships in medical research, and how to successfully balance the duties of a faculty member with the responsibilities of a good husband and caring father. I am proud to tell people that I work for him, and I will miss being a part of his lab.

I would also like to thank my committee's mentorship and continuing support. Deciding to take Dr. Grotberg's fluid mechanics course was one of the best decisions I have made during my short academic career. He is proof that it is possible to make meaningful contributions to both biomedicine and mechanics. If I can achieve half of the brilliance he possesses, I will have a long and productive career. Dr. Westfall has also been an invaluable mentor for me during my time at Michigan. It is rare to find someone with her level of expertise in cardiac physiology that is willing to invest time and effort for the work of a biomedical engineer. Her dedication and passion for her work are qualities that I will try to emulate as I progress in my career. I also owe much to Dr. Takayama for his insightful comments about my research.

I am of course indebted to my family. My father has always been my foremost role model; his curiosity and ability to find, assess, and solve technical problems is what impelled me to become a scientist and engineer. He also raised me a Wolverine fan, which may have influenced my decision to come to Michigan. My mother gave me unconditional love and support as well as the mindset to take one day at a time, which has been vital during my pursuit of a Ph.D. My sisters, Gina, Jess, and Terry, have always set an example of hard work and excellence that I've tried to imitate. My grandparents have given me the perspective that family always comes first. I'm also grateful for my in-laws for taking a genuine interest in the work that I do.

I am most thankful for my wife, Nina. I am a better person because of her love and support. Her compassion and commitment to helping others inspired me to begin studying biomedical engineering while I was working for GE. I'm proud of all that she accomplished during our time in Michigan, including gaining such a high level of respect from the students, parents, and teachers at St. Thomas school. She is an extraordinary person, and I am very fortunate to be her husband.

Table of Contents

List of Figures

List of abbreviations

α-SMA: alpha smooth muscle actin
TGF-β: transforming growth factor, beta
VEGF: vascular endothelial growth factor
IGF-1: insulin-like growth factor 1
PDMS: polydimethylsiloxane
ARB: angiotensin II receptor blocker
AT1R: angiotensin II type I receptor
MSC: mesenchymal stem cell
DMEM: dulbecco's modified Eagle's medium
PBS: phosphate buffered saline
2D: two-dimensional
3D: three-dimensional
VAD: ventricular assist device

ABSTRACT

CELLULAR MECHANOTRANSDUCTION IN THE PATHOGENESIS AND TREATMENT OF CARDIAC FIBROSIS

By

Peter Adam Galie

Chair: Dr. Jan Philip Stegemann

Cardiac fibrosis occurs after myocardial infarction, and contributes to both systolic and diastolic heart failure. Activation of cardiac fibroblasts to a myofibroblast phenotype is essential for fibrotic scar development. The present dissertation focuses on this phenotypic transition, specifically on the effects of mechanical stress and interactions with mesenchymal stem cells (MSC). The experimental platform used was a flexible 3D culture well that allowed simultaneous application of fluid flow and cyclic strain to collagen type I hydrogels seeded with primary rat neonatal cardiac fibroblasts. The results indicated that fibroblasts transitioned to myofibroblasts in static culture in the absence of exogenous biochemical or mechanical stimulation. Interstitial fluid flow significantly stimulated the myofibroblast transition, while cyclic strain had an opposing effect. Using chemical antagonists and lentivirally-delivered shRNA, it was found that the acute response to flow was mediated by angiotensin II receptor type I (AT1R) and transforming growth factor β (TGF-β). Cyclic strain also influenced the TGF-β pathway by attenuating the phosphorylation of smad2, a downstream effector of this signaling pathway. The experimental results were augmented with a poroelastic model of flow and gel displacement within the collagen hydrogels, which indicated that cyclic strain produced substantial interstitial fluid flow in the absence of applied cross flow. The results of the analytical model, combined with the experimental findings, suggested that cyclic strain decreased fibroblast activation even in the presence of interstitial flow. Finally, GFP-labeled MSC were injected into the cell-seeded collagen hydrogels to examine their effect on the cardiac fibroblast response. The presence of MSC significantly attenuated cardiac fibroblast activation under both static conditions and during biochemical and mechanical stimulation. Hypoxia, not mechanical stress, induced the highest levels of MSC migration, as well as the highest release of the paracrine factor, VEGF. The data suggest that AT1R can be targeted to prevent the myofibroblast transition, due to its role in fluid shear-induced fibroblast activation. Additionally, the observed beneficial effects of cyclic strain may have implications for therapies that unload the myocardium, including the use of ventricular assist devices (VADs). Finally, the effects of MSC on fibroblast activation may illuminate the mechanisms of MSC-based therapies.

Chapter I

Introduction

The field of mechanobiology has gained increasing importance and clinical relevance in the last few decades as researchers and clinicians have continued to find evidence that cells convert exogenous mechanical stimuli into specific biochemical responses. The goal of the field is to discern these mechanically-sensitive signaling pathways in cells, so that interventions can be made to attenuate harmful cell responses to altered mechanics. Such mechanotransduction is clinically relevant because of the multitude of pathologies that are characterized by a change in the mechanical microenvironment. Certainly, one of the reasons for the accelerated growth of this field is its applicability to nearly every tissue in the body. For example, understanding the response of chondrocytes to compressive strain may yield insight into osteoarthritis. The same can be said for pulmonary epithelial cells response to fluid shear stress for emphysema, even cancer cells are influenced by the mechanical microenvironment of a tumor. But perhaps no tissue in the body is more mechanically relevant than the heart with its constant, cyclic deformation during systole and diastole. Though the comparison is made infrequently, there are more similarities than differences between a cardiac pressure-volume loop and an Otto cycle of the internal combustion engine. Due to its mechanical nature, it is intuitive that the cells within the heart are sensitive to changes in solid and fluid phase stress.

The research described in this dissertation mostly focuses on the mechanobiology of cardiac fibroblasts. Though cardiomyocytes take up the most volume of any cell type in the myocardium, there are actually more fibroblasts by number in the heart. Moreover, the crucial role of fibroblasts in cardiac architecture and physiology is increasingly being elucidated. Under

specific circumstances, fibroblasts in the myocardium transition to a myofibroblast phenotype that is characterized by increased contractility, extracellular matrix secretion, and the expression of prominent stress fibers within the cytoskeleton. Myocardial injury leads to activation of cardiac fibroblasts which causes scar formation and subsequent systolic or diastolic dysfunction in heart failure. Therefore, cells within the fibrotic myocardium are exposed to an altered mechanical environment, which may contribute to the growth of the fibrotic scar and eventual heart failure. The goal of the present dissertation is to study the response and mechanism of cardiac fibroblasts stimulated by fluid-induced and solid stress, so that treatments can be developed to attenuate the fibroblast activation that leads to scar development in the heart.

The approach of this research involved seeding cardiac fibroblasts within collagen hydrogels, which mimic the three-dimensionality of in vivo tissue. The cell-seeded gels were studied in conventional culture wells, as well as within a polydimethylsiloxane (PDMS) well designed to apply interstitial fluid flow, or cyclic strain, or a combination of both stimuli. To predict fluid flow, pressure, and the strain environment, the empirical research was supplemented with a numerical poroelastic model. Throughout these studies, the myofibroblast transition was quantified using a combination of contractility assays, message level analysis, immunofluorescence, and immunoblotting. The mechanisms for the cell response were discerned using several blocking agents, including a shRNA construct targeting a specific mechano-sensitive G-protein coupled receptor. Once the effect of culturing conditions and mechanical/biochemical stimulation on fibroblast activation was elucidated, the cell-seeded gel was used as an in vitro model of fibrosis to study the addition of mesenchymal stem cells to the fibrotic myocardium. MSCs were injected into the cell-seeded hydrogel to study the effect of mechanical stimulation on MSC paracrine release and its effect on surrounding fibroblasts.

The following chapters begin with pertinent background information for the research presented in later chapters. This background describes the current impact of heart disease, as well as a description of the current treatments for patients suffering from this affliction, including clinical trials involving stem cell injection. A short introduction of the physiology underlying fibrosis in the myocardium is also presented, along with a full explanation of the fibroblast to myofibroblast transition. This is followed by a description of the mechanical environment within the myocardium, both in healthy and fibrotic tissue. The background section concludes with a survey of previously published research conducted on the fibroblast and MSC response to mechanical stimuli. Then, a detailed methods section describes the culturing conditions of the cell-seeded gels in static culture as well as in the mechanically-stimulated PDMS wells. Assays to assess cell response and function are subsequently described. The results of the experiments are presented in graphical form with descriptive text, and the interpretation and analysis of the results and their significance is provided in the Discussion section.

Chapter II

Background

2.1 Heart failure: definition, epidemiology and treatment options

Heart failure is the end result for a broad range of different pathologies, and includes abnormalities in either cardiac structure, rhythm, or a combination of both. Heart failure is generally characterized into two categories: systolic and diastolic. Though both diseases result in reduced cardiac output, the structural differences and disease progression are distinctly different. In systolic dysfunction, an acute or chronic affliction decreases the contractility of the myocardium, as indicated by a reduction in the slope of the Frank-Starling curve. To maintain cardiac output, the volume of the left ventricle is increased by remodeling of the myocardium. Systolic dysfunction is characterized by an increase in myocyte length, which leads to eccentric hypertrophy. This compensatory mechanism eventually breaks down, and the cardiac output falls below acceptable levels. In diastolic dysfunction, the left ventricle is unable to sufficiently fill with blood. After the constant volume stage of diastole, complete filling relies on the ability of the myocardium to distend. If the wall is too stiff, the filling is inadequate and stroke volume decreases even though ejection fraction increases. Diastolic dysfunction is associated with an increase in myocyte width, which leads to concentric hypertrophy.

Differentiating between systolic and diastolic heart failure is further complicated by the fact that nearly a third of patients experience simultaneous systolic and diastolic dysfunction [McMurray, 2005]. Because ejection fraction can be preserved in diastolic dysfunction, it is much more difficult to diagnose clinically than systolic dysfunction. There is increasing evidence that the current understanding of systolic and diastolic dysfunction as distinct afflictions is

misleading; patients may transition between states of systolic and diastolic dysfunction prior to end-stage failure. However, one common factor in both systolic and diastolic dysfunction is the presence of fibrosis in the myocardium, as indicated by a study showing elevated levels of procollagens I and III in patients suffering from both types of heart failure [Barasch, 2009]. Hence, understanding the formation and growth of fibrotic scars is crucial to developing new treatments for heart failure.

The epidemiology of the disease is well documented, most likely due to its prevalence in both developed and developing countries. Nearly 2% of the adult population suffers from heart failure [McMurray and Pfeffer, 2005], and the incidence increases with age. Approximately 5.8 million people in the United States have been diagnosed with heart failure, with nearly 670,000 being added to that list per year [Lloyd-Jones, 2010]. What is perhaps most striking is the mortality associated with heart failure, with rates higher than many cancers for people admitted to the hospital [Baker, 2003]. A person in their forties has a 20% chance of being diagnosed with heart failure, and a 33% chance of dying within a year of that diagnosis [McMurray and Pfeffer, 2005]. The impact of heart failure on human life is tremendous and is motivation in itself for studying the disease, but its financial burden cannot be ignored. Nearly 2% of all health-care spending in a developed country like the U.K. is attributed to heart failure [Stewart, 2002]. In 2010, heart failure cost the U.S. $39.2 billion in health care services, medication, and lost productivity [Lloyd-Jones, 2010]. In 2007, the American Heart Association had a $700 million budget for research, public education, community programs, and advocacy. One can assume that these costs will only rise as the mean age of developed countries continues to rise in the next 10 to 20 years, considering that the incidence of heart failure for people over the age of 65 can increase by a factor of 5 [McMurray and Pfeffer, 2005].

Despite these grim statistics, treatments for all stages of NYHA-designated heart failure are continuing to increase in efficacy and availability. Traditionally, pharmaceutical intervention with inhibitors of the renin angiotensin system and β-adrenergic receptors have been effective for slowing the progression of heart failure and providing palliative relief for patients. The standard treatment for non-end stage heart failure currently involves some combination of beta-blockers, digoxin, diuretics, and inhibitors for the renin-angiotensin system, including ACE inhibition [Desai, 2011]. A recent argument has been made for inclusion of aldosterone receptor antagonists as well [Nappi and Sieg, 2011]. For patients in end-stage heart failure, ventricular assist devices are proving to be valuable and increasingly practical solutions [Gregory, 2011]. In addition, the use of adult stem cells holds great potential for treatment of heart failure, though the efficacy, mechanism, and delivery of this treatment are controversial subjects [Boudolas, 2009]. The following paragraphs will provide a brief review of current and future treatments: their advantages and caveats as well as their effect on fibrotic scarring in the myocardium.

Beta blockers act directly on β-adrenergic receptors, reducing both the chronotropic and positive inotropic effects of receptor activation. Originally, due to the decrease in contractility, these drugs were considered inappropriate for treatment of systolic dysfunction. However, they also act on β1 receptors in the kidney to reduce renin secretion, which provides an added benefit for patients of heart failure suffering from hypertension. Moreover, blocking β-adrenergic receptors also has anti-apoptotic effects [Liang, 2008; Amin, 2011]. Previous work has also indicated that beta-blockers normalize the turnover of beta adrenergic receptors, which is attenuated in heart failure. In this manner, beta-blockers can improve the beta adrenergic response of cardiomyocytes [Leosco, 2007]. Initial clinical trials featuring bisoprolol and metoprolol, selective β1 blockers without sympathetic activation or vasodilating properties, did

not find any significant improvement in reducing mortality [CIBIS II, MDI, 1999]. Nonetheless, the benefit of beta blockers is well established [Bangalore, 2007]. The only beta blocker designated by the FDA for treatment of heart failure is carvedilol, which has been shown to significantly reduce the progression of the disease [Packer, 1996]. More recent clinical trials have also established the benefit of beta blockers for treating various stages of heart failure [Klapholz, 2009]. Overall, the consensus seems to be that beta blockers are effective at interrupting the neurohormonal chain of events involved in disease progression, but not with any immediate symptomatic improvement. A recent study showed that spironolactone, an aldosterone antagonish, used together with a beta blocker significantly reduced cardiac collagen turnover in heart failure patients, indicating that these agents may also have anti-fibrotic effects in the myocardium [Cavallari, 2007]. Carvedilol also has been shown to reduce cardiac fibrosis up to 67% in rat models [Barone, 1998]. The mechanism for this benefit has yet to be elucidated.

Digoxin has been used for the treatment of heart failure for over 200 years. Though its exact mechanism is still unknown, it is theorized that by deactivating sodium/potassium ion channels, the intracellular concentration of sodium in cardiomyocytes is increased. Then through the calcium-sodium exchange channel, intracellular calcium concentration subsequently increases. This increase in calcium causes a highly positive inotropic effect on the heart, augmenting contractility of the myocardium and negating the need for left ventricular enlargement during systolic dysfunction. However, the drug is not without severe side effects, including toxic and mood-altering consequences at high concentrations. For example, a recent study has shown that dronedarone, a common antiarrhythmic medication, can increase digoxin concentrations in the blood when the two are taken in combination [Vallakati, 2011]. A genotyping study showed that females may actually be more susceptible to digoxin intoxication

[Neuvonen, 2011]. Moreover, one may assume that if it can change calcium concentrations in cardiomyocytes, it could do the same in cardiac fibroblasts. The role of increased intracellular calcium concentrations in cardiac fibroblast activation has been well-studied [Chen, 2010], and it is possible that digoxin could lead to augmented cardiac fibroblast activation and subsequent fibrosis. Due to its dangerous effects, the use of digoxin is currently being phased out of the clinical setting [McMurray and Pfeffer, 2005].

Drugs targeting the renin angiotensin system have been used progressively more in the past ten to twenty years to treat patients suffering from heart failure and in the aftermath of myocardial infarction. Their primary mode of operation is to reduce blood pressure, both by reducing total blood volume (preload) and preventing constriction of vasculature (afterload). They are often used in conjunction with antagonists for angiotensin II receptor blockers (ARBs), though in recent years there has been a debate to the effectiveness of "single" (without ARBs) versus "dual" (with ARBs) use [Messerli, 2009; McMurray, 2009]. The concern with using ARBs in conjunction with ACE inhibitors include renal dysfunction, hyperkalemia, and hypotension. However, the argument for dual use is based on two clinical trials and the recommendation that symptoms for the aforementioned side effects be monitored during treatment [McMurray, 2009]. In the past few years, the anti-fibrotic effect of ARBs has been increasingly elucidated. A recent study showed that telmisartan, a common ARB, significantly reduced fibrosis in rat models of chronic heart failure [Sukumaran, 2010]. Valsartan, another ARB, was found to reduce remodeling in the myocardium of hypertensive rats [Okada, 2006]. Yet, the mechanism by which these antagonists facilitate this anti-fibrotic effect is unknown.

If pharmaceutical intervention can be deemed "the first line of defense" against heart failure, then ventricular assist devices (VADs) would be the last line. The device does the work

of the ventricle by creating a pressure gradient to drive blood into the circulatory system. Blood can be propelled by pulsatile, axial, or centrifugal means [Scolletta, 2011; Moscato, 2009; Wu, 2010]. Though much progress has been made in the development and use of these devices, there are still substantial challenges facing the field. Issues with biocompatibility and thrombosis from platelet rupture persist [Alemo, 2010]. Moreover, there are also issues with right heart failure and the risk of kidney failure. The effect of VAD implantation on fibrosis is controversial. A recent study using a rat model found that unloading of the heart, by abdominal heterotopic heart transplantation, resulted in attenuated fibrotic scarring in the unloaded myocardium [Zhou, 2011]. However, a study involving human hearts unloaded by an LVAD found that microvascular density and fibrosis significantly increased [Drakos, 2010]. This study suggests that mechanical stress can modulate the fibrotic response in the myocardium.

Though the benefit of adult stem cell implantation in the myocardium has been established for some time, the mechanism and duration of this improvement is more controversial. In recent years, mesenchymal stem cells (MSCs) have been implanted into patients suffering from various myocardium-related pathologies including dilated cardiomyopathy, concentric hypertrophy, and myocardial infarction [Novotny 2008; Wang, 2010; Meluzin, 2009]. It has been hypothesized that the implanted cells regenerate tissue through paracrine effects [Gnecchi, 2008], cell fusion with damaged cells [Avitabile, 2011], as well as through differentiation into cardiomyocytes [Lu, 2010]. However, the extent to which damaged myocardium uses stem cell homing from the circulation as a repair mechanism is unclear, bringing into question the appropriateness of cell implantation. Moreover, there is a great deal of variability in the effectiveness of cell therapies. This could arise from the fact that patients receiving stem cell transplants from their own bone marrow may have comorbidity with diabetes,

high blood pressure, or another affliction that could affect the beneficial properties of the implanted stem cells. Nonetheless, studies have indicated that injected MSCs attenuate fibrosis in the response to myocardial infarction, by altering MMP and collagen production by cardiac fibroblasts [Mias, 2009].

Not only is the mechanism a source of debate, but the optimal mode of delivery has also yet to be identified. The two primary locations of MSC injection in the heart are directly into the myocardium (intramyocardial) and into the coronary artery (intracoronary). Both injection methods have demonstrated positive results, despite the common obstacle of cell engraftment within the fibrotic myocardium. An advantage of injection into the vasculature is distribution of any paracrine factors released by the stem cells to perfused tissue [Barallobre-Barreiro, 2011; Gyöngyösi, 2010]. Fibrotic regions of the myocardium may suffer from reduced blood flow when the occluded artery remains blocked [Germain, 2001], and a recent study has demonstrated intracoronary injection is associated with reduced blood flow following the treatment [Gyöngyösi, 2010]. The primary advantage of intramyocardial injection is the ability to localize the treatment directly to the fibrotic region. Cells injected in this manner often improve cardiac function through formation of new vasculature [Hu, 2008], and have even been associated with reduction of arrhythmias [Wang, 2010]. Using a rat model of IDC, it was found that intramyocardially injected MSC induced angiogenesis and myogenesis through direct differentiation into both vascular-associated cells and cardiomyocytes, as well as through the production of angiogenic, antiapoptotic, and mitogenic factors including VEGF, hepatocyte growth factor, adrenomedullin, and IGF-1 [Nagaya, 2005].

In addition to direct MSC injection, other methods of cell delivery to the heart have been investigated. For example, monolayers of cultured MSC without exogenous matrix support have

been grafted onto the surface of scar tissue in the myocardium [Miyahara, 2006]. The cells produced significant amounts of extracellular matrix components while in culture, and the implanted cell sheet produced a substantial amount of new tissue with evidence of angiogenesis. It was hypothesized that a major benefit of this extra tissue was to decrease overall wall stress on the damaged myocardium, but in other respects the monolayer technique produced similar effects as an injection method used for a similar injury model [Perin, 2003]. Both studies suggested that paracrine effects of the implanted MSC outweighed the benefit of direct differentiation into cardiomyocytes.

The concept of a cardiac patch seeded with MSC applied directly to the epicardium also has shown promise. The principle behind this technique is to deliver cells while they are seeded into the type of matrix they will encounter in the native environment of the heart. For example, a study using a Type I collagen patch populated with MSC found a significant improvement in heart function in rat infarction models [Simpson, 2007] without signs of rejection. However, the authors did not find any significant improvement in wall thinning. Another study used a polyethylene glycol-modified fibrin, a degradable material that allows the gradual release of MSC into the affected area [Zhang, 2008]. Using a murine post-infarct model, this patch was able to significantly improve the hemodynamic function of the heart, especially ejection fraction. A recent study used a portion of decellularized swine myocardium as a scaffold for a cellular patch seeded with bone marrow mononuclear cells [Wang, 2010]. Such patches attempt to reconstitute certain key aspects of the extracellular environment, but the effects of mechanical stresses on such materials have not been fully investigated. Moreover, how a patch would change electrical conduction and potentially contribute to arrhythmias are issues that must be addressed.

2.2 Introduction to the fibrotic myocardium

Fibroblasts in the myocardium are similar in structure and function to fibroblasts in other parts of the body; they produce vital components of the extracellular matrix, and by doing so maintain tissue structure and integrity. These cells also are able to take on a contractile, smooth muscle-like phenotype. In the adult heart, this transition occurs primarily during pathology and often facilitates the progression to heart failure. In a healthy adult myocardium, the ratio of myofibroblasts to fibroblasts is very low. Nonetheless, the distinction between these two phenotypes is not entirely clear. Though increased extracellular matrix (ECM) production and expression of smooth muscle alpha-actin are often utilized as markers of the transition (Figure 1), cardiac fibroblast phenotype comprises a continuous spectrum of states. Myofibroblasts exhibit a hybrid of smooth muscle cell and fibroblast properties, rather than being a completely distinguishable cell type. Studies have shown that both mechanical and biochemical stimuli can influence the location of the cell in this spectrum, and the pathways by which these cells transduce mechanical signals into biological changes have been extensively studied.

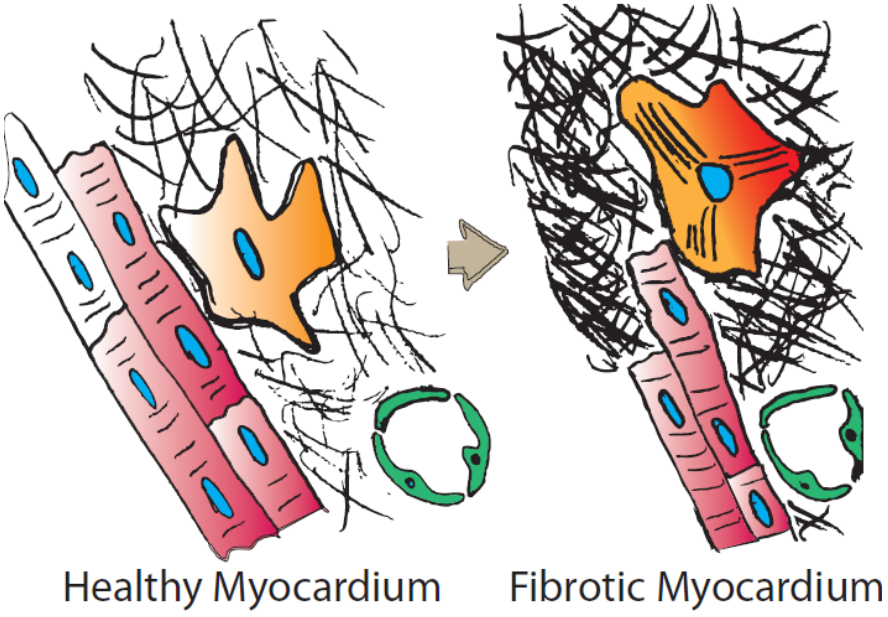

Figure 2.1 - **Fibroblast activation in the myocardium:** Fibroblasts transition to a myofibroblast phenotype and secrete a thick extracellular matrix and increase contractility.

The presence of a fibrotic scar, characterized myofibroblasts and a thick extracellular matrix, can be identified through several means. Traditionally, biopsies of myocardial tissue were taken to determine the extent of fibrosis. In the past 10-15 years, non-invasive approaches have been developed and refined, including measuring the presence of pro-fibrotic peptides in blood serum. Markers for collagen I and III production and degradation have shown to be useful in this approach [Díez, 2000]. Gadolinium-enhanced magnetic resonance imaging (GE-MRI) also provides a non-invasive assessment of the presence of fibrosis in the myocardium [Walcher, 2010]. Studies using this technique have correlated increased left atrial diameter and septum thickness with increased fibrosis [Prinz, 2011]. In patients suffering from dilated cardiomyopathy, the presence of fibrosis as quantified by GE-MRI correlated with decreased ejection fraction and increased deceleration time [Nanjo, 2009]. In a pig model of myocardial infarction, PET scans also revealed a decrease in ejection fraction and increases in both end-systolic and end-diastolic LV volumes [Teramoto, 2011].

Multiple pathologies can stimulate the formation of fibrosis in the myocardium. Fibrosis can arise from an acute event like a myocardial infarction, as well as from chronic pathologies including hypertrophic and dilated cardiomyopathies and myocarditis arising from infectious or toxic causes. As mentioned, studies have shown evidence that fibrosis exists in both systolic and diastolic heart failure. The pathogenesis of cardiac fibrosis for many of these pathologies is not fully understood, and there is evidence that it can be quite complicated. For example, in a study focused on a hypertensive animal model, the development of fibrotic lesions appeared to occur in two distinct phases: the first phase is a generalized process that includes the septum, and the second phase limited to localized areas in the myocardium [Herrmann, 1995]. Another study suggested that aldosterone and mineralocorticoid receptor, important factors in metabolic

dysfunction including hypertension and obesity, can mediate the presence of cardiac fibrosis [Essick, 2011]. The ubiquity of fibrosis in all of these different pathologies provides motivation for studying the cellular and molecular mechanisms underlying scar formation and homeostasis.

Studying cardiac fibroblasts in vitro provides a platform to elucidate these mechanisms, though their behavior in vitro can be quite different than in vivo, and depend upon culturing conditions. For example, cardiac fibroblasts isolated from tissue typically begin to spontaneously differentiate to a myofibroblast phenotype. Studies have shown that this transition may be related to increased activation of protein kinase A through the G protein coupled receptor – adenylyl cyclase – cAMP pathway [Swaney, 2005]. Moreover, fibroblasts appear to be sensitive to the concentration of serum used in the culture medium. Serum deprivation has been shown to not only affect the expression of SMA [Swaney, 2005], but also the viability and ECM production of cardiac fibroblasts [Leicht, 2001; Leicht, 2003]. Another recent study observed that the response of cardiac fibroblasts to cyclic mechanical loading depended upon the serum concentration of the culture media [Butt, 1997]. The data indicated that the cell response to cyclic loading was negligible when cultured in 1% FBS, but became significant in the presence of 10% serum. In this case, the cellular response was characterized by the amount of procollagen produced by the cells, as well as labeled thymidine incorporation as a measure of cell proliferation [Butt, 1997].

As these results indicate, understanding the relationship between mechanical transduction and the action of biochemical factors is vital to understanding the phenotype response of cardiac fibroblasts. Serum contains a host of growth factors that affect the cardiac fibroblast, so modifying serum concentrations does not indicate specifically what factors influence phenotype. Nonetheless, other studies have investigated how several growth factors, especially those associated with fibrosis, affect the response of cardiac fibroblasts to mechanical loading. For

example, angiotensin II is an important peptide in heart disease, since elevated levels are associated with fibrosis and heart failure [Fujita, 2008; Olson, 2008; Kawano, 2000; Thibault, 2001]. Studies have shown that not only are angiotensin II and other components of the RAAS system present in the myocardium, but also that static 20% strain initially reduces the expression of angiotensinogen, a key RAS substrate [Lal, 2008]. Hence, these results indicate that static stretch diminishes the presence of the myofibroblast phenotype, since angiotensin II is an important factor in this fibroblast myofibroblast transition. Moreover, it provides a clear example by which mechanical stimuli influences the biochemical environment.

Another important biochemical factor that affects the phenotype of cardiac fibroblasts is the oxygen concentration of the environment surrounding the cells. The change in oxygen concentration has been speculated as the impetus for the transition from fibroblasts to myofibroblasts in culture, since oxygen concentrations in surrounding tissue (~14%) are significantly less than the atmospheric conditions encountered once isolated (~21%). Moreover, hypoxic conditions can reduce oxygen concentrations to as low as 3% [Roy, 2003]. Cardiac fibroblasts respond to surrounding hyperoxic conditions through a specific signaling pathway involving induced p21, cyclin D1, cyclin D2, cyclin G1, Fos-related antigen-2, and TGF-beta [Roy, 2003]. This finding is non-intuitive because it indicates the myofibroblast transition is initiated by both hypoxia and hyperoxia. The authors of this study speculate that cardiac fibroblasts are able to reset their normoxic oxygen concentration to much lower levels in hypoxic conditions, so that a return to the 14% concentration is sensed not as a return to normoxia, but rather a hyperoxic condition. Hence, as the heart is reperfused, this triggers the myofibroblast transition. Further research by the group indicated that blocking this p21 associated pathway attenuates the expression of SMA, effectively maintaining a fibroblast phenotype even in the

presence of hyperoxic conditions [Roy, 2007]. Others have postulated that reactive oxygen species also play a central role in producing the myofibroblast phenotype. There is evidence that NADPH oxidase 4 is significantly upregulated in cardiac fibroblasts stimulated with TGF-beta, a growth factor known for its pro-fibrotic properties. Using si-RNA, the results suggest that production of reactive oxygen species by NADPH oxidase 4 is required for the fibroblast to myofibroblast transition [Cucoranu, 2005].

The importance of TGF-beta in the production of fibrosis in the heart as well as other tissues has been well documented; the following references [Brown, 2002; Liu, 2003; Wipff, 2007; Merryman, 2007] provide a cursory snapshot of the many studies conducted on this topic. In general, the growth factor works in various tissues to increase matrix production, stimulate the proliferation of myofibroblasts, and initiate other processes associated with fibrosis. Cardiac fibroblasts stimulated by TGF-beta have been shown to augment contraction of the gels compared to controls, with and without the presence of cardiotrophin-1 [Drobic, 2007]. This response is consistent with the ability of TGF-beta to promote the contractile myofibroblast phenotype, and shows that the effect of the growth factor is resilient to the presence of opposing factors. The augmented gel contraction has been repeated in another study, which showed that the extent of contraction was TGF-beta dose-dependent [Lijnen, 2003]. This study also showed that TGF-beta stimulated an increase in protein production by the cells, while the DNA content of cells was unchanged by TGF-beta [Lijnen, 2003]. However, another study utilized TUNEL staining to show that myofibroblasts stimulated by TGF-beta have increased DNA fragmentation and an inhibition of telomerase activity that halts cell proliferation, though the cells are non-apoptotic [Petrov, 2008]. Moreover, the effect of TGF-beta has shown crosstalk with the response of cells to angiotensin II [Chen, 2004]. Hence, the biochemical environment that

stimulates the transition from fibroblasts to myofibroblasts is complex - relying on multiple, related factors in addition to mechanical stimuli. These effects must be understood in order to evaluate the cell's response to mechanical loading.

An important component of both the biochemical and mechanical environments in tissue is the extracellular matrix (ECM), which also directly affects the fibroblast/myofibroblast phenotype. Studies have shown that specific elements of the ECM facilitate a transition to myofibroblasts. Though complex, the orientation of cardiac fibroblasts in the surrounding ECM is ordered and well-defined [Goldsmith, 2004]. The interaction between fibroblasts and the surrounding ECM is potentially as important as the relationship between fibroblasts and myocytes [Banerjee, 2006]. A study by Naugle et al showed that one component of the ECM, collagen type VI, is over-expressed in vivo after myocardial infarction. This protein attenuated cell proliferation in the presence of angiotensin II compared to collagens type I and III [Naugle, 2006]. The authors hypothesized that collagen VI produced this effect by stimulating a transition of fibroblasts to myofibroblasts, which are relatively non-proliferative. Not only does the matrix environment affect the cell biology, but the inverse is also true. Increased matrix production by the myofibroblast phenotype alters the structural and mechanical properties of the matrix. A recent study found that not only is the quantity of matrix production augmented in hypertensive heart failure, but the quality of this production is also affected. An imbalance in matrix metalloproteinases and tissue inhibitors of these enzymes were found in these tissues, indicating that pathology alters the pattern of collagen deposition [Lopez, 2006].

Several in vivo studies utilizing animal models have been conducted to further investigate the cardiac fibroblast to myofibroblast transition. As will be discussed in the following chapter, the mechanical environment in the heart is complex and varies both spatially and temporally.

Thus, although in vitro studies provide insight into the effects of specific stimuli on cell function, they cannot fully mimic the in vivo microenvironment as effectively as an animal model. One study in particular combined both in vivo and in vitro approaches. To assess the cell behavior of the myofibroblast phenotype, cells were isolated from pig models of left ventricular failure and cultured to assess their adhesion, migration, and release of fibrillar collagens and matrix metalloproteinase-2 [Flack, 2006]. Results of multiple animal studies have given insight into the mechanisms underlying the myofibroblast transition through knockout and transgenic models. For example, a tumor necrosis factor-alpha (TNF-α) null mouse model presented reduced cardiac fibrosis in a pressure overload model [Sun, 2007], indicating the role of this cytokine in the fibrotic response. The role of TGF-β has also been confirmed with an animal model; a transgenic mouse overexpressing the growth factor responded differently to β-adrenergic signaling [Rosenkranz, 2002]. These studies are just a select few examples of animal models that provide insight into the fibroblast to myofibroblast transition.

2.3 The mechanical microenvironment of the myocardium

In order to understand the role of mechanics in the myofibroblast transition, it is necessary to first characterize the mechanical environment in the in vivo myocardium, and how these mechanics are affected by fibrosis. Despite the health of the myocardium, cardiac fibroblasts are exposed to a complex mechanical environment that includes tensile, compressive, and shear stresses. These stresses are exerted by the contraction of surrounding cardiomyocytes, interaction with the microstructure of the extracellular environment, as well as interstitial fluid flow from perfusing vasculature. Due to the anisotropy and dynamic nature of the heart, these stresses vary both spatially and temporally, and are coupled with one another. Due to the complexity of the mechanical milieu in the heart, computational and analytical modeling is an important tool in

studying both the cell and tissue behavior of the myocardium. Experimental approaches to measuring strains in the heart have also been developed [LeGrice, 1995], though such experiments are technically challenging.

Nonetheless, a substantial amount of work has studied the complex structure of the myocardium, which is one of the primary determinants of the stress state. The structure of mammalian heart tissue is largely anisotropic, yet highly ordered. The wall consists of repeating laminar sheets, each approximately four myocytes thick [LeGrice, 1995]. The myocytes within each lamina are connected through intercalated disks, which contain both gap junctions and desmosomes to link adjacent cells electrically and mechanically. These branching muscle fibers are surrounded by fibrillar extracellular matrix proteins like collagen I and III, as well as fibroblasts and the endothelial cells of capillaries. The myocytes branch between lamina, but these connections are less frequent. This affects the mechanics of the heart in addition to how the wall is electrically depolarized. The existence of discrete lamina causes significant shear to adjacent layers, and causes the conduction velocity to be two to three greater along the plane of the lamina compared to the transverse plane [LeGrice, 1995]. Collagen fibers also connect adjacent layers, though these fibers are often thin and uncoiled, allowing for shear strain [Harrington, 2005; Arts, 2001].

The overall architecture of the lamina is also ordered. The myocardium exhibits subtle differences between fiber orientation within the sheets and the orientation of the sheets themselves with respect to an orthogonal coordinate system. Fiber angles vary from –60 degrees at the endocardium to +60 degrees at the epicardium, creating a helical pattern to the radial direction of the wall [Harrington, 2005]. However, the sheet angles of the lamina are restricted to either -45 or +45 degrees, and alternate depending upon the location of the sheet in the

myocardium [Harrington, 2005]. Because the sheet orientations are alternating, the lamina slide along one another in different directions even though the magnitude of the shear deformation is uniform across the wall. This leads to thickening of the wall in systole. Interestingly, research has indicated the orientation of these sheets aligns with planes of maximum shear strain [Arts, 2001]. During systole the healthy heart produces ejection fractions of 60-70%, which is accompanied by radial thickening of the heart wall of around 40%. However, the maximum contraction of an individual myocyte is limited to approximately 15% [Harrington, 2005]. Unfortunately, there has not yet been a study to determine the approximate strain on a cardiac fibroblast. The discrepancy in dimensional changes is thought to be a result of the shear exerted by slip between lamina in the myocardium, which contributes the orientation of the cells within the sheets.

Fibroblasts in the myocardium are also exposed to substantial fluid stresses from interstitial fluid flow [Lorenzen-Schmidt, 2006; Dvir Tal, 2007; Sinay, 1989; Ashikaga, 2008]. Because of the large deformation of the heart wall during the cardiac cycle, the interstitial fluid undergoes substantial flux and consequently exerts a pressure and shear force on cells within the myocardium. The fluid balance within the myocardium is controlled by the perfusion of the coronary artery and corresponding microcirculation as well as by lymphatic drainage that transports the products of cell metabolism [Mehlhom, 2001]. The factors that control fluid balance are strongly dependent on one another. For example, the pressure of the interstitial fluid is a regulator of the rate of perfusion. This effect is manifested during systole, when perfusion in the coronary capillaries is impeded due to the high pressure existing in the contracting myocardium. In addition, the myocardium separates two different bodies of fluid: the endocardium surrounds the blood-filled lumen, and the pericardial fluid surrounds the

epicardium. Consequently, there is a pressure gradient in the radial direction of the myocardium that may influence interstitial fluid flow [Lee, 2004].

The cardiac mechanical environment is strongly affected by, and may be contributing factor to, the damaging effects of various pathologies. Many of the pathologies affecting the heart, including acute infarction, dilated cardiomyopathy, and others are associated with changes in the extracellular matrix. These conditions affect the interaction between the sheets of cardiomyocytes and consequently the stresses exerted on resident cells like fibroblasts. In the case of acute myocardial infarction, the heart progresses through ischemic, necrotic, fibrotic, and remodeling phases that are each characterized by different mechanical properties [Holmes, 2005]. The necrotic phase is characterized by edema, which affects transport of the interstitial fluid within the myocardium. During the fibrotic phase, the mechanics are influenced by excess collagen, the cross-linking of which changes the mechanical environment during remodeling [Holmes, 2005]. In a canine model of infarction, researchers found that the twisting motion of the heart during systole was significantly reduced by fibrosis, indicating a substantial change in cardiac mechanics [Wang, 2009]. Other studies have found that the wall stress increases with the size of a remodeling left ventricle, indicating that excess collagen increases the stress on cells in the myocardium [Aikawa, 2001]. The studies in the present dissertation determine the extent to which cardiac fibroblasts respond to mechanical stress, in order to ascertain whether the changes in the mechanical microenvironment during pathology affect fibroblast phenotype.

Recent studies have focused on computational modeling of the mechanical environment experienced by cells in the myocardial wall. However, similarly to the experimental approach, modeling is made difficult by the complex microstructure of the tissue. Hence, validation of these computational models is also a substantial obstacle, though some empirical data is

available [Arts, 2001]. Moreover, the tissue undergoes finite, time-dependent deformation that depends upon interaction between the fluid mechanics of blood in the lumen as well as interstitial flow within the tissue and the structural mechanics of the heart wall. Nonetheless, useful models have been constructed for elucidating the stresses applied to cells in the heart wall. For example, one recent model utilizes an arbitrary Lagrangian-Eulerian reference frame to model the fluid-structure interaction present in the heart. Using finite element analysis, this study estimated the stress in the left ventricle wall, and confirmed the thickening of the wall during systole [Watanabe, 2004]. In another study, a model was created to predict the planes of maximum shear strain in the heart lamina [LeGrice, 1995]. Although complex, such modeling is necessary to complement empirical studies to discern the exact mechanical environment surrounding cardiac fibroblasts in the heart, and how these mechanics change with pathology.

2.4 Fibroblast response to mechanical stress

As with many biological systems, a feedback loop exists in the cardiac fibroblast response to loading. Mechanical stress affects the cell phenotype, which in turn alters the surrounding ECM, modifying the applied mechanical stress. This feedback is amplified in pathologies like fibrosis; a pathological stimulus causes fibroblasts to transition to myofibroblasts, these cells deposit greater amounts of ECM, and the ECM enlarges and stiffens. This change in the ECM further increases the stresses exerted on the cells. Understanding how cardiac fibroblasts respond to loading can affect the development of treatments for these diseases. Furthermore, understanding how to prevent this positive feedback can enable physicians to impede or prevent heart failure. This section will address key results from these recent studies which involve in vitro mechanical testing of isolated cardiac fibroblasts, with an

emphasis on studies that elucidate how cardiac fibroblasts respond to stress, and how these responses are relevant for the treatment of cardiac pathologies.

Early studies on the mechanobiology of cardiac fibroblasts utilized various flexure units able to apply axial or biaxial strain to cells attached to a 2D substrate. One such study applied 10 and 20% static strain to cardiac fibroblasts isolated from adult rats, which were cultured in 10% serum media. The cells were plated on a 2D silicone substrate coated with fibronectin. 2D biaxial strain of these substrates was associated with early activation of G proteins in the cardiac fibroblasts, and the rate of activation was dependent upon the strain rate utilized to stimulate the sample [Gudi, 1998]. Although this result does not point to a specific signaling pathway, it demonstrates the ability of the cardiac fibroblasts to transduce mechanical stimuli into specific biological responses. In a related study using similar mechanical stimulation, the authors found that static, biaxial strain increased levels of TGF-beta produced by the cells [Lee, 1999], suggesting a shift toward the myofibroblast state. Other modes of 2D stimulation have been used, including magnetic beads coated with collagen to apply static stresses of 0.65 pN/μm2 to determine α-SMA expression [Wang, 2000]. Studies have indicated that static and cyclic strain produce different responses. For example, cyclic stress produced significant amounts of IGF-1, another pro-fibrotic growth factor, while static stress did not have this effect on cultured cardiac fibroblasts [Hu, 2007].Several recent studies have investigated the effect of ECM composition on the cellular response of cardiac fibroblasts to mechanical loading. For example, one study applied 2D static strain to cardiac fibroblasts isolated from neonatal rats and cultured in 15% serum on laminin substrates, and found that cytoskeletal arrangement was significantly affected [Fuseler, 2007]. In a related study, mechanical stretch increased activation of MAP kinase when cells were plated on collagen and fibronectin compared to cells plated on aligned collagen and

laminin [Atance, 2004]. The results also indicated a difference in collagen type I deposition depending on the ECM component utilized. Although the authors of the study did not directly evaluate whether the static stretch promoted a transition to myofibroblasts, they did find that strain reduced proliferation rates, a characteristic of myofibroblasts. These results underscore the importance of the ECM on cardiac fibroblast response to mechanical loading, and vice versa. For example, a recent study showed that cyclic loading affected the type of ECM produced by the cells. 2D cyclic strain was applied to cardiac fibroblasts isolated from adult rats cultured in varying serum conditions. The authors found that both serum concentration and magnitude of strain affected the amount of collagen type I and III expressed by the cells [Husse, 2007].

Several studies have begun to focus on specific signaling pathways associated with cardiac fibroblast mechanotransduction. In a study utilizing magnetic beads to apply strain to cells, authors investigated the role of a Rho-Rho kinase pathway in increasing expression of α-SMA in stretched cardiac fibroblasts [Zhao, 2007]. Other studies have found that mechanical stretch is involved with specific changes in gene transcription, and activation of several protein kinases [Liang, 2000; Prante, 2007; Wang, 2005]. Moreover, other studies have elucidated the role of ion exchange and ion channels in the response of cardiac fibroblasts to mechanical loading [Raizman, 2007; Chilton, 2005]. This body of work contributes to our understanding of the specific mechanisms by which cardiac fibroblasts transduce mechanical stimuli into biological changes. However, most of this work was performed in two-dimensional culture systems that do not fully recreate the three dimensional nature of the loading experienced by cells in vivo.

Though fewer in number, there have been several studies focused on the effects of 3D mechanical loading on cardiac fibroblasts. A study analyzing the response of cardiac fibroblasts

to static stretch in a 3D environment supported the results of earlier studies that found attenuated myofibroblast transition [Poobalarahi, 2006]. Static 3D stretch reverted myofibroblasts to fibroblasts, reducing the expression of SMA and attenuating collagen and fibronectin production, two hallmarks of the myofibroblast phenotype. Hence, static strain is an example of a stimulus that is not affected by dimensionality. Other studies have examined how cardiac fibroblasts compact three-dimensional hydrogels, finding that the morphology of the cells depends on whether the gels are free to compact or restrained [Baxter, 2008]. Another method of recreating the 3D environment is to use trabecula isolated directly from heart tissue. One study utilized this method and found that cyclic loading increased the size of the trabecula compared to control, which can be interpreted as a model of cardiac hypertrophy [Bupha-Intr, 2007]. However, the specific behavior of the fibroblasts in this testing setup is not clear.

The majority of studies investigating cardiac fibroblast mechanobiology focus on normal stress, but shear stress is also a crucial component of the mechanical environment in the myocardium. The lamina of the myocardium experience significant sliding, which generates shear stress on the cells contained within these layers. Moreover, interstitial fluid flow also imparts shear stress on the cells in the myocardium. In conditions of ischemia following myocardial infarction, interstitial fluid flow in the scar environment is most likely substantially different than healthy myocardium, though this change has never been quantified. Shear stress has been shown to affect fibroblasts isolated from skin [Ahamed, 2008] through the release of TGF-beta. While there is not a similar study published using cardiac fibroblasts, bioreactors have begun to provide a platform for studying the effects of perfusion on tissue engineered cardiac constructs [Brown, 2008]. To address this gap in mechanobiology knowledge, studies in

this dissertation characterize the influence of fluid flow on fibroblast differentiation in a 3D environment.

2.5 Mesenchymal stem cell response to mechanical stress

For the purposes of cell therapy, it is also necessary to understand how mesenchymal stem cells respond to the mechanics of the healthy and fibrotic myocardium. However, the question of how MSC will respond to the mechanical environment when implanted into the myocardium depends strongly on the mode, location, and timing of delivery, as well as on the pathology being treated. Because of the complexity of the in vivo environment of the heart, most studies of mechanical stimulation of MSC to date have relied on in vitro culture models, which provide a more controllable setting for studying specific stimuli. Nonetheless, valuable and insightful information can be obtained by studying the effects of specific loading modes on MSC phenotype. The effects that have been studied include changes in cell phenotype and proliferation, as well as the secretion of antiapoptotic, angiogenic, mitogenic, and other factors. As mentioned, the current consensus is that MSC secrete paracrine factors once implanted in the myocardium. By understanding how the mechanics of the environment affect this paracrine release, the variables involved with MSC injection (location, timing, etc) can be optimized.

Similar to cardiac fibroblasts, two-dimensional culture of MSC on deformable substrates has provided insight into how these cells are affected by mechanical signals. Cyclic tension has been found to have a strong effect on several aspects of MSC phenotype. Exposure to 10% cyclical, uniaxial tension at 1 Hz for 7 days causes the actin cytoskeleton of bone marrow progenitor cells to align, impedes proliferation, and increases expression of α-SMA and calponin [Hamilton, 2004]. These results suggest differentiation into a smooth muscle cell (SMC)

phenotype rather than a cardiomyocyte lineage. Such experiments have been repeated on both collagen and elastin substrates, and it was shown that exposure of MSC to two-dimensional uniaxial strain increases the production of α-SMA and other SMC-type markers [Park, 2004]. In another study, equibiaxial strain caused an increase in proliferation of MSC [Song, 2007]. These varying responses suggest that MSC phenotype is dependent upon the type of mechanical loading. The observed differentiation toward the SMC phenotype in a subset of these studies suggest that the primary benefit of implanted MSC may be formation of new vasculature, as confirmed by multiple in vivo studies.

Three-dimensional cultures of MSC embedded in protein matrices also have been used to study mechanical effects on cell phenotype. In particular, MSC embedded in 3D collagen Type I matrices have been subjected to both uniaxial or biaxial strains. One study found that MSCs formed multicellular units in response to cyclic strain [Doyle, 2009]. In another study, a construct seeded with MSC was exposed to either 10% or 12% strain at 1 Hz for four hours a day for a week and the cells produced significant levels of bone markers such as bone morphogenetic protein 2 [Sumanasinghe, 2006]. An osteogenic response was also observed in another study using a similar type of construct for a wider range of strain values [Farng, 2008], and also in a study in which MSC were seeded on a synthetic polymer scaffold and exposed to cyclic compression [Duty, 2007]. These studies did not assess markers of the cardiomyocyte or smooth muscle cell phenotype, but their results are aligned with the observed presence of bone markers in an in vivo study of implanted MSC [Breitbach, 2007]. These studies imply that 3D culture in collagen matrices under mechanical loading can promote osteogenic differentiation in MSC. However since the majority of in vivo studies indicate a beneficial effect, more research is needed to determine the difference in these 3D in vitro models and the in vivo myocardium.

The effect of fluid stresses on MSC in 3D environments has not been extensively studied, but is an important area of investigation if these cells are to be transplanted to the heart. Studies of embryonic stem cells exposed to fluid shear showed that these cells differentiate to endothelial cell types, as evidenced by the expression of von Willebrand factor [Wang, 2005]. In a study focused on MSC, cells were plated on two-dimensional surfaces and exposed to pressure dominant, shear dominant, and combined constant, fluid stresses. It was found that fluid shear and compressive stress individually and in combination led to the expression of smooth muscle cell-like markers, including α-SMA and smooth muscle myosin heavy chain [Kobayashi, 2004]. This study did not examine the presence of any cardiac specific markers, though the resulting cell morphology resembled the smooth muscle phenotype. A recent study did analyze the effects of perfusion in a 3D scaffold, and found that flow affected MSC morphology and cell interactions [Zhao, 2009].

The effects of combined fluid shear stress and cyclical tension on MSC phenotype also have been investigated. In a study aimed at developing engineered heart valves using MSC seeded in a three-dimensional polymeric scaffold, it was found that cell response was dependent upon the type of loading: flexure, fluid shear, or combined loading. Under combined loading, MSC were responsible for a 75% increase in collagen deposition on the polymeric substrate. Moreover, the cells tested positive for such endothelial markers as CD31, laminin, and von Willebrand factor [Englemayr, 2006]. In another example of combined loading, MSCs were seeded on the lumen of a silicone tube and exposed to both 5% radial distention and a shear stress of 1 Pa at a frequency of 1 Hz. The MSC on the silicone tubes aligned in the direction of the flow as endothelial cells would, though they expressed SMC markers including α-SMA and calponin [O'Cearbhaill, 2008].

The mechanical properties of individual MSC also have been examined. Using a micropipette aspiration technique, it was found that these cells are inherently viscoelastic, and that the mechanical properties are strongly dependent upon the organization of the actin cytoskeleton. These properties were fit to a linear viscoelasticity model of the cells, which can be used for future modeling studies [Tan, 2008]. The study, which used temperature to modulate cell mechanical properties, provides motivation to examine how the mechanics of the cells changes with other factors relevant to implantation into the myocardium. For example, understanding how mechanics changes in the presence of different biochemicals as well as attenuated oxygen concentrations would be useful for cardiac applications. Research has shown that MSCs exposed to hypoxic conditions have been more successful in implantation [Hu, 2011], but the mechanism behind this phenomenon is not clear. The studies of the present dissertation test the relationship between oxygen concentration and cell mechanics to determine whether the success of cell transplantation is dependent on cell mechanics.

2.6 Hypothesis and Specific Aims

This dissertation focuses on the effects of mechanics on cells within fibrotic tissue, specifically fibroblasts and MSCs injected into the myocardium for cell therapies. The overall motivation of this work is to understand both the cell response, as well as the mechanisms by which the cells respond, in order to direct treatment strategies for attenuating fibrotic scar growth and eventual heart failure.

There are two distinct hypotheses for this work. First, mechanical strain and interstitial flow modulate the myofibroblast transition through a mechanism involving TGF-β signaling. Second, the presence of MSC dictates the myofibroblast transition through release of cardioprotective and angiogenic paracrine factors. It has been clearly demonstrated that cells are

affected by mechanical stress, but the significance of the present work is determining the underlying mechanism of this response using a system able to apply both fluid and solid stress to the cells in a three-dimensional environment. Although the in vitro system used in this work does not fully mimic the in vivo scar microenvironment, it provides a platform to study cell responses to specific elements of exogenous mechanical and biochemical stimuli. By understanding the mechanism of this response, treatments can be designed to block or stimulate these molecular actions to inhibit excessive myofibroblast transition and stimulate MSC paracrine release.

The specific aims are the following:

SA1: Characterize the response of cardiac fibroblasts to the stiffness environment of static collagen hydrogels, determining if the phenotype shift in 2D described in literature is repeated in 3D.

SA2: Design and construct an apparatus capable of simultaneously applying cyclic strain and interstitial fluid flow through the cell-seeded collagen hydrogel.

SA3: Identify the mechanisms responsible for the fibroblast response to the stimuli stated in SA2 using specific agonists and antagonists as well as lentivirally-delivered shRNA constructs.

SA4: Supplement the experimental results with an analytical model to predict relative fluid velocities and pressures within the hydrogel during operation, in order to explain cell responses to applied mechanical loading.

SA5: Inject mesenchymal stem cells into mechanically stimulated cardiac fibroblast-seeded gels, and determine the response of both the mesenchymal stem cells using tests for stem markers, cell motility, and paracrine release as well as the fibroblasts, using immunofluorescence and quantitative RT-PCR.

The results of these studies, which were performed in the order presented above, are summarized in the following chapters. Each subchapter in the Results and Discussion chapters are devoted to a specific aim. Chapter III details the materials and methods used for each of the studies, again in the order provided by the specific aims. Chapter IV presents and describes the results of these experiments, while Chapter V provides a discussion of how these results conform to the stated

hypothesis. The Appendices list specific protocols that can be used to repeat the experiments, a manuscript detailing a related project focusing on the adult cardiomyocyte response to stiffness, and detailed statistical analysis of the results.

A graphical description of the dissertation organization is provided below in Figure 2.2. The document begins with preliminary work to understand the effect of serum and stiffness on the transition of cardiac fibroblasts to a myofibroblast phenotype. After learning the correct culture conditions for stimulating the transition in static culture, the PDMS well was used to study the transition in dynamic, mechanically-stimulated culture. The poroelastic model provided insight into why cells responded differently to disparate modes of mechanical stimulation. Finally, MSCs were injected into the gel to study the effect of this coculture on the fibroblast transition.

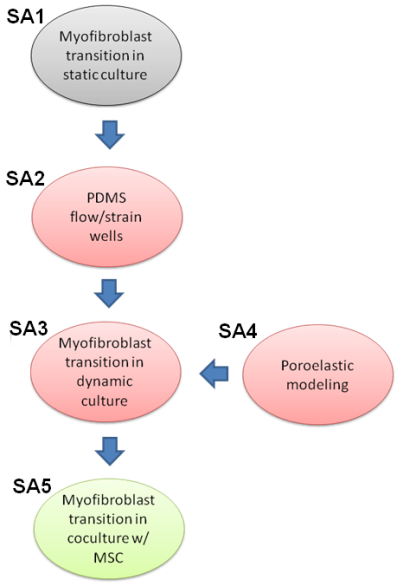

Figure 2.2 – **Dissertation roadmap**: The project is organized chronologically (from top to bottom) into the five specific aims previously described. Specific aims 3 and 4 were investigated simultaneously.

Chapter III

Materials and Methods

3.1 Experimental Methods

3.1.1 Cell Isolation and Culture

Cardiac fibroblasts were isolated from the ventricles of 2-3 day old Sprague-Dawley rats using a previously described enzymatic digestion protocol [Zlochiver, 2008]. This procedure is approved by the Institutional Animal Use and Care Committee at the University of Michigan and is in compliance with the *Guide for the Care and Use of Laboratory Animals* published by the National Institutes of Health. Briefly, minced ventricles were digested in 0.125% trypsin and 0.15% pancreatin (Sigma-Aldrich, St. Louis, MO) at 37 °C in consecutive 15-minute steps. Fibroblasts were separated from myocytes in a pre-plating step. After one day of culture in M199 supplemented with 10% FBS, fibroblasts were trypsinized and transferred and cultured in either low serum (5% FBS) or high serum (10% FBS) M199 or DMEM culture medium. Cells were cultured for one week with media changes every two days prior to use in experiments. The cells were then trypsinized and seeded in collagen constructs. For experiments involving both mechanical stimulation and MSC paracrine analysis, cells were cultured in 5% FBS.

3.1.2 Fabrication of Collagen Hydrogels

Collagen hydrogels were created in different molds and volumes depending on the specific experiments. For example, to study the effect of substrate compliance on cardiac fibroblasts in culture, released and constrained collagen gels were prepared in 24-well plates.

Both acellular and cellular gels were prepared in PDMS molds for mechanical testing. Regardless of the application, the fabrication and formulation of these gels were kept constant. Cardiac fibroblasts were seeded at a concentration of 5×10^5 cells/ml in a gel composed of 2.0 mg/mL acid solubilized bovine collagen type I (MP Biomedicals, Solon, OH), 10 % FBS, DMEM, and 0.1 M NaOH at physiological pH. Gels were incubated at 37 °C in a humidified 5% CO_2 incubator to initiate polymerization, before culture medium was added to the polymerized gels.

3.1.3 Gel Compaction Assay

For the released and constrained gels, individual 1.0 ml gel aliquots seeded with cells were poured into a 24-well plate, and gels were cultured in either low or high serum. Released gels were removed from the sides and bottom of the well plate with a thin spatula at the end of the 1 h polymerization step. Culture dishes were incubated at 37^oC in a humidified incubator with 5% CO_2. Samples were taken at 6, 24, 48, and 120 hour time points. The gels for the 120 hour time points were given new media at 48 hours. To measure compaction, released gels were removed from their well plates at the prescribed time points, and transferred to a sterile platform. The cylindrical constructs and an adjacent optical scale were photographed from transverse and longitudinal angles. These images were imported into ImageJ software, where volume calculations were computed. The same gels used for the compaction assay were then homogenized for quantitation of message RNA levels by qRT-PCR .

3.1.4 Mechanical testing of released collagen gels

Released gels removed from the 24 well plate at the prescribed time points were transferred to a compression platen. A uniaxial mechanical testing system (Test Resources, Shakopee MN) was used to measure stress and strain at room temperature. All samples were pre-

stressed to 10% strain at a rate of 30% strain/s and then relaxed prior to data acquisition. A strain rate of 30%/s to 30% strain was used to evaluate the static elastic properties of each gel. For the dynamic mechanical analysis, a 10% strain magnitude of 1.0 Hz frequency was used to determine the phase angle shift between applied strain and measured stress on the hydrogel. Data was then analyzed using MATLAB software to determine phase angles.

3.1.5 Quantitative Reverse Transcriptase Polymerase Chain Reaction (qRT-PCR)

To isolate mRNA from the cells, a guanidium thiocyanate-phenol-chloroform extraction protocol (TRIzol, Invitrogen Inc.) was used. Briefly, 1 mL gels seeded with fibroblasts were homogenized in 200 μL of TRIzol, followed by the addition of another 800 μL of TRIzol to completely dissolve the constructs. mRNA was further purified with chloroform, precipitated and washed with isopropanol, washed with ethanol, and dissolved in RNAse free water. Reverse transcription of mRNA was carried out with a high-capacity cDNA Archive kit (Applied Biosystems, Foster City, CA) in combination with a C-1000 Thermocycler (Bio-Rad, Hercules, CA). Quantitative PCR was then performed using TaqMan gene expression assay kits (Applied Biosystems, Foster City CA), using two pre-designed primers (Table 1) and one probe each for collagen type I and III, TGF-β, and α-SMA, and the housekeeping gene GAPDH using a 7500 Fast Sequence Detection system (Applied Biosystems, Foster City CA). Collagen type 1 and type III were targeted because they are the most prevalent extracellular matrix proteins in the myocardium [Baudino, 2006]. TGF-β is a known pro-fibrotic growth factor, and has been shown to mediate the transition to myofibroblast phenotype in response to interstitial flow [Ng, 2005]. α-SMA is a commonly used as a marker for the myofibroblast phenotype that plays a role in the contractile apparatus of cells. Data is expressed in fold change relative to GAPDH, and was calculated by taking the difference in cycles to threshold between the target gene and GAPDH

(ΔC_T), subtracting the difference from the ΔC_T of an initial data set to create a double normalization ($\Delta\Delta C_T$). The fold change was calculated from this parameter as $FC = 2^{-\Delta\Delta CT}$. Duplicates of each sample were analyzed.

3.1.6 Immunocytochemistry

A parallel group of released and constrained gels seeded with fibroblasts were analyzed to assess the transition to myofibroblasts by immunocytochemistry. These gels were fixed in 3.7% paraformaldehyde (Sigma-Aldrich) for 10 min at room temp, washed with PBS, and permeabilized in 0.2% Triton X-100 (Sigma-Aldrich) for 10 min. Gels were then incubated in PBS containing 1% goat serum (Invitrogen, Carlsbad, CA) , fluorescent DAPI (1:50), phalloidin conjugated to Texas Red (Invitrogen; 1:50) and monoclonal anti- α-SMA conjugated with FITC (Sigma-Aldrich; 1:200) for one hour at 37 °C. The DAPI stained the nucleus of the cells and phalloidin targeted the F-actin of the cytoskeleton. Cells were visualized using confocal microscopy (Olympus America Inc., Center Valley PA). Projection image Z-stacks of approximately 30 microns were collected and used for analysis. To calculate circularity, ImageJ software was used to trace cell perimeter and calculate subsequent areas of at least 20 cells per time point. The following equation was used to determine circularity, so that the value is normalized to one:

$$circularity = 4\pi \frac{area}{perimeter^2} \quad (1)$$

To quantify the phosphorylation of smad2/3, a rabbit polyclonal antibody (#5678; Cell Signaling, Danvers, MA; 1:125) and secondary Texas Red-tagged goat anti-rabbit Ab were utilized to quantify smad2/3 phosphorylation. The intensity of the fluorescence within the nucleus of the cell (determined by DAPI staining) was normalized to the intensity within the

outline of the cell body (determined by phalloidin staining) for three cells from three images for each condition using the open source software, ImageJ.

3.1.7 Fabrication and characterization of PDMS construct holder

The experimental apparatus consisted of a thick polydimethylsiloxane (PDMS) block in which two wells were created to hold 3D hydrogel constructs. A schematic of one of the wells is shown in Figure 3.1A. The dimensions of the PDMS substrate and construct wells are given in Figure 3.1B.

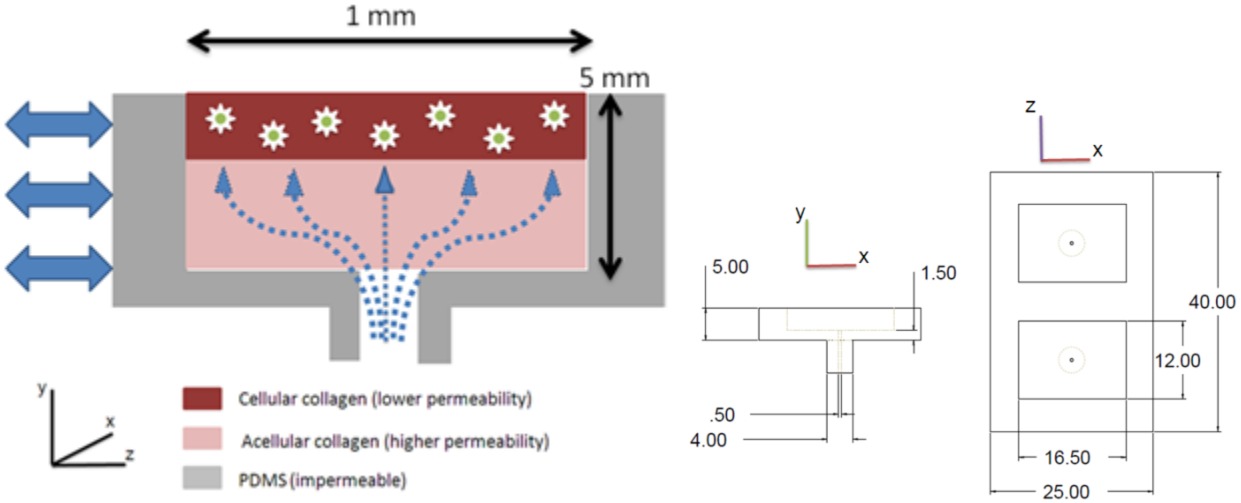

Figure 3.1 - **PDMS flow/strain wells:** A) A layer of porous, acellular collagen allows for distribution of flow in the zx plane, prior to passing through the cell-seeded gel in the positive y direction. Cyclic tensile strain is applied in the z direction. (B) Schematic of wells (dimensions in mm)

Because of the elastomeric properties of PDMS, this substrate allows for the application of cyclic mechanical strain to the cell-seeded gels inside each of the wells. The wells were also fitted with inlet ports to allow fluid to pass through the constructs. The gap between the well inlet port and the cell-seeded construct was filled with an acellular collagen gel. The purpose of this layer was to allow lateral (z-x) distribution of the entering fluid before it entered the cell-seeded construct.

The fabrication and characterization of the construct holder and collagen gel constructs are described in more detail in the paragraphs below.

The construct holder was made and prepared for use with collagen constructs by a multi-step process shown schematically in Figure 3.2.

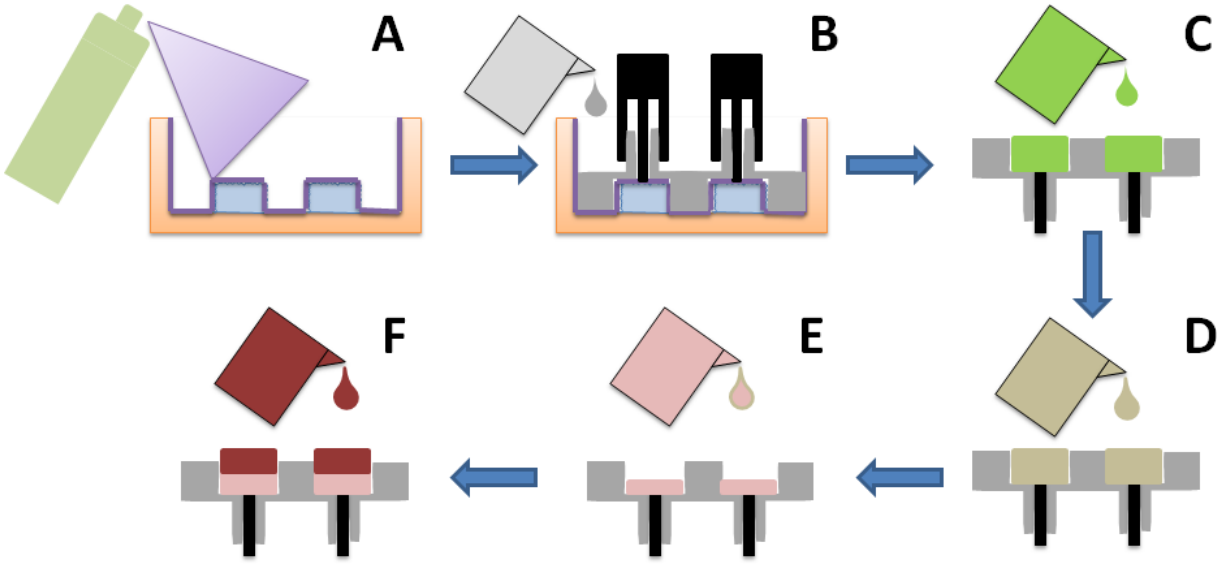

Figure 3.2 - **Fabrication and preparation of PDMS wells:** A) Delrin mold is fused with two porous polyethylene blocks, and a non-stick coating is applied. B) PDMS mixture is poured into the primary mold, and enters the inlet molds due to surface tension. C) After baking at 150 C for 10 minutes, the PDMS is removed from the mold. Using dowels to seal the inlets, 10 M sulfuric acid is used to etch the PDMS for 90 minutes. D) After autoclaving to sterilize the etched PDMS, a 20 µg/mL collagen I solution is used to coat the surface. E) The PDMS is incubated at 4 C for 4-5 days, and then a 300 µL, 2 mg/mL collagen hydrogel is added. F) Once the gel has solidified, a 700 µL cell-seeded collagen hydrogel is added and allowed to solidify.

PDMS base and curing reagent (Sylgard 184 Silicone Elastomer Kit, Dow Corning, Midland MI) were combined in a 10:1 (wt/wt) ratio and were mixed thoroughly. The substrate mold was created using a primary Delrin template containing porous polyethylene blocks (Small Parts, Seattle, WA) to produce textured wells. The mold was sprayed with NoStick (Stoner, Quarryville PA) to facilitate removal of the formed substrate (Fig. 3.2A). Inlet molds were inserted to create the inlet port to each well and the PDMS mixture was poured into the mold (Fig. 3.2B). The

assembled and filled mold was baked at 150 °C for 10 minutes and the cured PDMS substrates were removed from the mold. The inlet ports were then sealed with dowels and each well was filled with 10 N sulfuric acid for 90 minutes in order to etch the silicone surface and promote protein attachment (Fig. 3.2C). The wells were then thoroughly rinsed in deionized water and sterilized by an autoclave. Each well was filled with a solution of 20 μg/mL collagen Type I dissolved in PBS and incubated at 4°C for four to five days to facilitate collagen deposition (Fig. 3.2D). In preparation for experiments, the dilute collagen solution was removed from the wells and the acellular and cell-seeded collagen gels were fabricated in the wells.

In order to examine the effects of acid etching on the PDMS well surface, samples were analyzed by scanning electron microscopy. A control sample was taken directly after the curing process. Samples were also taken after the acid etching and after the collagen coating steps. All samples were sputter coated with platinum-gold, and images were collected at two magnifications on a scanning electron microscope (FEI Company, Hillsboro OR). For the acellular collagen sublayer, 300 μL of acellular gel was poured into the PDMS wells and allowed to gel at 37 °C in a humidified 5% CO_2 incubator. After an hour of incubation, 700 μL of cellular gel was added on top of the set acellular gels, and again allowed to gel at 37 °C in a humidified 5% CO_2. Constructs in wells were kept in the incubator for 24 hours before permeability testing or flow visualization.

3.1.8 Finite element modeling of PDMS well mechanics

COMSOL Multiphysics version 4.0 (COMSOL Inc., Burlington, MA) was used to construct a finite element model of the PDMS substrate under 5% normal strain in the z direction. The software was used to render the geometry of the 3D substrate and create a quadrilateral mesh. The mesh size was determined by increasing node resolution until the

computed strain distribution was unaffected by changing the resolution. The hydrogels were not included in the model because their elastic modulus is three orders of magnitude less than the PDMS [Schneider, 2009], and hence do not affect the mechanics of the PDMS. Because the gel was affixed to the PDMS, the strain calculated on the surfaces of the PDMS wells was assumed to be equal to the strain experienced by the gel. The PDMS was modeled assuming infinitesimal strains and isotropy, so the compliance tensor, C, in the stress-strain governing equation can be fully described by the elastic modulus and Poisson's ratio.

$$\sigma_{ij} = C_{ijkl} u_{(k,l)} \quad \text{for i,j = 1,2,3} \qquad (2)$$

where σ is the stress tensor, and u is the displacement tensor of the solid. The values of these parameters, E = 1.8 MPa and υ = 0.45, were taken from a previous study [Schneider, 2009].

3.1.9 Application of strain and flow

The set-up used to apply interstitial flow and mechanical strain to 3D constructs is shown in Figure 3.3. As shown in the schematic in the inset, fluid flow was applied through the inlet ports of the PDMS wells while strain was applied by stretching the entire PDMS substrate. The whole system was maintained at 37 °C using an outer water bath. The PDMS substrate was held by nylon grips, one of which was affixed to the floorplate of the bath chamber, while the other was affixed to an axial mechanical actuator system and control software (Test Resources, Shakopee MN). Interstitial flow was supplied by a syringe pump (KD Scientific, Holliston MA) through tubes connected to the well inlet ports, which were fitted with pressure sensors (Freescale Semiconductor, Austin TX).

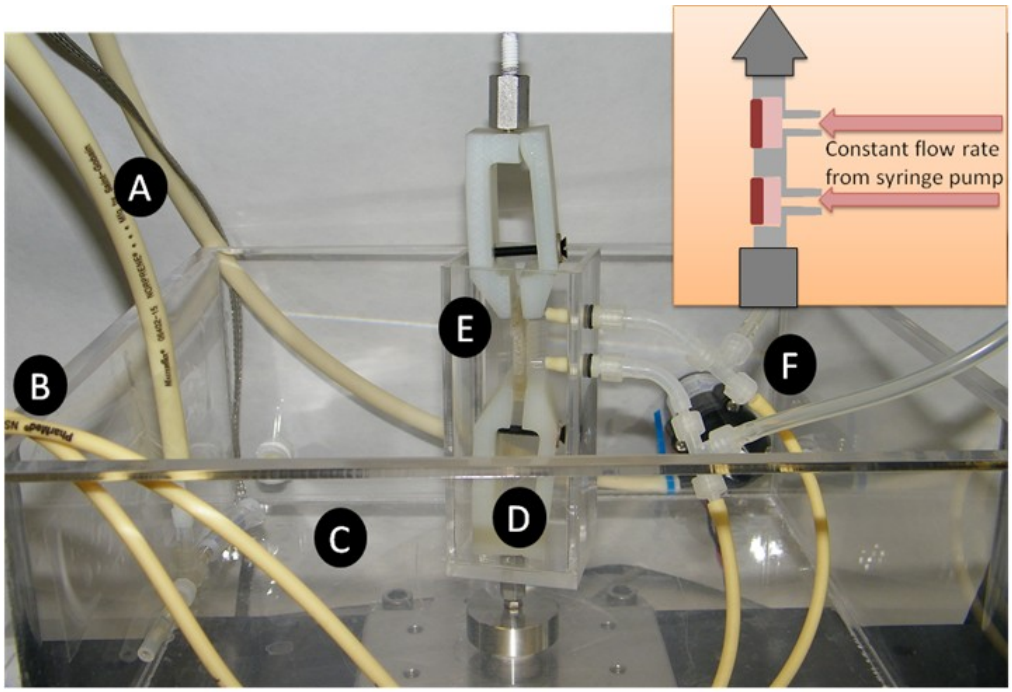

Figure 3.3- **Assembled flow/strain apparatus:** A) Feed and return lines for 37 C water heated by a water bath (not pictured). B) Tubes connected to the double-barreled syringe pump that delivers flow. C) Outer chamber filled with 37 C water. D) Inner chamber filled with media containing HEPES buffer to maintain pH over long periods of time. E) PDMS wells held by nylon clamps. F) Pressure tap locations.

This apparatus has the capability to apply strain and flow, either separately or in combination. For the experiments described here, the strain protocol was to apply 5 % cyclic strain at 1 Hz, while interstitial flow was applied at 10 μL/min. The strain was kept below 5% to maintain the infinitesimal strain assumption used in the finite element modeling. Strains greater than 15% caused failure in the PDMS substrate. Moreover, 10% strain applied at 1 Hz for two days caused detachment of the gel from the substrate. A magnitude of 5% was chosen to prevent detachment, and because prior studies demonstrated that 5% strain significantly affects the cell response of cardiac fibroblasts [Butt, 1997]. The flow rate was chosen to match previous interstitial flow studies [Chee Ping, 2003; Chee Ping, 2005].

All gels were cultured at 37C with 100% humidity and 5% CO2 for 24 hours prior to further testing. Gels digested after the 24 hour incubation served as initial controls, while the remaining gels were transferred to the testing apparatus or to an oxygen-controlled incubator set at 2.5% O2 for an additional 48 hours. Gels transferred to the bath but not exposed to any loading served as controls (denoted 48 h control). The remaining unloaded gels were transferred from the bath into the incubator for another 48 hours (denoted the 96 h control). The loading conditions included flow, strain, and a combination of strain and flow with and without inhibitors of angiotensin II type I receptor and TGF-β.

3.1.10 Permeability Testing

The testing setup provided a straightforward method of measuring permeability, since the syringe pump delivered a constant and known flow rate (Q), the pressure sensors could measure the pressure upstream of the constructs, and the thickness of the gels could be measured visually. Assuming the downstream pressure was atmospheric and negligible pressure drop between the measuring point and the constructs (~10 cm), the sensors gave the total pressure drop across the constructs (dP/dx). Because the dimensions of the constructs were confined by the PDMS wells, the area (A) was also known. Hence, permeability could be calculated using Darcy's equation for porous flow:

$$\kappa = \frac{Q}{A} dx / dP \tag{3}$$

Acellular and cellular gels were tested separately, and both were incubated for 24 hours prior to testing to allow for complete gelation and attachment to the PDMS substrate. The pressure measurements were made once a steady state was reached, which occurred after about two hours of fluid flow.

3.1.11 Flow Visualization

To assure the fluid flow distributed in the z-x plane in the acellular region before passing through the cell-seeded gel, photographic image-based flow visualization was used. Erioglaucine (792.85 g/mole, also known as brilliant blue FCF food coloring) was added to PBS in a 1:100 ratio (v/v), and supplied through the well inlet ports at 10 μL/min. The gels were then imaged at intervals up to ~80 minutes under both static conditions and while being exposed to a 5 % cyclic strain at 1 Hz.

3.1.12 Assessment of cell viability

Cell viability was assessed using the Live/Dead® assay kit (Invitrogen, Carlsbad CA). The gels were removed from the PDMS substrates, and washed 3X with PBS. The gels were then incubated at 37 °C for one hour in a PBS solution containing both ethidium homodimer and calcein AM in concentrations recommended by the manufacturer (4 μM and 2 μM respectively). After incubation, the gels were again washed 3X in PBS and visualized with an Olympus 500 confocal microscope at 10X magnification. Cell viability at the initial time point, as well as at 48 hours and 72 hours under static, no-flow conditions served as controls. Viability also was assessed after exposure to 10 μL/min fluid flow, 5 % strain at 1 Hz, and combined flow and strain at these levels.

3.1.13 Proliferation Assays

DNA quantity was assessed using a PicoGreen assay. Cell-seeded collagen gels were washed thoroughly with PBS, frozen at -80 C, then lyophilized overnight before being incubated in a proteinase K solution at 55 C for 12-16 hours. DNA quantity was normalized to the initial time points.

3.1.14 Immunoblotting

Gels were homogenized in Garner buffer containing protease and phosphatase inhibitors (50mM Trizma base, 150 mM NaCl, 1 mM phenylmethanesulfonylfluoride, 1% Triton X-100, 1 mM sodium orthovanadate, 10 mM sodium phosphate, 50 mM sodium fluoride, and ddH_2O) for cellular protein separation. Tubes were then boiled in a water bath for 3 minutes, sonicated for 10 minutes, and centrifuged 3 times at 2000 g for 15 seconds, before quantifying protein with a BCA assay (Thermo-Fisher, Rockford, IL), and storing samples at -20C until immunoblotting. For gels treated with control and AT1R lentivirus particles, trypsinized cells washed in PBS were lysed in ice-cold sample buffer (24.77% glycerol, 1.63% SDS, 0.1 M Trizma stacking buffer, 3.31% Bromophenol Blue stock solution, 24.88 mM DTT, 1.78 mM leupeptin), and then stored at -20C.

In preparation for protein separation, samples were boiled for 3 min, sonicated for 10 min, and then mixed with sample buffer in a 1:1 ratio. Proteins were separated with 12% or 4-12% gradient SDS-polyacrylimide 12 well gels (Bio-Rad), and then transferred onto a PVDF membrane overnight. The PVDF membrane was then blocked in either 5% dry nonfat milk or BSA, washed in Tris buffered saline (TBS), and incubated overnight at 4^{o}C with either a rabbit polyclonal antibody against phosphorylated smad2/3 (3101; Cell Signaling; 1:500), a rabbit polyclonal antibody against smad2/3 (3102; Cell Signaling; 1:500), or a rabbit polyclonal antibody against AT1R (sc-1173; Santa Cruz Biotech, Santa Cruz, CA; 1:200). The next day, blots were rinsed with TBS and incubated for 45 minutes at room temperature with HRP-linked anti-rabbit secondary antibodies (7404; Cell Signaling; 1:2000). Gels were silver stained and a representative protein band was used to normalize for protein loading on the blot for the AT1R knockdown verification. Immunodetection was visualized with chemiluminescence using Pierce ECL Western Blotting substrate (Thermo-Fisher).

3.1.15 Lentiviral knockdown

Cardiac fibroblasts isolated from neonatal rats were grown to 50% confluency in 100 mm diameter Petri dishes over 4-6 hours after plating, and yielded approximately 9000 cells/cm^2. Lentiviral-mediated gene transfer was initiated by adding viral particles to M199 media containing 5 μg/mL Polybrene (Santa Cruz Biotech) for 16-20 hours. Gene transfer with lentivirus utilized an MOI of 1 and included controls containing scrambled shRNA (sc-108080, Santa Cruz Biotech), and an experimental group with shRNA to disrupt AT1R production (sc-155992-V, Santa Cruz Biotech). After viral transduction, cells were split and cultured in T75 culture flasks. 24 hrs later, media was replaced with puromycin-containing media (2.5 μg/mL) to deplete non-infected cardiac fibroblasts from the cultures. After 48 hours in puromycin-containing media, the cells were seeded into gels within a week after primary dissociation. Knockdown verification on immunoblots was completed using aliquots of lysed cells prior to initiating cell incorporation into hydrogels.

MSC were incubated for 2 hours after plating to ensure cell attachment. Lentiviral-mediated gene transfer was initiated by adding viral particles to DMEM media containing 5 μg/mL Polybrene (Santa Cruz Biotech) for 14 hours. Viral particles were added at a density of 4.44 k/cm2, resulting in an MOI of 1.33. After the viral incubation, the medium was replaced with fresh DMEM and the cells allowed to proliferate.

3.1.16 Mesenchymal stem cell delivery

A micromanipulator was used to assure that the cell injections were uniform in amount and location in the collagen hydrogels. MSC injection was performed 12 hours after polymerization of the collagen hydrogel. A 1 mL syringe equipped with a 1” 25 gauge needle was mounted on the manipulator at an angle of 30 degrees from the gel surface. The 3 axis

manipulator allowed for axial displacement control, so the needle tip penetrated 5 mm into the gel. A schematic of the dimensions of the injection is shown in Figure 3.4. Once the needle reached its desired position, 40 µL of 6.25 M/mL MSC solution was injected into each gel, resulting in the addition of 250,000 MSC. Gels were then incubated for one hour at 37 C before being returned to culture medium to allow for attachment of the stem cells.

3.1.17 ELISA

Quantikine ELISA assays purchased from R&D systems were used to quantify the presence of VEGF and IGF-1 in the supernatants from the coculture hydrogels. When being removed from the PDMS wells, the gels would leave 100-150 µL of supernatant. This solution was collected in polypropylene microtubes and stored at -20C for 1-2 months until ELISAs were performed.

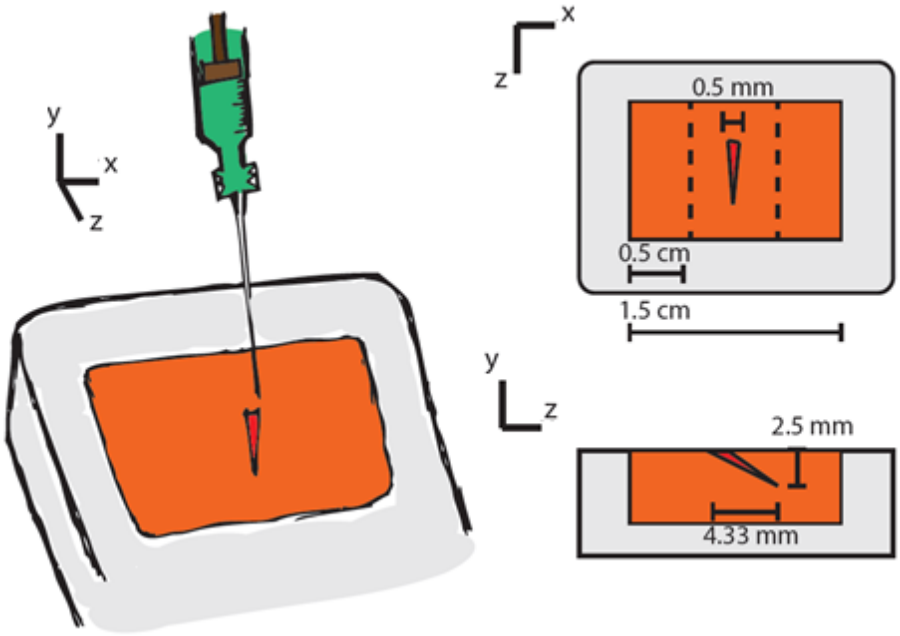

Figure 3.4 - **Schematic of injection placement within the cell-seeded gel:** A micromanipulator was used to ensure the injections were not variable with each test. The cells were injected at a 30 degree angle from the gel surface. The dotted lines show where the gels were sectioned to analyze the fibroblast response.

3.1.18 Statistical Analysis

Data are reported from sample sizes of 3-6 separate experiments. The error bars presented on the graphs represent one standard deviation. For comparisons of two groups, an unpaired Student's t-test was used to determine statistical significance with $p < 0.05$ considered significantly different. An analysis of variance (ANOVA) followed by Tukey's multiple comparison test ($p<0.05$) was used to compare multiple groups using the open source statistical package R (http://www.r-project.org/).

3.2 Mathematical Model

Note: The development of this model was carried out in collaboration with Dr. Ben Vaughan of the University of Cincinnatti.

As illustrated by Figure 3.1, the cell-seeded gel is molded above an acellular gel, and bounded on its side walls by the PDMS well. As described previously, the gels were exposed to three different modes of mechanical stimulation: 5% cyclic strain, 10 μL/min of cross flow, or a combination of strain and cross flow. Figure 3.5 illustrates these different modes, and a representation of the appropriate boundary conditions.

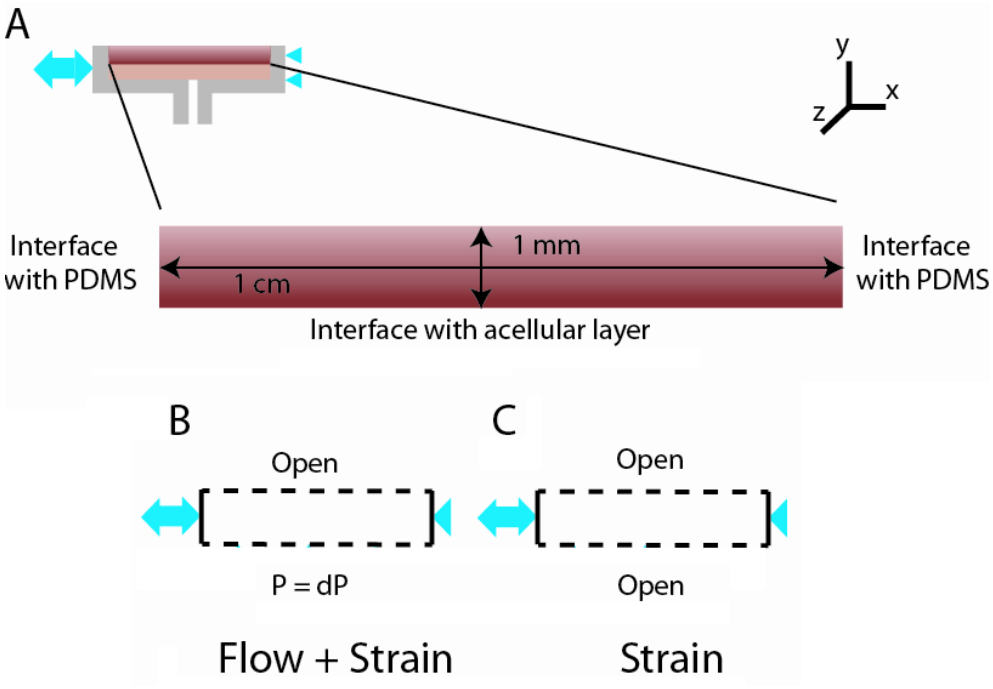

Figure 3.5 – **Physical basis for poroelastic model boundary conditions:** A) The gel was bounded on both sides by PDMS, open to atmosphere at the top boundary, and attached to the acellular region on the bottom boundary. B-C) Graphical representation of the boundary conditions for application of cross flow: a dotted line represents an open boundary, and a triangle denotes a boundary that is fixed in both the x and y directions.

We model the gel as a Biot poroelastic medium (cite). The $u-$ formulation is

$$\mu_s \nabla^2 \underline{u} + (\lambda + \mu_s) \nabla (\nabla \cdot \underline{u}) = \nabla p \tag{4}$$

$$\frac{\partial}{\partial t} (\nabla \cdot \underline{u}) = k \nabla^2 p \tag{5}$$

where $\underline{u} = (u_1, u_2)^T$ is the solid displacement, p is the pressure, μ and λ are the solid Lamé constants, $k = \kappa / \mu_f$ is the hydraulic conductivity, κ is the permeability, and μ_f is the fluid viscosity. Here, we have assumed that the solid matrix is intrinsically incompressible and the

fluid in infinitely incompressible. Using Darcy's law, we relate the relative fluid velocity, $\underline{v} = (v_1, v_2)^T$, to the pressure by the relation

$$\underline{v} = -\frac{k}{\varphi}\nabla p \quad . \tag{6}$$

The gel resides in a two-dimensional rectangular domain of length L and height H, where the wall at $x =$ is an oscillating wall with frequency ω and amplitude A. Since we will examine two different domain configurations, we shall discuss boundary conditions specific to each configuration separately.

Domain Configuration:

In this configuration, we have two solid walls (one fixed and one oscillating) and two open boundaries to allow a crossflow due to a pressure gradient to occur (Figure 3.6).

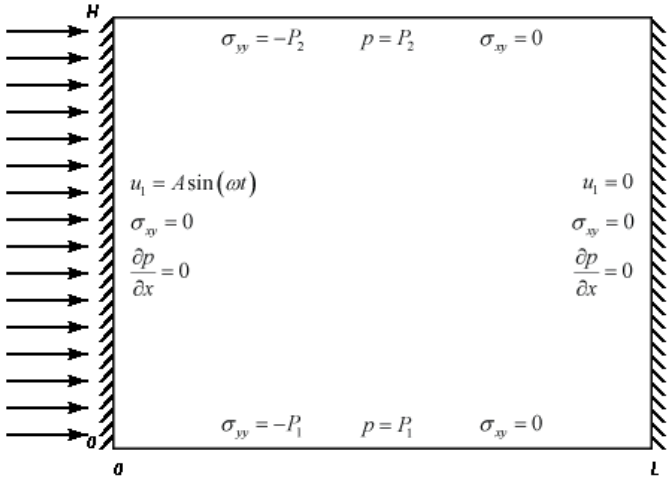

Figure 3.6 - **Domain configuration and boundary conditions with crossflow:** Shear stress at all the walls is set to zero, and the pressure gradient is fixed at boundaries with no flow. The value of P_1 determines the presence of cross flow.

Here, the components of the stress tensor are

$$\sigma_{xx} = \left(\lambda + 2\mu_s\right)\frac{\partial u_1}{\partial x} + \lambda\frac{\partial u_2}{\partial y} - p \tag{7}$$

$$\sigma_{yy} = \left(\lambda + 2\mu_s\right)\frac{\partial u_2}{\partial y} + \lambda\frac{\partial u_1}{\partial x} - p \tag{8}$$

$$\sigma_{xy} = \mu_s\left(\frac{\partial u_1}{\partial y} + \frac{\partial u_2}{\partial x}\right) \tag{9}$$

If we assume the following scales

$$\begin{aligned} \underline{u} &= H\underline{u}^*, \quad \underline{x} = H\underline{x}^*, \quad t = \frac{t^*}{\omega}, \\ p &= \frac{H^2\varphi\omega}{k}p^*, \quad \underline{v} = \omega H\underline{v}^*, \end{aligned} \tag{10}$$

we obtain the non-dimensional $u-p$ equations

$$\mu_s^*\nabla^2\underline{u}^* + \left(\lambda^* + \mu_s^*\right)\nabla\left(\nabla\cdot\underline{u}^*\right) = \nabla p^* \tag{11}$$

$$\frac{\partial}{\partial t^*}\left(\nabla\cdot\underline{u}^*\right) = k^*\nabla^2 p^* \tag{12}$$

along with the non-dimensional Darcy's law

$$\underline{v}^* = -\nabla p \tag{13}$$

for $0 \le x \le L^*$ and $0 \le y \le 1$. Here, $L^* = L/H$, $\mu_s^* = \mu_s k/\omega H^2\varphi$, $\lambda^* = \lambda k/\omega H^2\varphi$, and $k^* = \varphi$.

The dimensionless boundary conditions are now

$$\begin{array}{lll} u_1^*\left(0, y^*, t^*\right) = A^*\sin\left(t^*\right) & \sigma_{xy}^*\left(0, y^*, t^*\right) = 0 & \left.\dfrac{\partial p^*}{\partial x^*}\right|_{x^*=0} = 0 \\ u_1^*\left(L^*, y^*, t^*\right) = 0 & \sigma_{xy}^*\left(L^*, y^*, t^*\right) = 0 & \left.\dfrac{\partial p^*}{\partial x^*}\right|_{x^*=L^*} = 0 \\ \sigma_{yy}^*\left(x^*, 0, t^*\right) = -P_1^* & \sigma_{xy}^*\left(x^*, 0, t^*\right) = 0 & p^*\left(x^*, 0, t^*\right) = P_1^* \\ \sigma_{yy}^*\left(x^*, 1, t^*\right) = -P_2^* & \sigma_{xy}^*\left(x^*, 1, t^*\right) = 0 & p^*\left(x^*, 1, t^*\right) = P_2^* \end{array} \tag{14}$$

where $P_1^* = \omega\varphi H^2 P_1/k$ and $P_2^* = \omega\varphi H^2 P_2/k$.

We begin by removing the inhomogeneous pressure boundary conditions separating the crossflow solution from the oscillatory solutions:

$$p^*\left(x^*,y^*,t^*\right)=P_1^*-\left(P_1^*-P_2^*\right)y^*+p_o\left(x^*,y^*,t^*\right) \tag{15}$$

The crossflow solution does induce any deformation in the medium. We can now obtain the solution

$$u_1\left(x^*,t^*\right)=A^*\left(1-\frac{x^*}{L^*}\right)\sin\left(t^*\right) \tag{16}$$

$$u_2\left(y^*,t^*\right)=\frac{A^*}{L^*}\Im\left\{\left(y^*-\frac{2\mu_s^*}{\nu^*\left(\lambda^*+2\mu_s^*\right)}\left[\frac{\cos\left(\nu^*\right)-1}{\sin\left(\nu^*\right)}\cos\left(\nu^*y^*\right)+2\sin\left(\nu^*y^*\right)\right]\right)e^{it^*}\right\} \tag{17}$$

$$p_o\left(y^*,t^*\right)=\frac{2\mu_s^*A^*}{L^*}\Im\left\{\left(1-\cos\left(\nu^*y^*\right)+\frac{\cos\left(\nu^*\right)-1}{\sin\left(\nu^*\right)}\sin\left(\nu^*y^*\right)\right)e^{it^*}\right\} \tag{18}$$

The relative fluid velocity, including the crossflow, is

$$v_2=\left(P_2^*-P_1^*\right)+\frac{2\mu_s^*A^*}{L^*}\Im\left\{\nu^*\left(\frac{\cos\left(\nu^*\right)-1}{\sin\left(\nu^*\right)}\cos\left(\nu^*y\right)-\sin\left(\nu^*y\right)\right)e^{it^*}\right\} \tag{19}$$

with no flow in the horizontal direction. The values input into the model are taken both from solid mechanics characterization of the hydrogels, including elastic modulus (15111 Pa) and Poisson's ratio (0.33). The permeability was calculated to be 1.43E-11m^2 for cell-seeded gels, and the porosity was estimated to be 0.996, using an equation from [Ramanujan, 2002]. The pressure at the top boundary, P_1, was assumed to be zero. The upstream pressure, P_2, was calculated from the known volume flow rate of the syringe pump, the thickness and width of the gel, and the permeability of the gel: 77.6 Pa. The y component of fluid shear stress was calculated from the Tarbell equation [Wang, 1995]:

$$\tau_2 = \frac{\mu \phi^f}{k} v_2 \tag{20}$$

Chapter IV

Results

4.1 Effect of serum and substrate compliance on the myofibroblast transition

3D Collagen Gel Compaction: Our studies demonstrated media, serum concentration, and cell density each significantly influence the ability of fibroblasts to transition to the myofibroblast phenotype. In our first experiments, these variables altered the ability of the hydrogels to produce the compaction of released 3D gel cultures over the course of 120 hrs in culture. Gel compaction, defined as ratio of measured gel volume to original volume at t = 0, is a measure of passive fibroblast contractility and compaction increases over time in culture when gels are seeded with fibroblasts. Significantly higher compaction is observed with low serum (5% FBS) compared to high serum (10% FBS) levels in culture media (Fig. 4.1A). The highest compaction rate occurred within 6 h after initiating the culture for both serum formulations and the lower serum media produced the highest level of compaction (to 9.5 % of original volume). These results were repeated for cells given DMEM media, though compaction was not as high as the M199 results (Fig. 4.1B). Moreover, the effect of serum was not as evident in the DMEM data set, as indicated by the lack of significance at the 120 hour time point. Increased fibroblast cell density also stimulated gel compaction when comparing gels seeded with 0.5-, 2.5- or 5- x 10^5 cells (Fig. 4.1C).

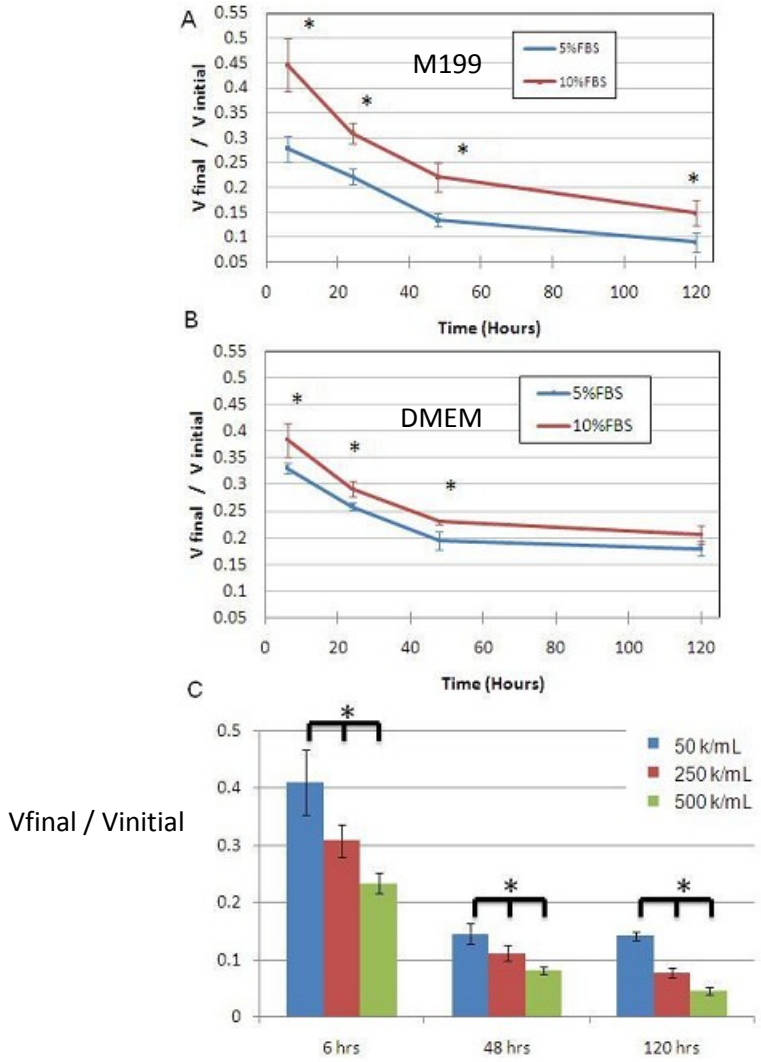

Figure 4.1 - **Influence of serum concentration and cell density on compaction:** A) Higher FBS concentrations in M199 attenuated the compaction for all time points. B) These results were repeated for DMEM media. C) Gels cultured with M199 + 10% FBS and seeded with different cell densities compared at three time points. Statistical comparisons were carried out using ANOVA and Tukey's multiple comparison test with $p<0.05$ (*) indicating significant differences.

Effect of Gel Constraint: Released and constrained gels were compared to evaluate the influence of matrix stiffness on message and protein expression of collagen I and III, TFG-β, and α-SMA along with fibroblast morphology. Figures 4.2 and 4.3 compare gene expression and representative immunocytochemistry results from cardiac fibroblasts cultured in released versus

constrained 3D collagen matrices for up to 48 h in M199 supplemented with 5 and 10% FBS. No significant difference in collagen I, collagen III, or TGF-β, or α-SMA gene expression was observed between released and constrained gels at 5% serum concentration (Fig. 4.2A). Released and constrained gels were then studied with the higher 10% FBS concentration to determine whether nutrient availability affected the effect of matrix stiffness on this transition. Though other message levels were again unaffected, expression of α-SMA was significantly higher in constrained matrices at the 6 and 24 h time points compared to released gels (Fig. 4.3A).

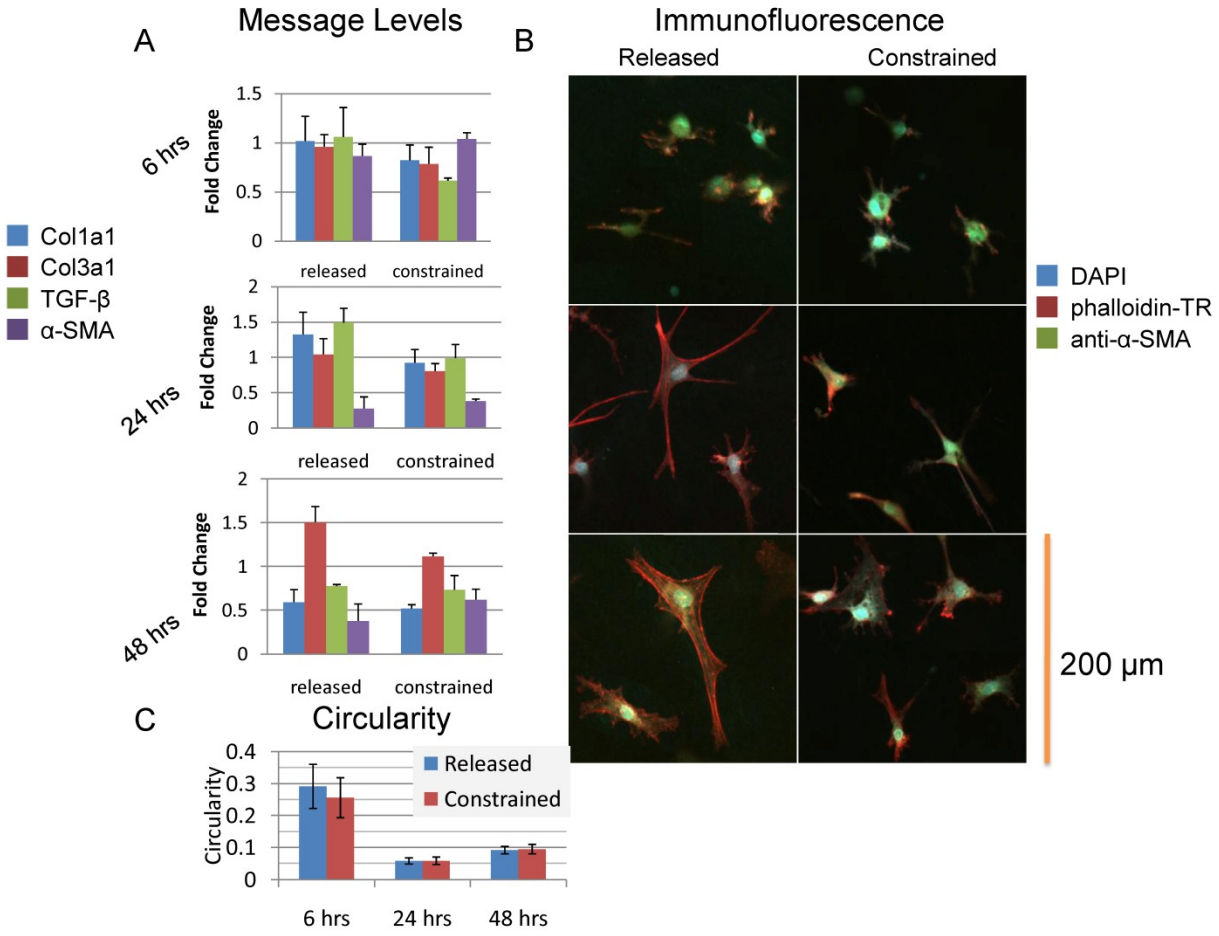

Figure 4.2 - **Message expression and cellular morphology in gels cultured in M199 with 5% FBS:** A) message expression of col1a1, col3a1, TGF-β, and α-SMA in released (left panels) or constrained (right panels) fibroblast-seeded gels. B) merged images of constrained (left panel)

and released (right panel) collagen gels stained for DAPI (blue), actin (red), and α-SMA (green). C) quantification of the immunofluorescence images shown in Panel B, using a circularity parameter.

The increase in α-SMA message levels observed in response to this increased matrix stiffness provided evidence that passive tension accelerates the transition of these cells to myofibroblasts. These finding suggests that lack of serum nutrients and increased matrix stiffness each modulate the expression of α-SMA in the myofibroblast transition, but their effects may not be additive. A similar association between constrained and released gel environments was noted when analyzing cell morphology. Morphological changes generally developed in concert with α-SMA expression, with α-SMA-positive cells displaying fewer and shorter processes and a more spherical morphology (Figs. 4.2B and 4.3B). In order to quantify this spherical morphology, ImageJ was used to calculate circularity of the cells. For cells exposed to 5% serum, there was no significant difference in circularity between released and constrained gels over the three time points (Fig. 4.2C). In contrast, cells cultured in 10% serum in released gels showed significantly less circularity for the first 24 h. The circularity results follow the message levels of α-SMA produced by cells in the constrained and released gels and indicate a more compact cellular morphology accompanies α-SMA expression and differentiation into the myofibroblast phenotype.

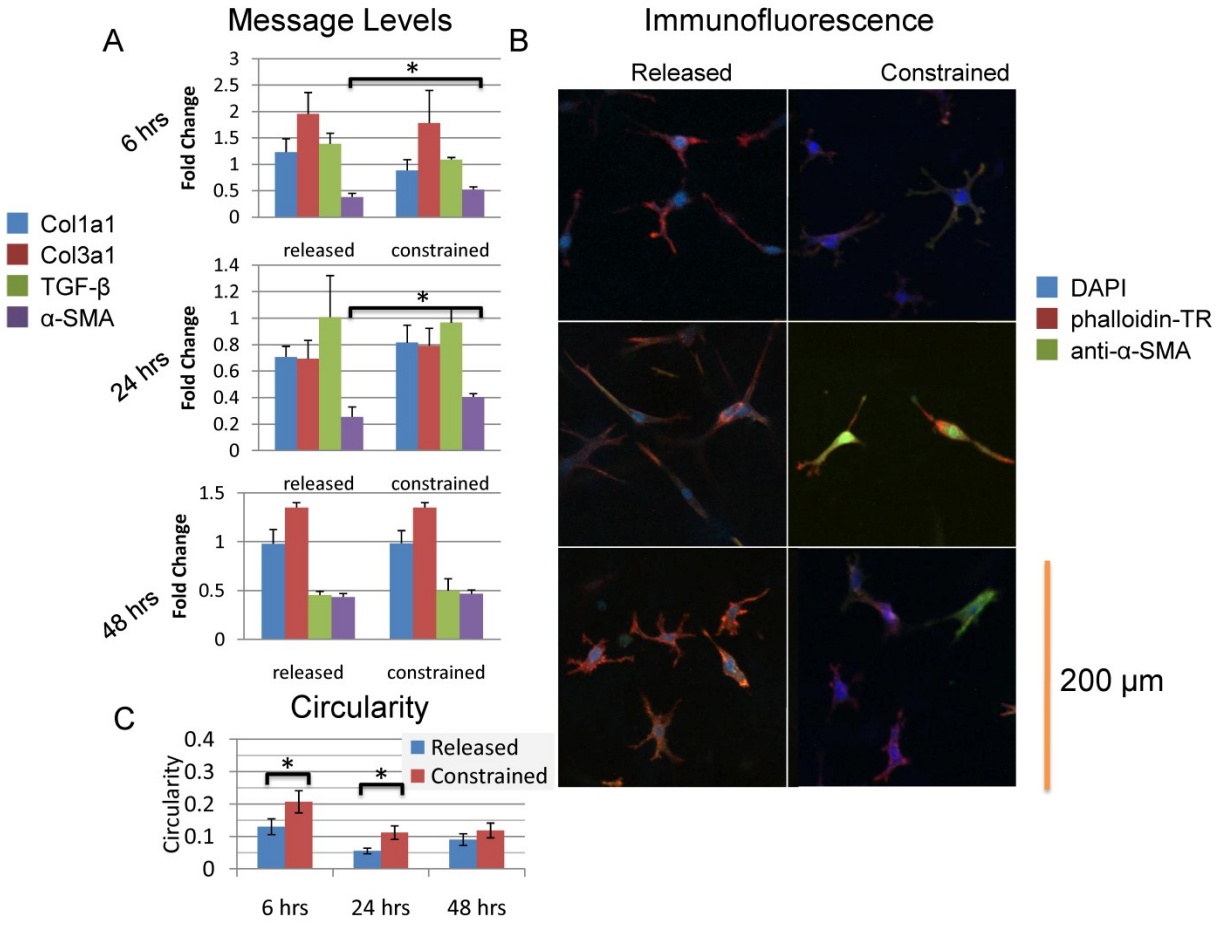

Figure 4.3 - **Message expression and cellular morphology in gels cultured in M199 with 10% FBS:** A) cells cultured in M199 media containing 10% FBS showed significantly less α-SMA expression for the first 24 hours when seeded into the released hydrogel compared to constrained gel. However, by 48 hours, the expression of the protein was statistically insignificant. B) merged images of constrained (left panel) and released (right panel) collagen gels stained for DAPI (blue), actin (red), and α-SMA (green). C) quantification of the immunofluorescence images shown in Panel B, using a circularity parameter. The significant differences in circularity at 6 and 24 h mirror the differences in message levels of α-SMA (Panel A). Results were compared using a Student's t-test $p<0.05$ (*) considered significantly different.

Effect of Serum Content: The above studies demonstrated an important role for serum in determining the functional phenotype. Thus, the influence of serum on expression of collagens I and III, TGF-β, and α-SMA was further analyzed in the released gels as a function of time. Cells cultured in 5% serum produced significant increases in gene expression of α-SMA within 6 h and

TGF-β at 24 h relative to cultures supplemented with 10% serum (Figs. 4.4C and 4.4D). There does not appear to be any significant effect of serum on these message levels beyond 24 h. Because matrix stiffness had little influence on collagen and TGF-β gene expression, this result suggests nutrient and mechanical stimuli may stimulate α-SMA expression and/or other upstream events in myofibroblast development via different pathways.

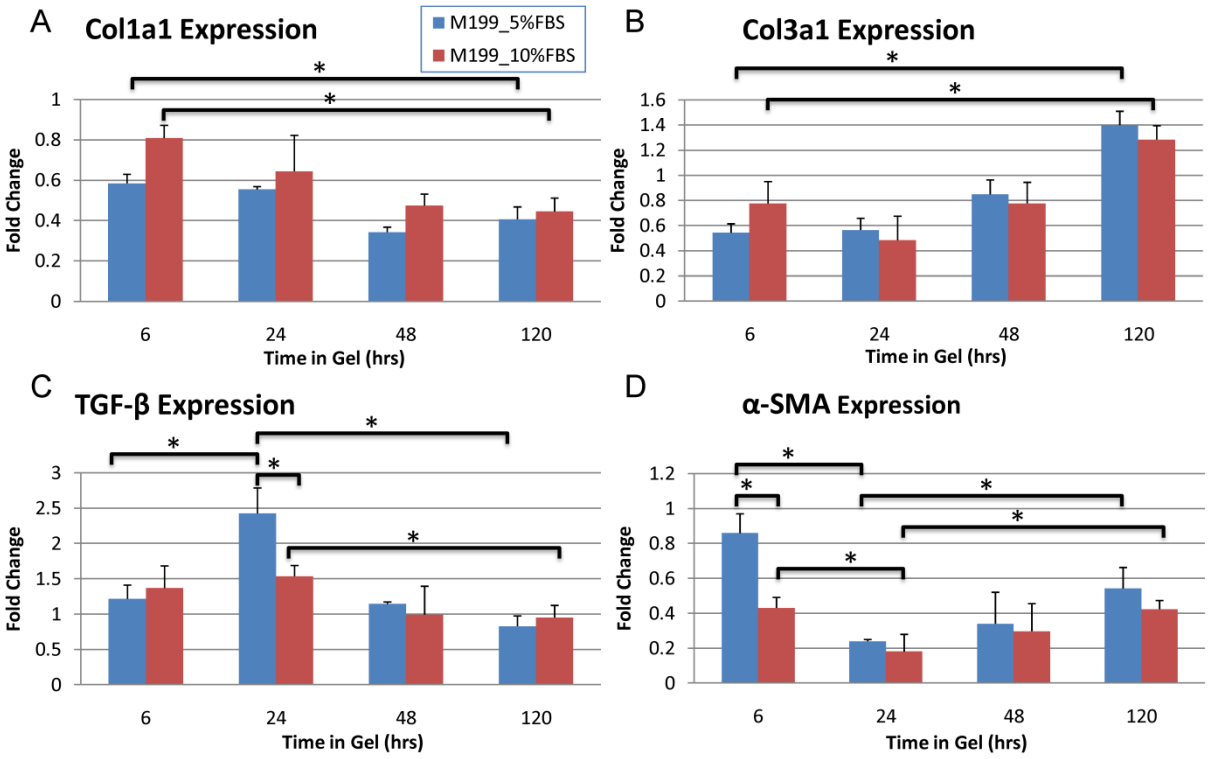

Figure 4.4 – **Message levels of cells seeded in released gels cultured in M199 with 5% and 10% FBS:** A) Col1a1 expression significantly decreased, while B) col3a1 significantly increased over time, although there were no differences in response to FBS levels. C) For cells cultured in 5% FBS, significantly higher TGF-β expression occurred at the 24 hour point compared to other time points. A spike in TFG-β expression also was observed at 24 hrs with 10% FBS, although this increase was significantly less than that observed with 5% FBS. D) A biphasic change in α-SMA expression was observed with both serum levels, with an initial decrease, followed by a return toward the 6 hr level after 24 hours. Significant differences were determined using ANOVA and $p<0.05$ (*) considered significantly different using a post-hoc Tukey multiple comparison tests.

The results also provide evidence that expression of these key indicators mirrors the functional response, although the temporal response appears to be specific for each indicator (Fig. 4.4). For example, collagen I expression decreased significantly while collagen III expression steadily increased between 6 and 120 h for both serum concentrations (Figs. 4.4A and 4.4B). The level of TGF-β expression (Fig. 4.4C) also peaked at 24 h before declining to lower levels at the 48 and 120 h timepoints for both serum levels. Interestingly, a bimodal α-SMA expression profile develops for both serum concentrations, with the highest expression at 6 h, followed by a significant dip at 24 h and a secondary rise at 48 h and 120 h (Fig. 4.4D). These transcript-specific patterns of expression provide additional evidence this differentiation process not only involves different pathways, but also utilizes complex spatial and temporal signaling events.

The general trends of this data were repeated in cell-seeded gels cultured in DMEM, as shown in Figure 4.5. The cells exhibited the same general trends in decreased collagen I expression, and increased collagen III expression (Fig. 4.5A,4.5B). For cells exposed to 5% FBS, the 24 hour time point had significantly higher expression of TGF-β than the 6 hour and 120 hour time points (Fig. 4.5C). The α-SMA expression significantly decreased at the 24 hour time point, prior to significantly increasing by the 120 hour time point (Fig. 4.5D). Again, this expression pattern follows the stiffness of the released gels. Unlike the M199 data set, there were significant differences between the two serum levels in the α-SMA message levels for all but the 24 hour time point, when levels were attenuated almost to zero.

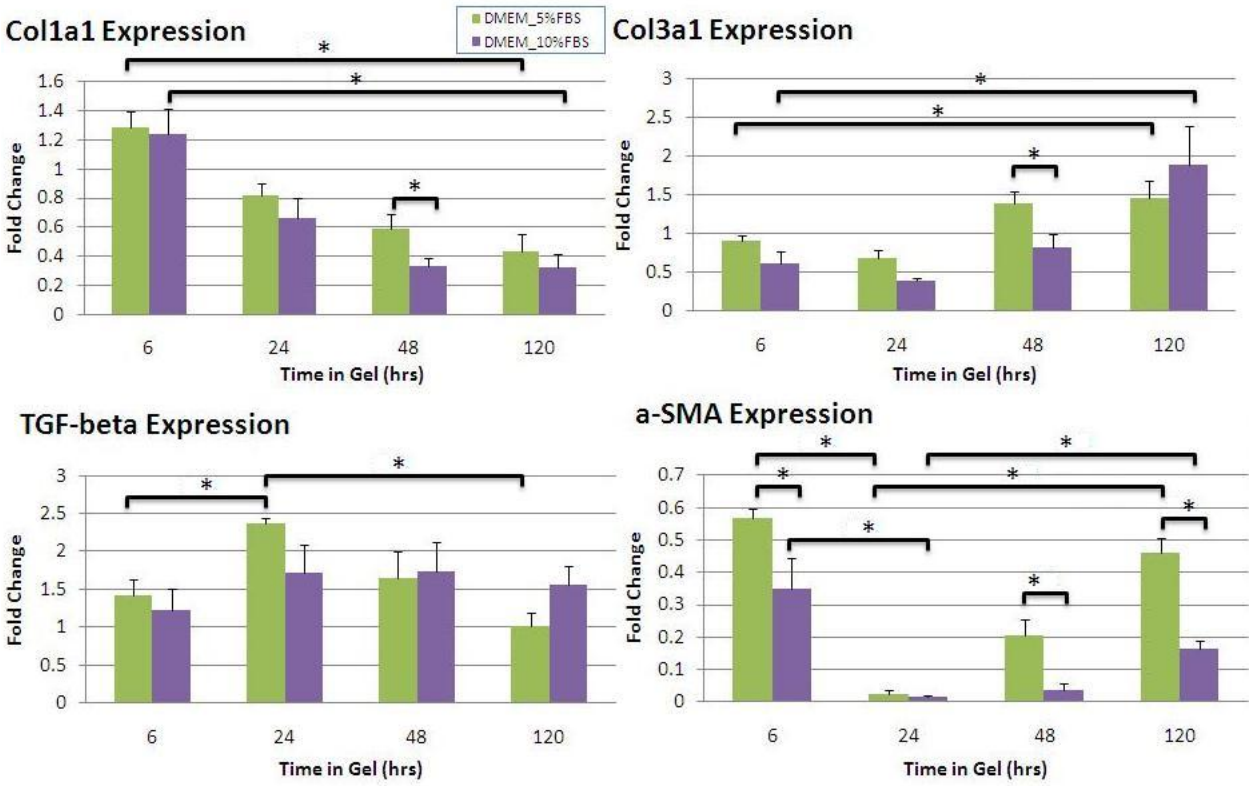

Figure 4.5 – **Message levels of cells seeded in released gels cultured in DMEM with 5% and 10% FBS:** A-D) Message levels of col1a1, col3a1, TGF-β, and α-SMA followed the same patterns of cells cultured in M199 at the same serum levels.

Mechanical Properties of 3D Collagen Matrices: Serum influences on neonatal fibroblast cultures also influenced the bulk mechanical properties of released gels**.** Elastic modulus (Fig. 4.6A) and phase loss angle (Fig. 4.6B) were measured at the initial (6 h) and final (120 h) time points in hydrogels seeded with neonatal fibroblasts and cultured in either 5 or 10% FBS. The elastic modulus increased significantly over time with both serum concentrations (Fig. 4.6), indicating that matrix stiffness increased as the neonatal cells differentiated over time.

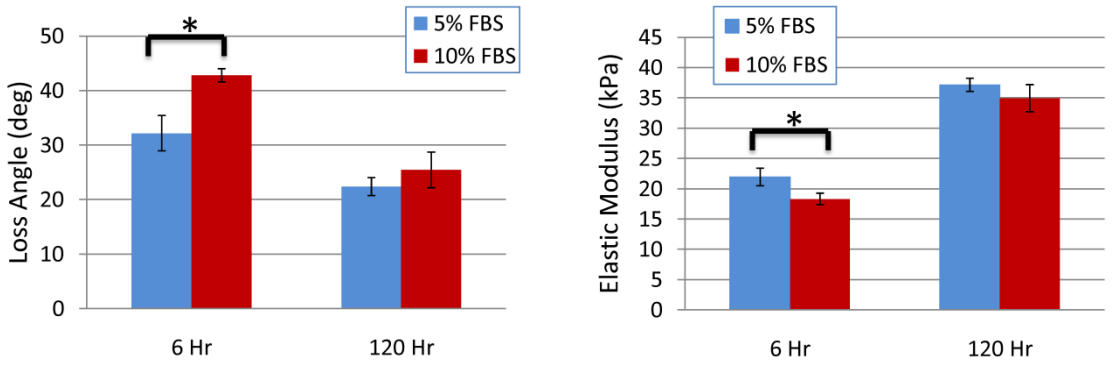

Figure 4.6 - **Elastic moduli and loss angle of released gels cultured in M199 + 10% FBS:** A) Released gels were strained at high strain rates (30%/s) to determine the elastic moduli or B) cyclically compressed at 1 Hz to determine the loss angle of the samples. Results were compared using a Student's t-test $p<0.05$ (*) considered significantly different.

The lower FBS concentration produced significantly less compliant gels at 6 h (Fig. 4.6A), but this serum-dependent difference in elastic modulus was abolished after 120 h in culture. Similarly, Figure 4.6B shows that the viscoelastic phase angle for gels cultured in low FBS was significantly lower than that for 10% FBS at the initial time point, but was not different at the later time point. The decrease in phase angle indicates the gel became stiffer over time, while also losing its viscous fluid properties and behaving more like an elastic solid. The differences in gel mechanical properties were largest at the early time point, which corresponds to the point where the differences in the degree of compaction also were greatest.

4.2 Application of simultaneous cyclic strain and interstitial fluid flow

Adhesion of collagen constructs to PDMS wells

In order to apply simultaneous cyclic strain and defined fluid flow through the construct, it is necessary that the collagen matrix remains firmly attached to the walls of the PDMS well to prevent fluid leakage around the edges of the gel. Cardiac fibroblasts seeded in a 3D collagen matrix will remodel and compact the collagen fibers [Poobalarahi, 2006] and in the presence of

uniaxial cyclic strain the cells will align the matrix in the direction of the strain [Voge, 2008]. These processes produce forces that can pull the collagen matrix away from the walls of the well, and therefore these cellular forces need to be overcome to maintain attachment of the gel to the PDMS. Acid etching of the PDMS and subsequent coating with dilute collagen was used to promote construct adherence to the wells. In the absence of any treatment, hydrogels detached from the PDMS after 4-6 hours. After etching the PDMS with 10 N sulfuric acid, gels stayed attached for 2-3 days. When additionally coated with 20 μg/mL collagen type I after etching, the 3D gels remained attached to the PDMS for 14-18 days. To determine whether the etching produces surface changes to the PDMS that might be responsible for increased collagen adherence, scanning electron microscopy was used to analyze the microstructure of the surface. Figure 4.7 shows electron micrographs of untreated (Figs. 4.7A-B), acid etched (Figs. 4.7C-D), as well as etched and coated PDMS surfaces (Figs. 4.7E-F). Untreated surfaces were essentially smooth with <1 μm surface features. After 90 minutes of etching with sulfuric acid, the PDMS displayed clearly larger surface features, on the order of 10 μm. After collagen coating, the surface once again exhibited a smooth appearance, presumably due to filling of the features with collagen matrix. While acid etching produced a much rougher surface topography, it is not known whether it also changed the surface chemistry or charge. The rougher surface provided improved gel adhesion, but subsequent collagen coating clearly had the greatest positive effect on collagen gel adherence.

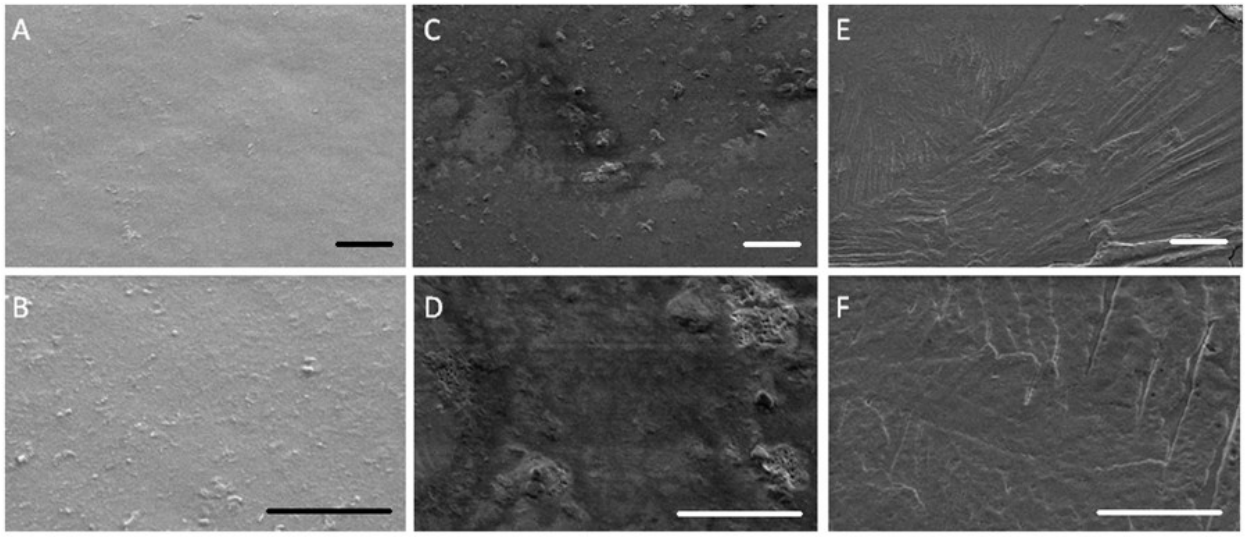

Figure 4.7 - **SEM images of the PDMS surface:** A-B) Control (after curing). C-D) After 90 minutes of etching with 10 N sulfuric acid. D-E) After 24 hours of incubation with collagen-PBS solution following acid etch. Scale bars for ACE = 20 μm, BDF = 10 μm.

Finite Element Model

A global uniaxial strain of 5% was applied to the apparatus based on the initial PDMS substrate dimensions. We performed finite element modeling to better characterize the strain field and to determine the actual magnitude of strain on the constructs within each of the wells. The results of this modeling are shown in Figure 4.8, and show that there are regional variations in the applied strain. Figure 4.8B shows the z component of the strain tensor ( ) along a y-z slice through the midline of the deformed PDMS substrate. The model shows that the PDMS material separating the wells is essentially unstrained in the z-direction, while the floor surfaces of the wells exhibited axial strains of slightly greater than 5%. The strain distribution was relatively continuous on the surface of the well with the exception of the location of the fluid inlet.

Due to the relatively high Poisson's ratio of the PDMS (υ=0.45), an axial strain of 5% in the z direction also produced deformation in the x and y directions. The bottom surfaces of the deformed wells are shown in Figure 6C-E, which show the x-, y-, and z-components of the strain tensor, i.e. ( ) respectively. The averages and standard deviations of the strain values for these surfaces were calculated for each well. The average strain in the x-direction on the surface was -0.029 +/- 0.008 for both the wells, -0.018 +/- 0.009 for both wells in the y direction, and 0.065 +/- 0.014 for both wells in the z direction.

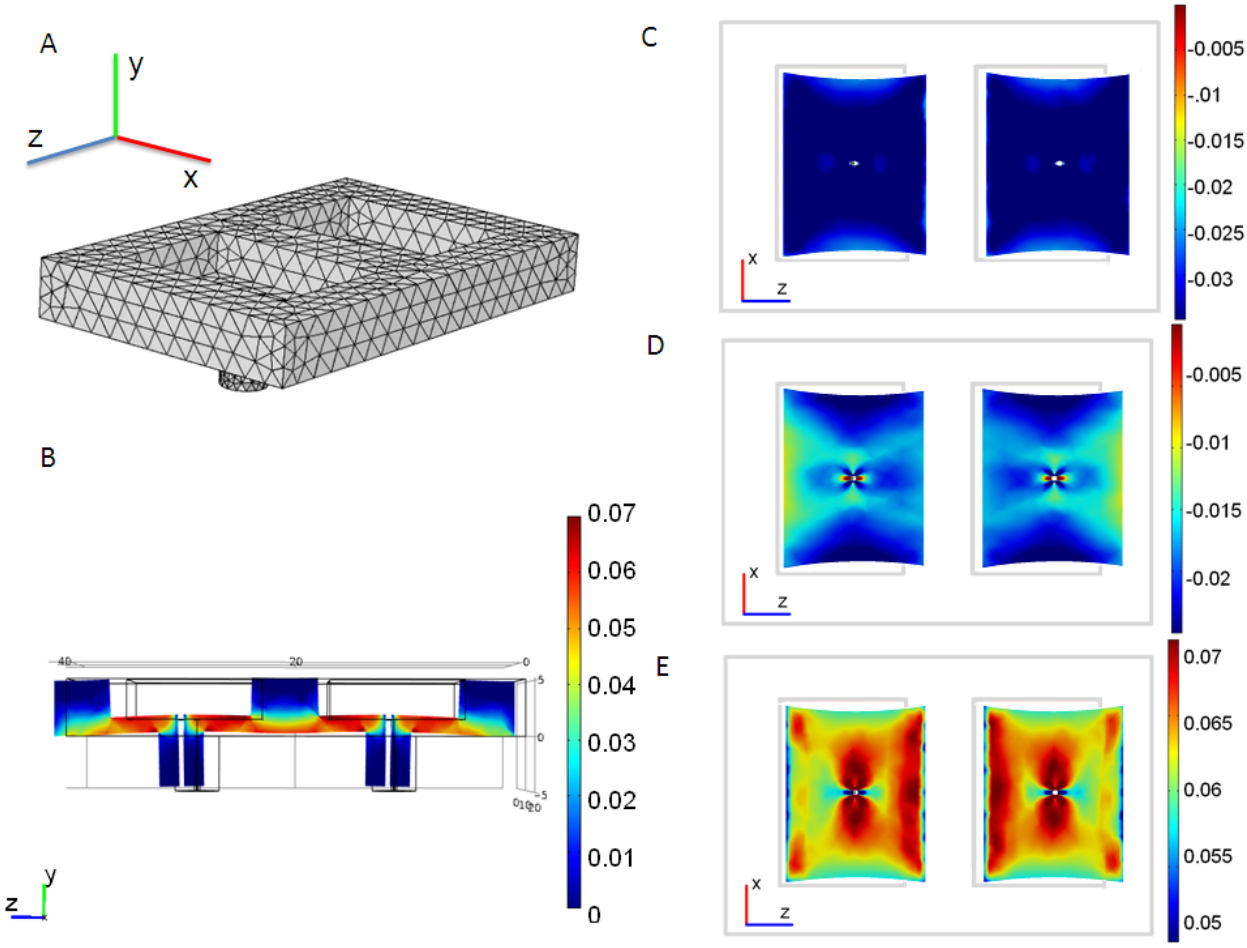

Figure 4.8 - **Finite element model of well deformation:** A) 3D finite element mesh that discretizes the geometry of the PDMS substrate, B) A y-z slice through the centerline of the substrate that shows a contour plot of the zz component of the strain tensor. C-E) A z-x slice through the substrate at the bottom surface of the wells showing contour plots of the xx (C), yy

(D), and zz (E) components of the strain tensor. For all contour plots, the solid lines indicate the original, undeformed geometry of the substrate, and the x-y-z grid is shown in part B.

Therefore while there was slight compression (2-3%) in the x and y directions, the tensile strain applied to the wells was approximately 6.5%. These results validate that the primary component of strain was in the z direction, though the magnitude was slightly greater than the global applied strain. The local variation in the strain field that was observed suggests that this model is not appropriate for microscale analysis of the effects of strain. However, it is appropriate for tissue-level analysis since the wells experienced similar strains that were close to the applied strain magnitude.

Permeability of unseeded and cell-seeded collagen gel

The layer of acellular collagen was used to achieve a uniform flow distribution prior to entering the fibroblast-seeded construct. For this approach to work, the acellular collagen layer must have significantly higher permeability than the cell-seeded construct, creating a higher pressure drop in the y-direction and resulting in preferential flow in the z-x plane. Once the pressure has built sufficiently in the acellular region, the fluid will then flow in the y direction across the cell-seeded gel, in spite of its lower permeability. Because of the simple geometry and known boundary conditions of the PDMS apparatus, it could be used to determine the permeability of collagen constructs.

Figure 4.9 shows the results of the permeability testing for both acellular and cell-seeded constructs under both static and strained conditions. Acellular gels exhibited approximately 4-fold higher permeability than fibroblast-seeded gels. In previous published studies, the permeability values of acellular collagen gels at concentrations ranging from 10-30 mg/mL were determined [Ramanujan, 2002]. A curve fit of this data can be extrapolated to 2 mg/mL, resulting

in a permeability value of approximately 5.4×10^{-11} m^3s/kg, which falls within the error of the present measurement of acellular gels. Cell-seeded gels exhibited lower permeabilities, around 1.4×10^{-11} m^3s/kg. Both types of gels were constrained and attached to the PDMS wells, so that gel compaction was prevented in the z-x plane, but not in the y direction. Therefore, compaction of the gels in this direction during the 24 hour incubation period could be the cause of the reduced permeability, since the thickness of the gels stayed constant after the 24 hour point.

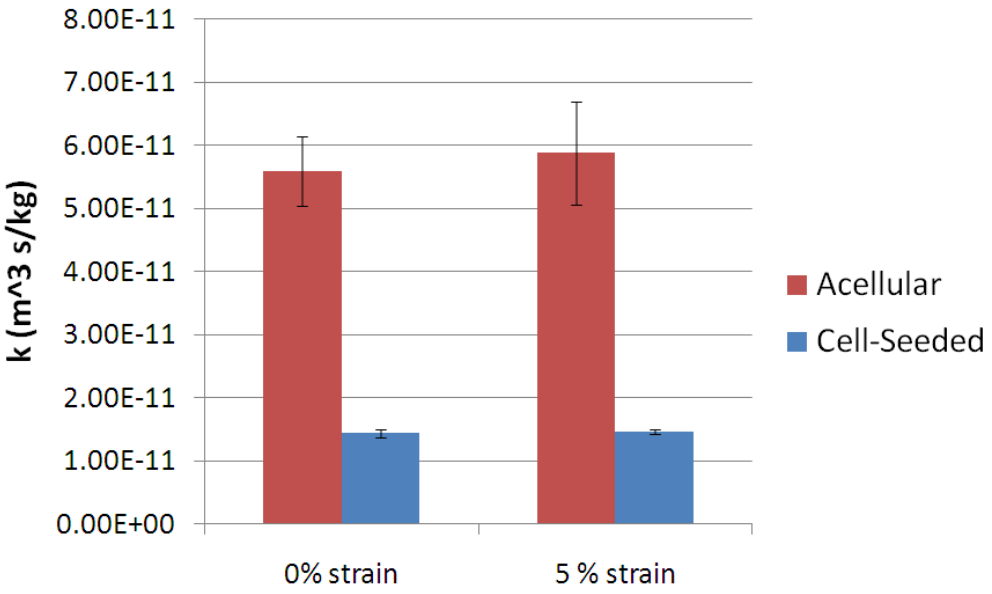

Figure 4.9 - **Gel permeability measurements:** Permeability was measured for both acellular and cell-seeded gels for both static and 5% tensile strained conditions. Error bars represent one standard deviation from the mean measurement.

There was no significant difference in the permeability of static gels and strained gels, whether they were acellular or fibroblast-seeded. This measurement is important because it confirms that 5% global stretch did not cause leakage of fluid around the constructs, which would have resulted in substantially increased fluid transport. These findings also have significance for computational modeling of the gel mechanics, since they indicate that permeability can be considered independent of strain for this type of construct. A previous study analyzed

permeability of collagen constructs exposed to compressive strain in the same direction as the fluid flow, and showed permeability was affected by strain [Serpooshan, 2011]. The present result shows that 5% strain in the plane perpendicular to the direction of flow does not affect permeability.

Flow distribution in acellular support gel

To directly test whether flow was uniformly distributed in the acellular region before passing through the cell-seeded gel, PBS containing blue dye was injected through the inlet of the construct wells under both static and cyclically strained conditions. Images were taken perpendicular to the z-x plane as the flow entered the PDMS wells and spread within the acellular region.

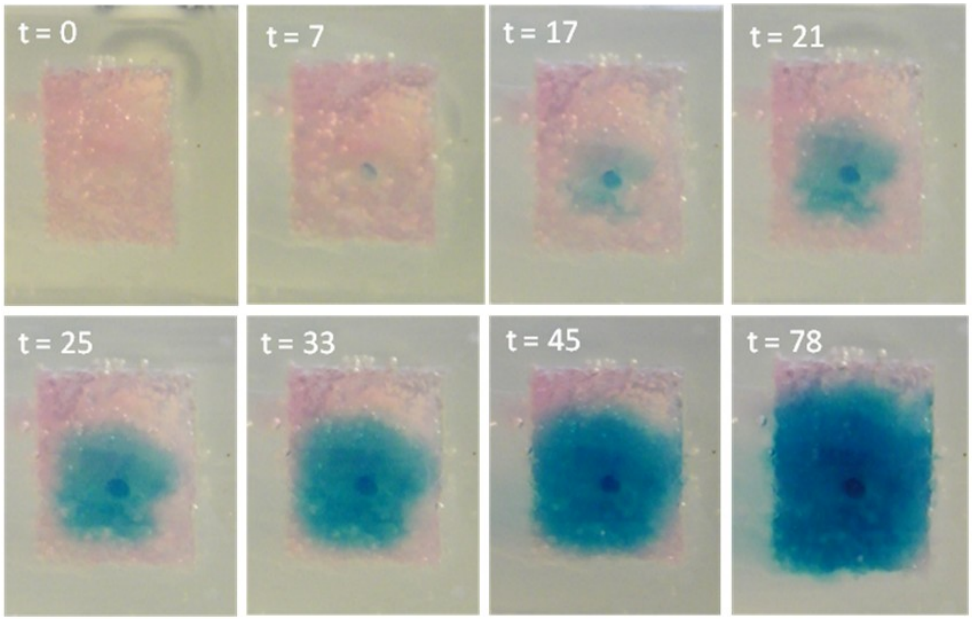

Figure 4.10 - **Flow visualization for a static gel:** These images depict the xy plane of the layered acellular and cellular gels as 10 μL/min of colored PBS is injected into the PDMS wells. The blue dot near the center of the gel indicates the location of the fluid inlet.

Figure 4.10 shows the time course of dye perfusion at a flow rate of 10 μL/min under static conditions. The dye perfuses evenly out of the inlet port and distributes within the acellular gel

over about 80 minutes. It was evident that flow did not pass through the cell-seeded gel in the y direction until fully distributing in the z-x plane. Figure 4.11 shows similar image data for cyclic straining to 5 % at 1 Hz. In this case, the flow distributes uniformly in the x direction, however in the z direction the fluid initially flows preferentially in the direction of the applied strain. In order to quantify this effect, the position of the leading edge of the flow in the positive z direction was compared to the position of the edge in the negative z direction, using the inlet as the coordinate axis origin. Figure 4.12 shows the results of this analysis for both the static and strained gels. For the static gel, the ratio stays constant at approximately one, indicating uniform flow. For the strained gel, the flow is initially skewed in the positive z direction, though as time progresses and the acellular region fills, the ratio recovers to approximately one. This result indicates that although strain does affect the fluid flow profile, the flow first distributes in the z-x plane before passing through the cell-seeded construct for both static and strained conditions.

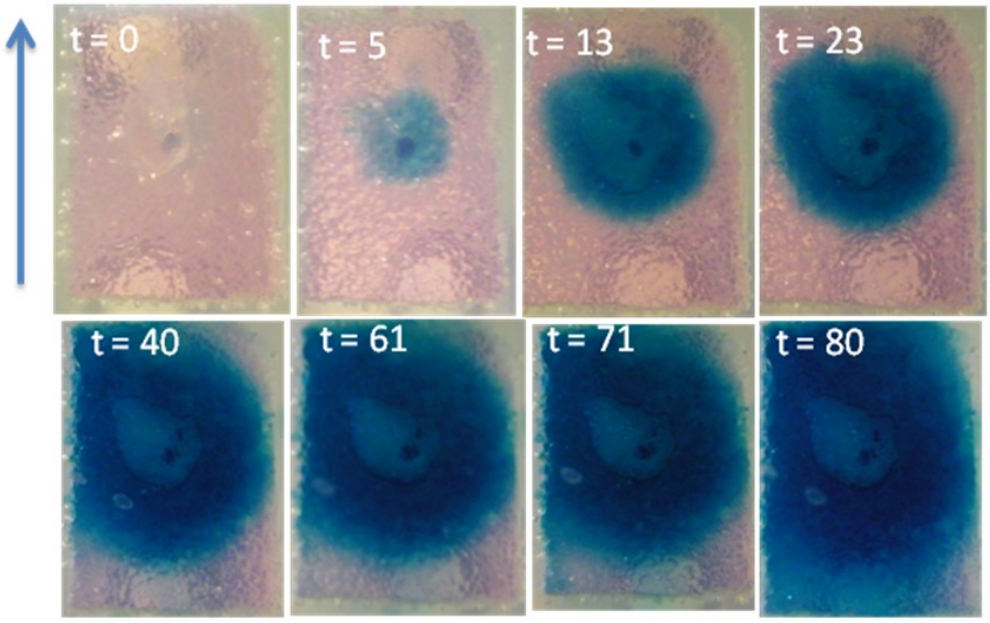

Figure 4.11 - **Flow distribution for a cyclically strained gel:** The blue arrow indicates the direction of strain, and again the location of the fluid inlet is visible.

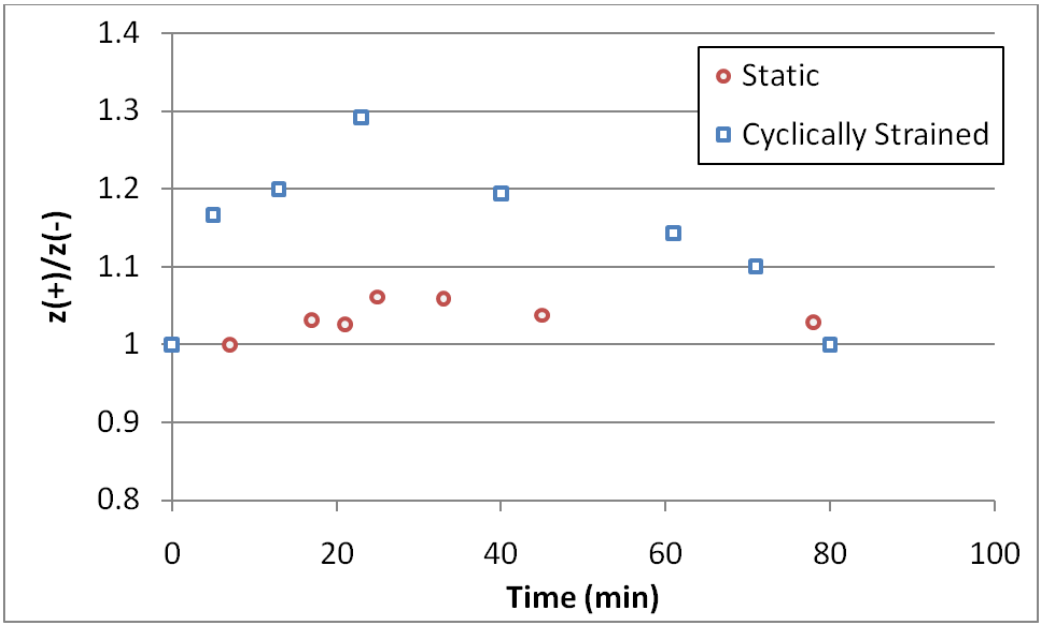

Figure 4.12 - **Quantification of flow visualization:** This plot indicates how the flow distribution in the cycling gel is skewed in the direction of strain (positive z direction) compared to the distribution in a static gel.

Cell viability in constructs under strain and flow

In order for the apparatus to be useful for studying cell responses to strain and flow stimuli, cell viability must be maintained in the 3D collagen construct. Figure 4.13 shows cell viability data for different time points, with and without strain and flow. At the 24 hour time point (Fig 4.13A), immediately before constructs are mounted in the strain/flow apparatus, cell viability was high (above ~85 %). When constructs were maintained in the PDMS wells in the absence of flow and strain, viability remained very high at both the 72 hour (Fig. 4.13B) and the 120 hour (Fig. 4.13C) time points. After stimulation by either flow (Fig. 4.13D), or strain (Fig. 4.13E), or a combination of flow and strain (Fig. 4.13F) for 48 hours (i.e. 72 hours after initial creation of the construct), the viability in all constructs also remained very high (generally over 80-90 %). These data suggest that cells can be maintained in 3D collagen constructs in PDMS wells and

that application of flow and/or strain does not compromise cell viability. This result is important for the use of this flow-strain system for the examination of cell function in 3D hydrogels over time.

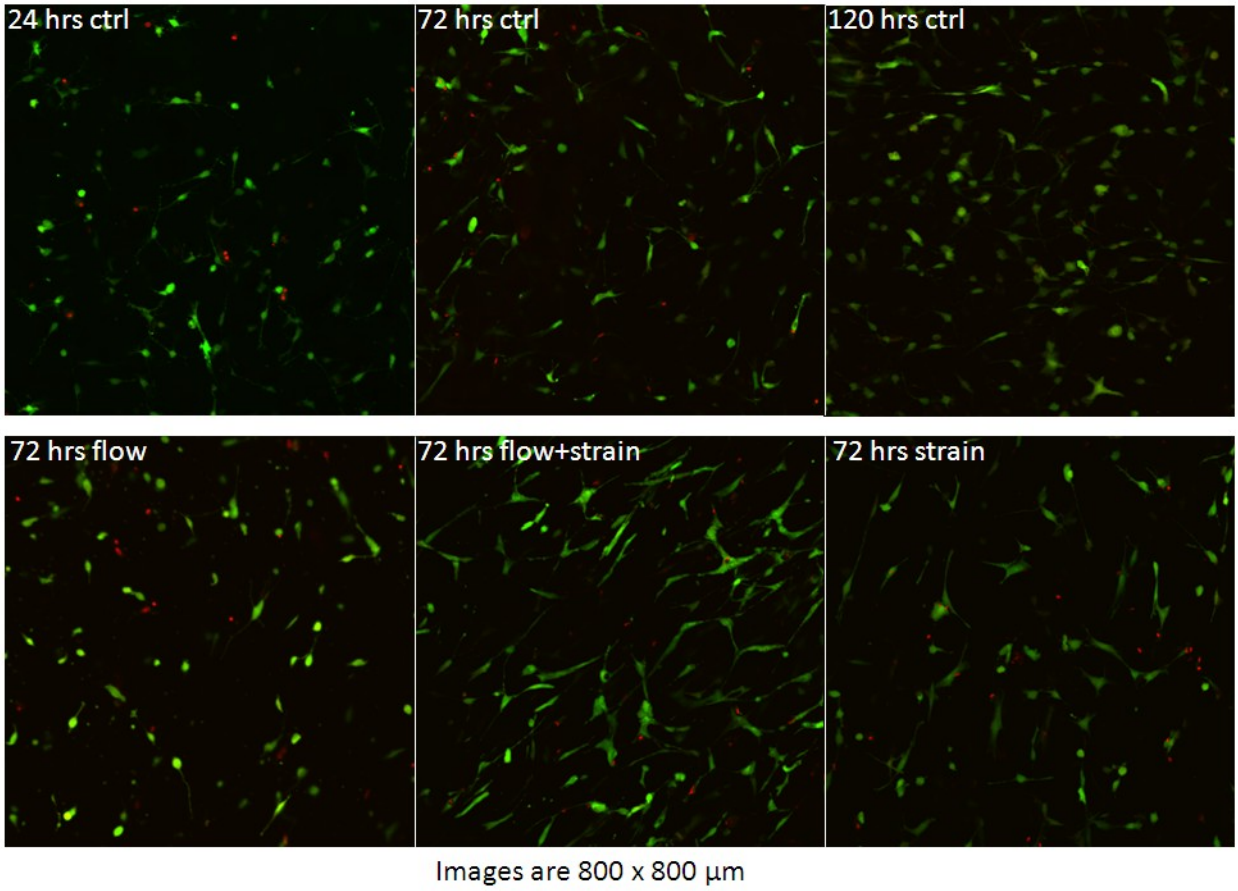

Figure 4.13 - **Cell viability for different testing configurations:** Live cells enzymatically convert calcein AM to fluorescent calcein, while ethidium homodimer is able to penetrate the nuclei of dead cells and bind to nucleic acid, increasing its fluorescence emission by 40x. The images show a similar ratio of live to dead cells for all testing configurations and time points. All times are expressed in terms of hours after creation of the gels. All gels were incubated under static conditions for 24 hours, and then exposed to either fluid flow, strain, a combination of both, or static conditions (control).

Because the viability experiments lasted for two days, the pressure drop across the stacked gels provided insight into whether the permeability of the gels changed with time. The permeability of the acellular gel, without cells to remodel the matrix, was assumed to stay

constant. A change in permeability of the cellular gel would indicate remodeling of the matrix by the cells. However, over the two day testing period of the viability experiments, the pressure drop stayed constant once steady state was reached.

4.3 Cardiac fibroblast response to cyclic strain and interstitial fluid flow

The Effect of Mechanical Stimuli on Expression of Myofibroblast Markers

The present study demonstrates that mechanical stimuli modulate the fibroblast to myofibroblast transition, though the mechanisms involved result in distinct transduction of fluid-induced and stretch-induced stresses. As showed in Figures 4.4-4.5, fibroblasts in collagen gels created in standard culture plates and cultured for 48 and 96 h transitioned to a myofibroblast phenotype, marked by significant elevations in the mRNA message levels for collagen type III and α-SMA, and a reduction in TGF-β1 expression. This baseline pattern was repeated in gels polymerized in the PDMS wells in the present study, as indicated in Figure 4.14. Note that the time points designated "48 h" and "96 h" are identical to the "72 h" and "120 h" time points in Figures 4.1-6.

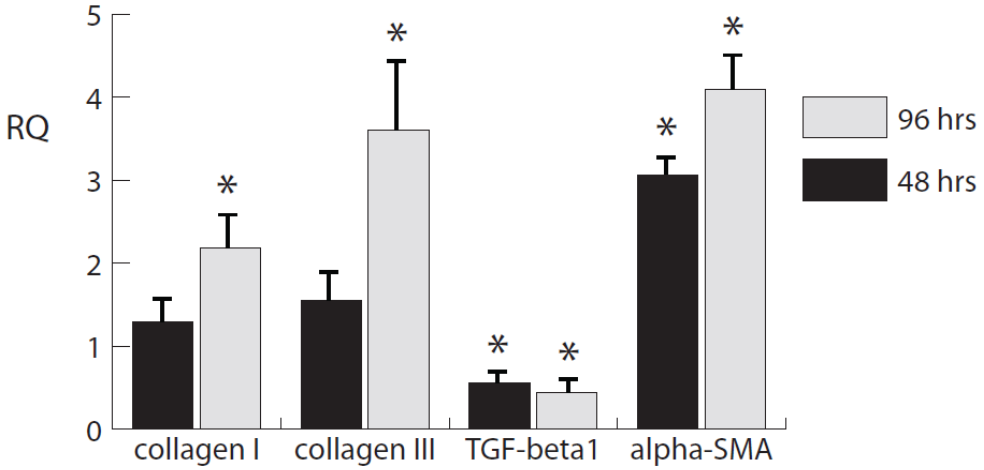

Figure 4.14 – **Baseline trends in message levels:** Message expression of the 48 h and 96 h control samples levels showing collagen type I (A), collagen type III (B), TGF-β (C), and α-SMA (D) after. Levels are normalized to initial (t=0) levels. A * designates significance from the initial time point, as determined by 2 sample t-tests.

Collagens type I and III serve as markers for matrix deposition in the myocardium, and α-SMA as a marker for the myofibroblast phenotype. Therefore, polymerizing cardiac fibroblast-seeded collagen gels in PDMS wells did not alter the baseline shift to a myofibroblast phenotype.

mRNA expression of myofibroblast markers (collagen I and III, α-SMA, and TGF-β1) was measured and immunolocalization of α-SMA were performed in response to a 48 h exposure to combinations of interstitial flow and cyclic strain, as well as to a 2.5% oxygen environment. As shown in Figure 4.15A, neither mechanical stimulation (by cyclic stretch or cross-flow) nor hypoxia significantly affected collagen type I message levels. However, cross flow significantly increased collagen type III levels over control levels, both in the presence and absence of cyclic strain, whereas cyclic strain alone did not significantly affect message levels (Fig. 4.15B). Similarly, cross flow both with and without cyclic strain prevented the drop in TGF-β1 expression observed in the control samples and in cyclic strain conditions (Fig. 4.15C).

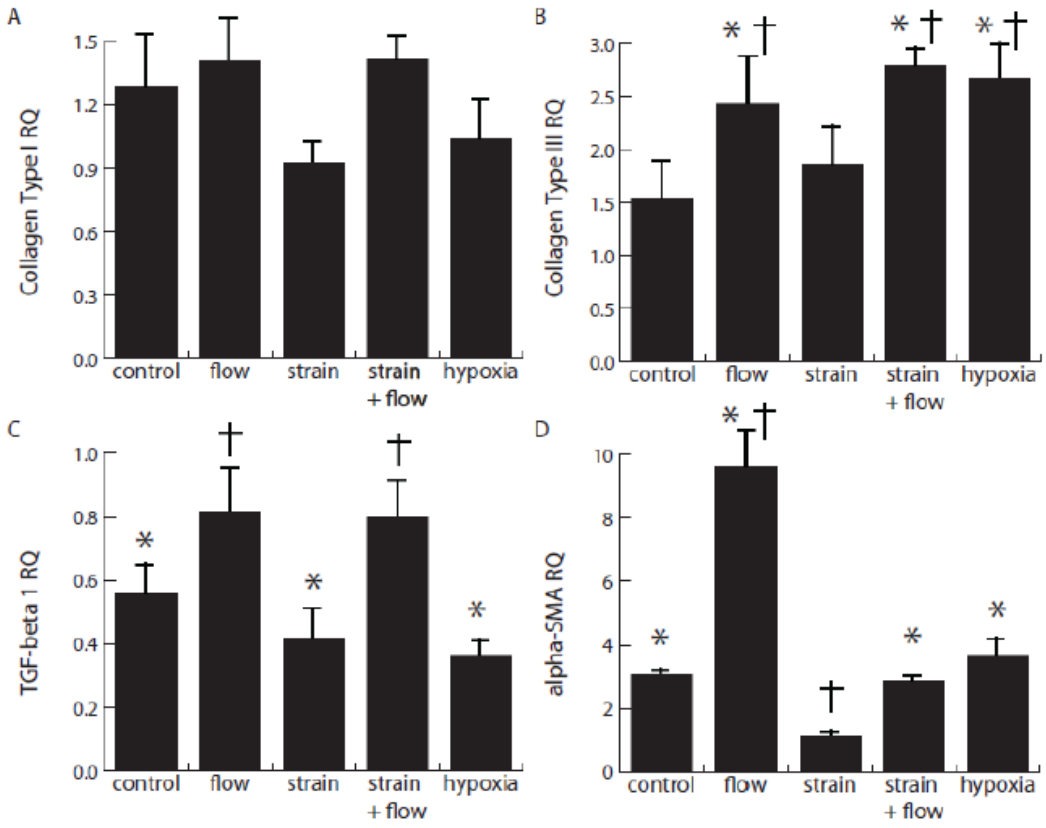

Figure 4.15 – **Message level response to exogenous stimuli:** Influence of hypoxia and mechanical stimuli produced by cross flow and cyclic strain on message levels of collagen type I (A), collagen type III (B), TGF-β (C), and α-SMA (D) after 48 h of stimulation, indicating significant differences compared to initial control levels (*: $p<0.05$) and showing significant differences compared to 48 h controls (†; $p<0.05$). Relative quantity (RQ) is defined as $2^{-\Delta\Delta CT}$, where C_T is the cycles to threshold, double normalized to both GAPDH and the initial control levels.

Cross flow alone produced a marked increase in α-SMA message levels compared with both the initial control level and that of samples exposed to cyclic strain. The competing effects of cross flow and cyclic strain were most apparent in the samples exposed to a combination of both fluid flow and cyclic strain, which resulted in no significant change from the 48 h controls (Fig. 4.15D). Hypoxia caused a significant increase in collagen type III and α-SMA message, but not in TGF-β1 levels. Assessment of DNA content in these constructs showed that cell numbers

were constant across samples, and therefore the observed effects were not a result of changes in proliferation or cell death (Figure 4.16).

Immunohistochemistry was performed to provide insight into the mechanical influences on cell phenotype (Fig. 4.17). Previous studies indicated that the myofibroblast transition is associated with a distinct morphology characterized by prominent stress fibers and a less stellate shape. The observed increase in α-SMA gene expression was corroborated by the presence of distinct stress fibers that stained for α-SMA. This effect was evident in control samples, which exhibited increased positive staining for α-SMA over 96 h (Fig. 4.17a-c). Cells exposed to cross flow exhibited prominent stress fibers, a more stellate morphology, and markedly increased α-SMA staining compared to the other conditions (Fig. 4.17d).

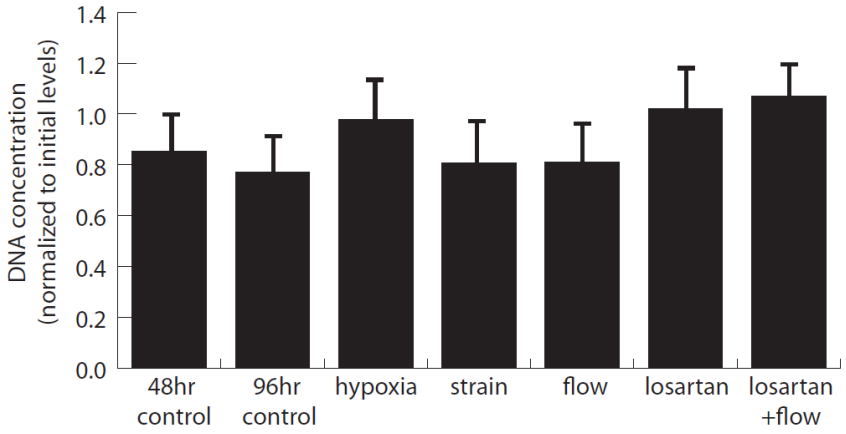

Figure 4.16 - **Cell proliferation assay:** DNA concentrations quantified using the picoGreen assay were normalized to initial levels for many of the testing conditions. No significant differences were found.

Cells exposed to cyclic strain, both with and without the presence of cross flow, showed decreased expression of α-SMA compared to the cross flow samples (Fig. 4.17e, f). Moreover, the cells exposed to strain appeared to align with the direction of strain, though they exhibited less prominent stress fibers compared to the 96 h controls and cells exposed to flow alone. These

results support the qRT-PCR data for α-SMA message levels, further implicating that cross flow stimulates and cyclic strain attenuates the myofibroblast transition.

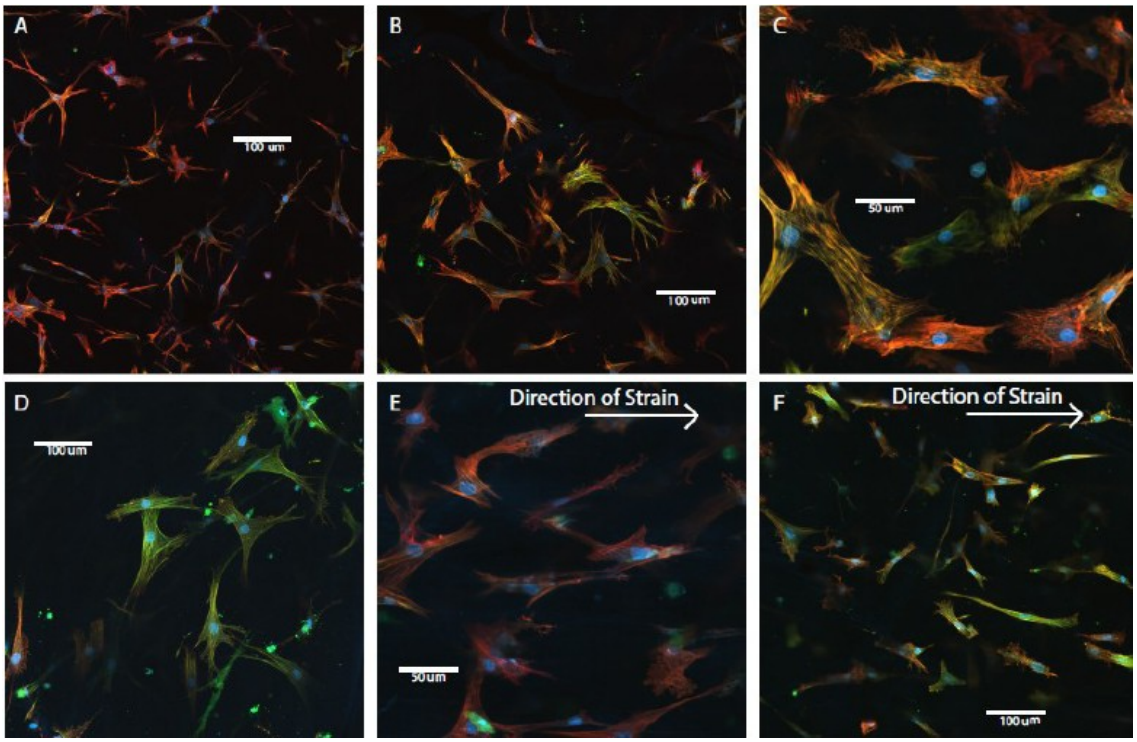

Figure 4.17 – **Cell morphology and α-SMA protein expression in response to mechanical stimuli:** Immunofluorescence images of embedded fibroblasts for initial, 48 h, and 96 h controls (A-C) and for flow (D), strain (E), and strain + flow (F). Blue indicates DAPI staining of the nucleus, red shows Texas red phalloidin staining of fibrillar actin, and green represents FITC-stained anti-α-SMA. Note scale bars and higher magnification in panels C and E, compared to A, B, D, F.

The role of the AT1R and TGF-β signaling pathways in cardiac fibroblast mechanotransduction

Since the response of cardiac fibroblasts exposed to cross flow and cyclic strain revealed distinct and opposing effects of these two types of mechanical signal, we performed experiments to further examine signal transduction in these cells. In particular, we blocked TGF-β and AT1R-mediated signaling to determine the roles of these pathways in the cellular response, as shown in Figure 4.18. Blocking of TGF-β to inhibit autocrine and paracrine signaling by the cells through

this growth factor did not affect collagen type I message levels, both in the presence or absence of cross flow (Fig. 4.18A). However, inhibiting TGF-β attenuated the cross flow-induced increase in both collagen type III and TGF-β1 expression (Fig. 4.18B-C). The presence of the antibody did not affect levels of either marker in the absence of flow. However, blocking TGF-β not only prevented the cross flow-induced increase in α-SMA expression, but also reduced the message levels to initial control levels both with and without cross flow (Fig. 4.18D), suggesting that cross flow might be activating a separate pathway.

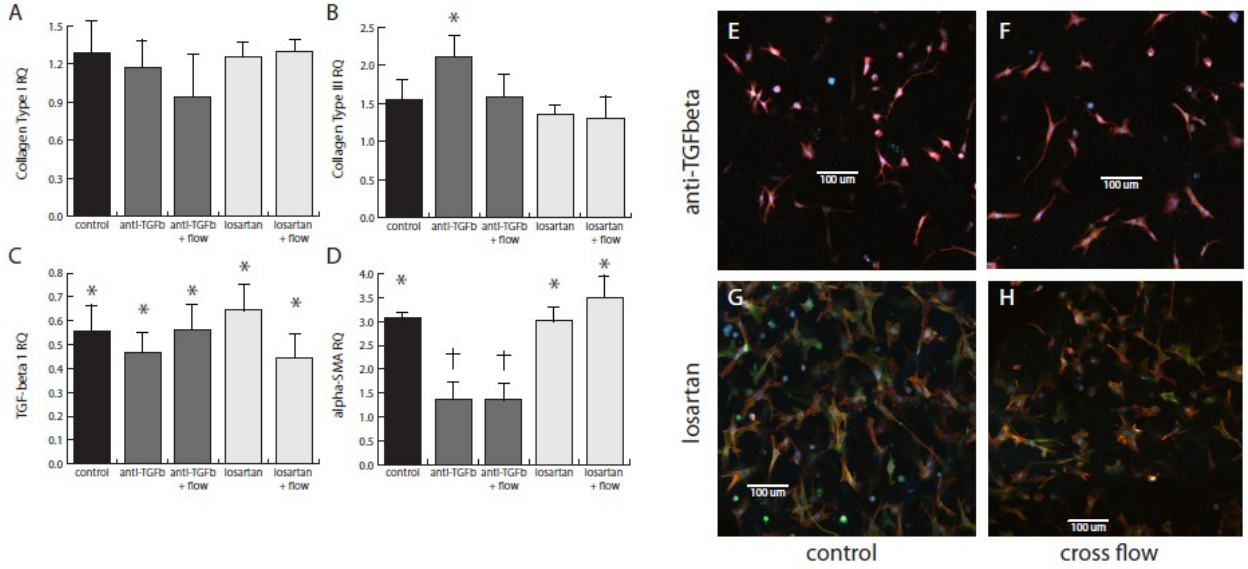

Figure 4.18- **Blocking TGF-β signaling and AT1R function:** Effects of inhibition of AT1R and TGF-β on message levels of collagen type I (A), collagen type III (B), TGF-β1 (C), and α-SMA (D), using a pan-specific TGF-β blocking antibody (dark grey bars) and the AT1R antagonist, losartan (light grey bars). Immunofluorescence images of cardiac fibroblasts treated with anti-TGF-β (E, F) and losartan (G, H) at both the 48 h control (E, G) and cross flow conditions (F, H). Blue corresponds to DAPI, red to phalloidin, and green to anti-α-SMA. All images are 600 x 600 μm.

TGF-β signaling is known to be enhanced by activation of angiotensin II receptors, and AT1R in particular has been linked to flow-induced mechanotransduction [Zou, 2004]. We therefore examined the role of AT1R in the cross flow response by blocking this receptor using

losartan. The antagonist had a similar effect to blocking of TGF-β on the message levels of collagens type I and III and TGF-β1 (Fig. 4.18A-C), providing further evidence for a relationship between AT1R-activated signaling pathways and the production of TGF-β1 by the cell for autocrine/paracrine signaling. In contrast to the TGF-β blocking antibody, the addition of losartan did not affect the baseline increase in α-SMA message levels (Fig. 4.18D). However, the presence of losartan in the perfusing media did block the flow-induced effect on message levels (Fig. 4.18D). These results suggest that cross flow may act through AT1R, which when activated elicits TGF-β1 expression and thereby initiates the myofibroblast transition. Immunofluorescence was also used to validate the observed trends in α-SMA message levels, and to gain insight into the effect of these blocking agents on cell morphology. Cells treated with the TGF-β blocking antibody exhibited similar morphology and α-SMA expression to the initial controls (Fig. 4.18E,F). Losartan-treated cells appeared similar to the 48 h controls (Fig. 4.18G,H). This is evident for both the control conditions (Fig. 4.18E,G) and for the cells exposed to cross flow (Fig. 4.18F,H).

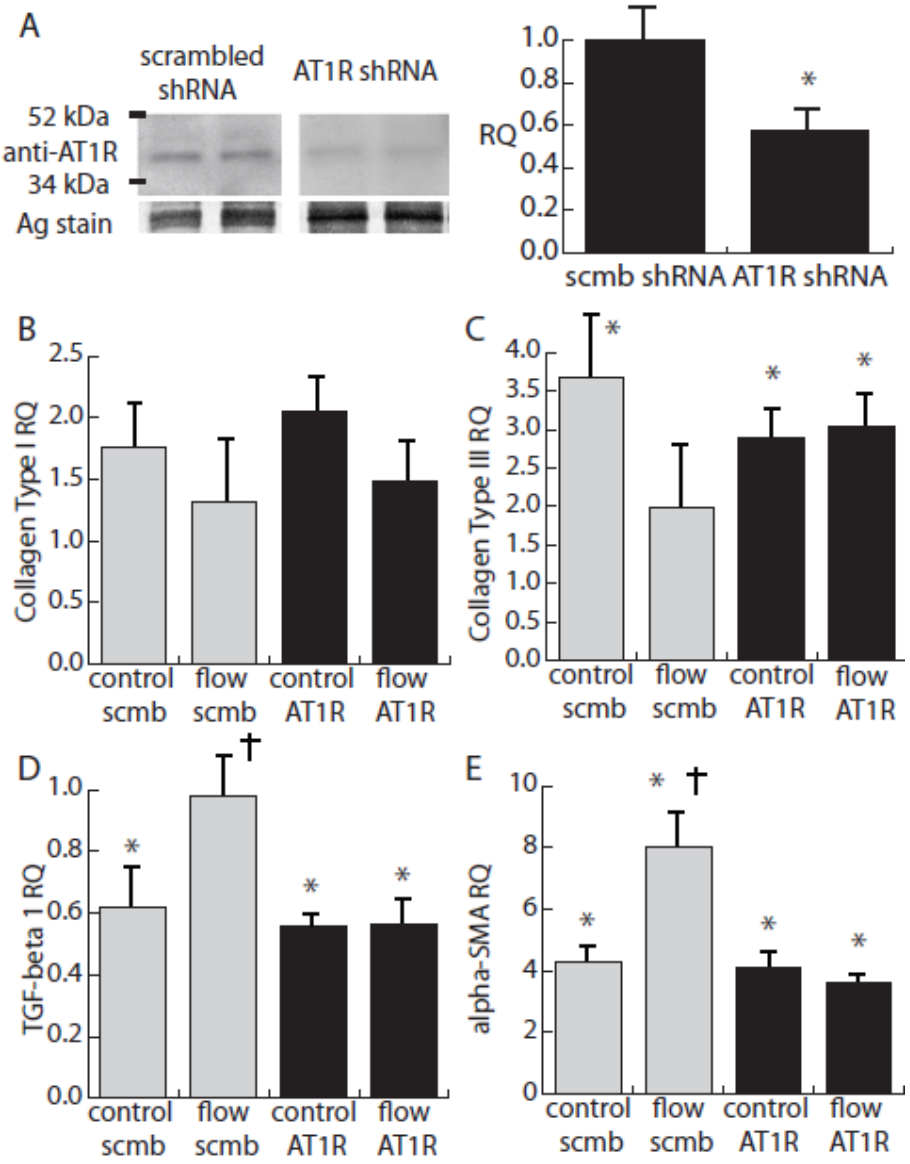

Figure 4.19 – **AT1R shRNA-mediated knockdown:** The effects of shRNA knockdown of AT1R on flow-mediated phenotype shifts in cardiac fibroblasts. A) Immunoblot verifying knockdown of AT1R. B-E) Message levels of key phenotype markers in response to treatment with AT1R shRNA and scrambled shRNA, as well as cross flow and 48 h controls. Relative quantities were normalized to initial controls treated with scrambled shRNA. AT1R shRNA had no significant effect on initial controls infected with scrambled shRNA. * denotes significance from initial levels, and + denotes significance from control levels.

Losartan may affect the TGF-β receptor and a previous study demonstrated its ability to block angiotensin II type 2 receptors [Habashi, 2011]. Therefore, since losartan is capable of

blocking both AT and TGF-β pathways, demonstration of the role of AT1R-mediated signaling in the cellular response required more specific targeting of the receptor. Lentiviral transduction was used to insert a shRNA against AT1R into cardiac fibroblasts, and results are shown in Figure 4.19. AT1R shRNA knocked down AT1R levels to around 55% of the levels present in cells infected with a scrambled shRNA (Fig. 4.19A). Cells treated with shRNA were then exposed to the cross flow regimen. Figures 4.19B-E show message levels for samples exposed to shRNA (AT1R and scrambled) at the 48 h control and the cross flow condition. In general, cells infected with scrambled shRNA responded similarly to non-infected cells, with the exception of a statistically significant increase in collagen type I and III expression for the 48 h time point (Fig. 4.19B-C). Moreover, cross flow did not significantly increase collagen type I or III expression relative to initial controls (Fig. 4.19C). Scrambled shRNA produced the same patterns of TGF-β1 and α-SMA expression as non-infected cells (Fig. 4.19D-E). In general, the incorporation of the AT1R shRNA produced similar effects to losartan treatment. However, the combination of AT1R shRNA and cross flow caused a significant increase in collagen type I compared to initial control levels (Fig. 4.19B).

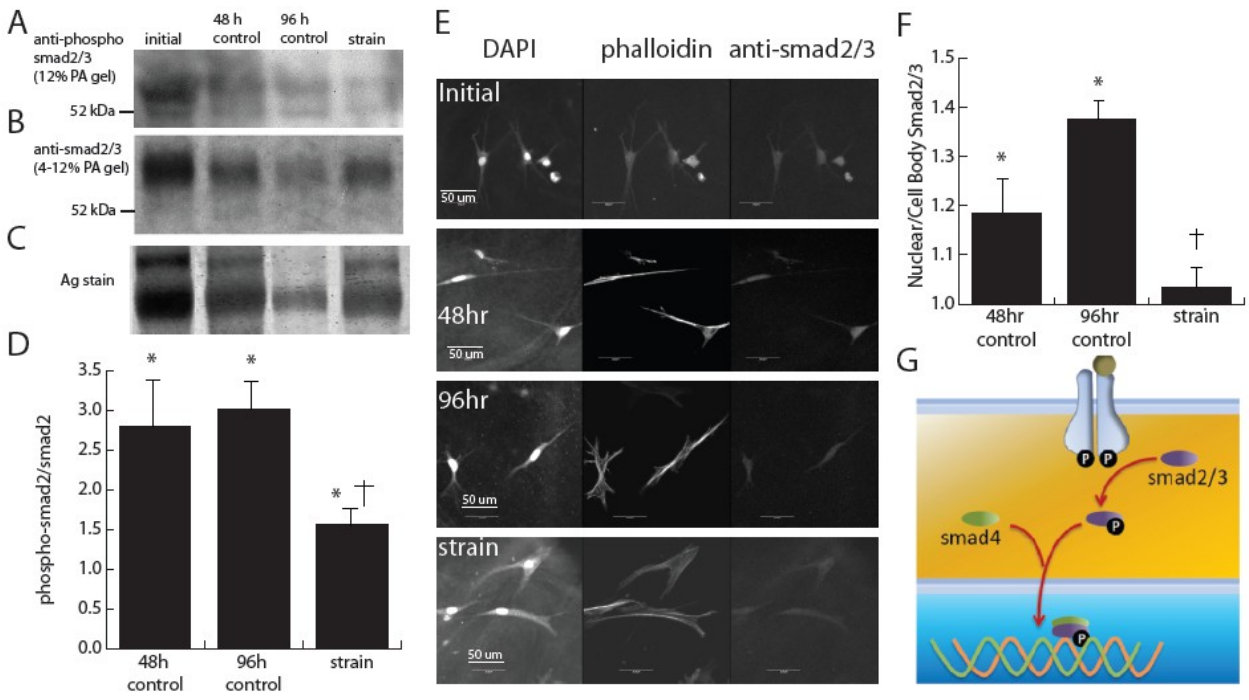

Figure 4.20 - **Effect of cyclic strain on smad2 phosphorylation:** Western blot of cardiac fibroblasts exposed to cyclic strain using smad2/3 (A) and phospho-smad2 (B) antibodies. Representative lanes from silver staining (C) indicated uneven protein loading caused by separation of cellular protein from the collagen hydrogel. The ratio of phosphor-smad2 to total smad2 is quantified in (D). Immunohistochemistry of smad2/3 and its localization to the nucleus during phosphorylation. E) shows images of cardiac fibroblasts stained for smad2/3 and F) shows quantification of nuclear localization. G) illustrates how smad2/3 is shuttled into the nucleus to affect transcription.

Moreover, AT1R shRNA prevented a significant increase in collagen type III expression in the 48 h control samples (Fig. 4.19C). Nonetheless, AT1R shRNA prevented the rise in TGF-β1 message levels to the initial control levels with the addition of cross-flow (Fig. 4.19D). Similarly, AT1R shRNA attenuated the rise in α-SMA expression in response to cross flow, while still allowing for the baseline increase in this message level at the 48 h time point. Taken together, these results suggest that AT1R directly participates in the transduction of the mechanical stress exerted by cross flow.

The effect of cyclic strain on smad2 phosphorylation

Because our results suggested that cross flow acts through AT1R to facilitate the myofibroblast transition, experiments were conducted to determine if cyclic strain also works through a TGF-β-related pathway in order to clarify the degree and type of crosstalk between these stimuli. In particular, we examined the phosphorylation of smad2, a downstream effector of TGF-β, in cells exposed to cyclic strain, as shown in Figure 4.20. Immunoblotting (Fig. 4.20A-B) showed a band at 60 kDa, which represents smad2 levels (the 52 kDa band in the phospho-smad blot represents cross-reactivity of the antibody with smad3). The amount of protein varied between blots (Fig. 4.20C) due to the difficulty in isolating cellular proteins from the protein-based hydrogels, however silver staining showed that the relative levels of smad2 were not significantly different across all samples. Comparison of the ratio of phosphorylated to total smad2 (Fig. 4.20D) showed that relative phosphorylation of smad2 increased in control samples as time progressed, which mirrored the observed increases in collagen type III and α-SMA message levels. Interestingly, the application of cyclic strain attenuated the phosphorylation to initial control levels, which also matched the effect of strain on α-SMA message levels. To verify the results of immunoblotting, the levels of smad2 phosphorylation were also examined using immunohistochemistry, as shown in Figure 4.20E. Previous studies have shown that once phosphorylated, smad2/3 is shepherded into the nucleus by smad4 to mediate transcription (Fig. 4.20G). Examination of the ratio of fluorescence intensity between the nucleus and cytoplasm (Fig. 4.20F) showed that the 48 and 96 h controls had significantly higher levels of phosphorylated smad2 compared to initial controls and cyclically strained samples, which aligns with the immunoblotting results. Overall, these data suggest that the observed changes phosphorylated smad2 were due to transduction of the mechanical strain stimulus.

4.4. Poroelastic model to describe cell-seeded gel mechanics

Pressure and relative fluid velocities for the strain only condition

Applying a 1 Hz, 5% cyclic strain in combination with 10 μL/min of cross flow produces a substantial difference in fibroblast message levels, morphology, and α-SMA protein expression compared to gels exposed only to strain. A poroelastic model was chosen to determine the effect of cross flow on fluid pressure, relative fluid velocity, and fluid shear stress distributions in the hydrogels. First, these parameters were calculated for the strain only condition. Figure 4.21 shows the fluid pressure in a 5% cyclically strained hydrogel at three discrete times in the cycle (t = 0, 0% strain (black), t = 0.25s, 2.5% strain (orange), t = 0.5s, 5% strain(green)). As the figure shows, there is a considerable pressure gradient at the ends of the gel (y = 0 mm, y = 1 mm), due to the open boundaries with the surrounding fluid. The magnitude of this gradient is highest at 2.5% strain, compared to 0 and 5% strain. This result is intuitive since the strain rate is also at a maximum at 2.5% strain rate, due to the sinusoidal waveform at the cycled boundary.

As shown in equation 20, the shear stress on cells within the hydrogel can be estimated by a direct multiple of the relative fluid velocity. Figure 4.22 shows the shear stress profile along the y axis at the x centerline for three different points in the strain cycle. As could be predicted from the pressure profile, the highest levels of shear stress occur at the ends of the gel on the y axis. In fact, there is zero shear stress in the midpoint of the gel along the y axis, the area most removed from the open boundaries.

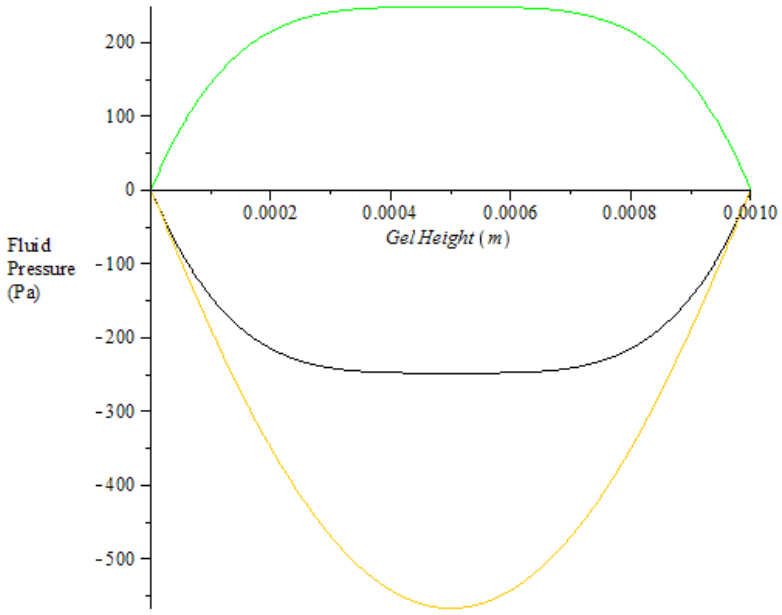

Figure 4.21 - **Fluid pressure during cyclic strain:** Fluid pressure along the y axis of the hydrogel, at the x axis centerline for a 5% strain, 1Hz cycle. Black: 0% strain, orange: 2.5% strain, green: 5% strain

This result is caused by exchange between the surrounding fluid outside the gel with interstitial fluid within the hydrogel. The model predicts shear stresses from about -2 dyn/cm^2 to 2 dyn/cm^2, which is within the range of physiological values of interstitial fluid flow in the wall of arteries [Wang, 1995].

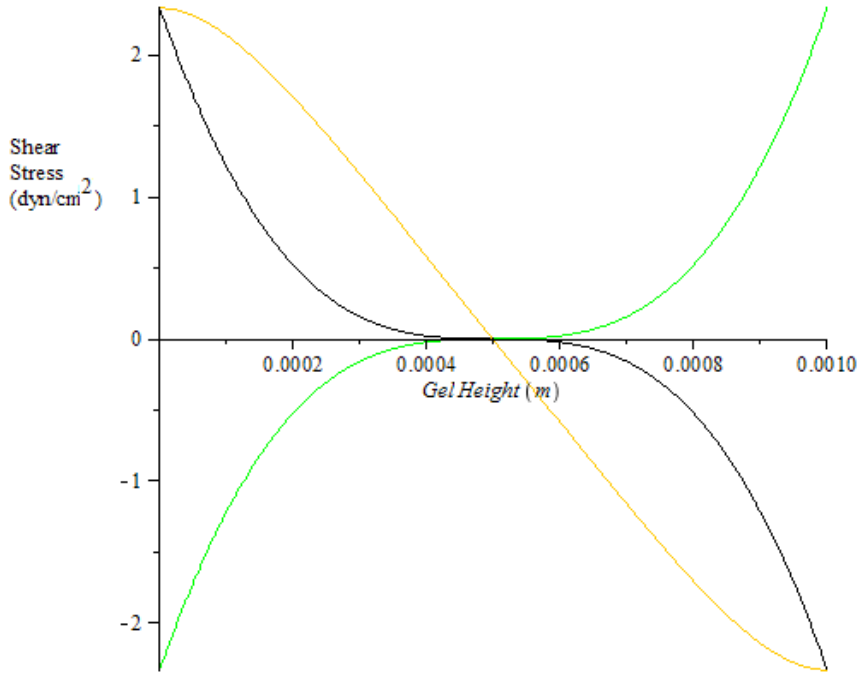

Figure 4.22 – **Estimated shear stress during cyclic strain:** Fluid shear stress along the y axis of the hydrogel, at the x axis centerline for a 5% strain, 1Hz cycle. Black: 0% strain, orange: 2.5% strain, green: 5% strain

These results indicate that cyclic strain induces substantial interstitial fluid flow within the hydrogels. But because the gels are being strained, the cells are also exposed to solid stress from the deformation. Figure 4.23 shows the solid displacement of the gel along the y axis at the x centerline of the gel. Due to the Poisson's ratio of the hydrogel, the cells are also strained in the y direction during the strain cycle. This deformation is in addition to the strain in the x direction caused by the cycling boundary condition. Hence, the total stress on cells within the hydrogel has both a substantial fluid stress component as well as a solid stress component. As the gel is positively strained in the x direction at 2.5% strain, there is a totally negative displacement in the y direction. The maximum displacement occurs at the top surface of the gel. The addition of cross flow to the hydrogel does not affect the y displacement of the gel, hence Figure 4.23 is identical to the displacement distribution for the addition of cross flow.

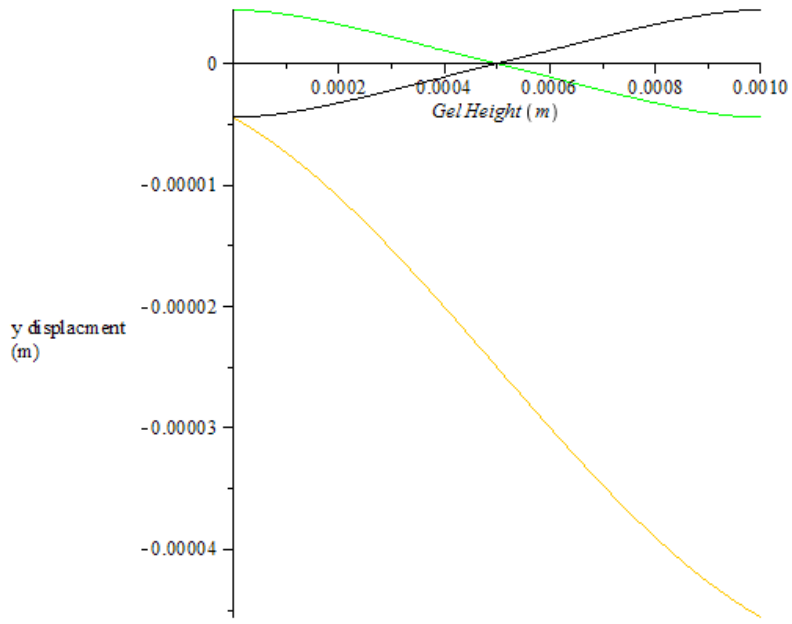

Figure 4.23 – **y displacement during cyclic strain in the x direction:** Solid displacement in the y direction of the hydrogel undergoing a 5%, 1 Hz tensile cyclic strain. Black: 0% strain, orange: 2.5% strain, green: 5% strain.

Even though cross flow does not affect the solid mechanics of the hydrogel, the model can analyze the effect of adding cross flow to the fluid pressure and shear stress distributions. To facilitate the addition of cross flow, the only change to the model is the addition of a pressure gradient along the y axis of the gel. The results of the altered pressure distribution are given in Figure 4.24. The distribution appears to be quite similar to the distribution for strain only (Fig. 4.21), with the pressure shifted up at the bottom boundary, y = 0 mm. For example, the pressure gradients are again highest at the edge of the gels (y = 0 mm, y = 1 mm). In contrast to the strain only condition, there does exist a small pressure gradient near the center of the gel (y = 0.5 mm), caused by the addition of the pressure gradient.

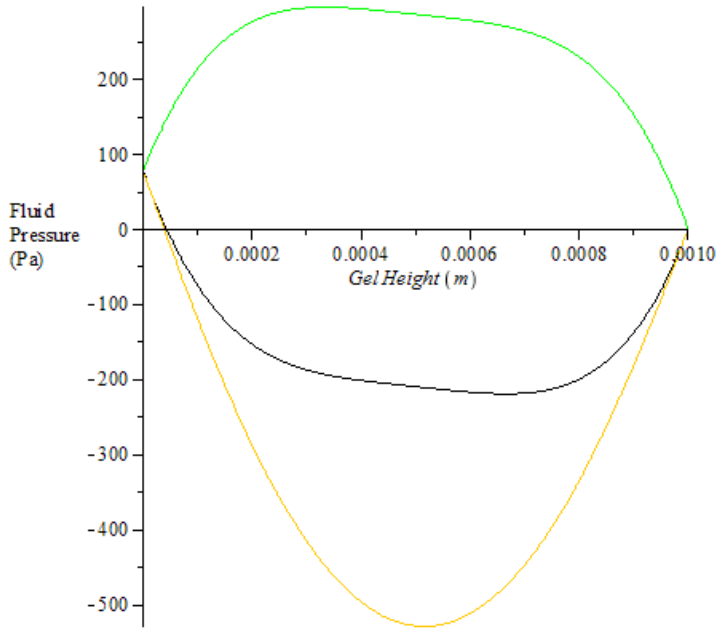

Figure 4.24 - **Fluid pressure during cyclic strain and applied cross flow:** Fluid pressure within the hydrogel undergoing a 5%, 1 Hz cyclic strain in addition to a 77.6 Pa cross flow pressure gradient. Black: 0% strain, orange: 2.5% strain, green: 5% strain.

Figure 4.25 shows the effect of the cross flow on the fluid shear stress on the cells embedded in the hydrogel. Again, there is not much difference between these distributions and those calculated for strain only (Fig. 4.22). However, cells at the midpoint of the gel (y = 0.5mm) are exposed to a constant 0.1 dyn/cm^2 fluid shear stress caused by the cross flow. Hence, the cross flow produced a shear stress that is about 20 times less than the flow-induced stress caused by the 5% cyclic strain. This result underscores the porosity of the hydrogels, and the high level of coupling between the solid and fluid mechanics of the poroelastic medium.

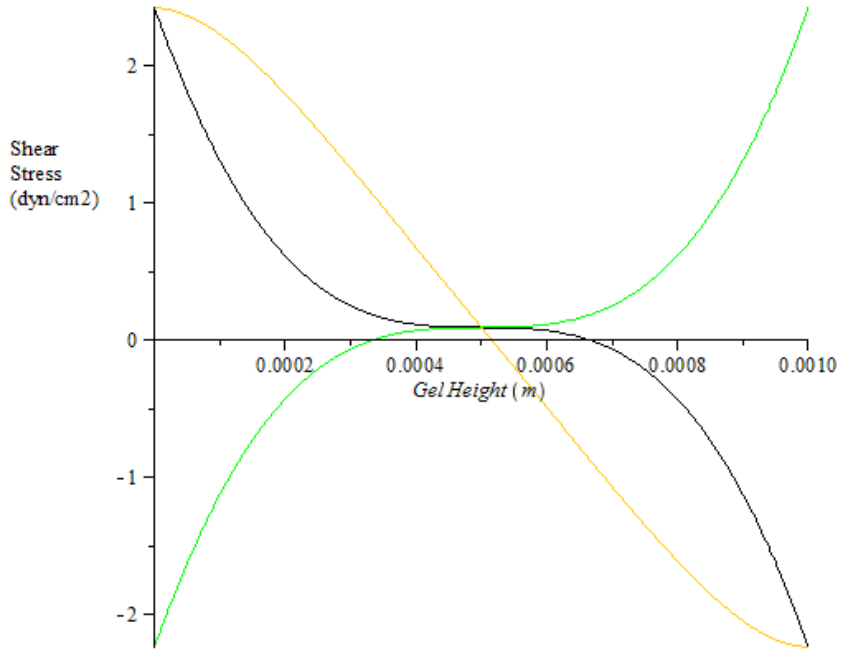

Figure 4.25 – **Estimated shear atress during cyclic strain and applied cross flow:** Fluid shear stress within the hydrogel undergoing a 5%, 1 Hz cyclic strain and 77.6 Pa cross flow pressure gradient. Black: 0% strain, orange: 2.5% strain, green: 5% strain.

The results of the model indicate that there is considerable interstitial fluid flow produced by strain, but not substantial strain produced by fluid flow. Considering that cross flow alone had such a significant effect on α-SMA expression compared to strain alone (Fig. 4.15), this result suggests that cyclic strain may be the determining stimulus on fibroblast phenotype. The mechanism underlying this response may be explained by the effect of cyclic strain on smad2 phosphorylation. It is also possible that the transient nature of the cyclic strain may be causing a distinct response in the fibroblasts, compared to the constant cross flow. To test this possibility, a 1 Hz pulsatile cross flow of 10 μL/min was applied to the gels. Figure 4.26 shows that the pulsatile cross flow does cause increased α-SMA protein expression in the cells. However, the morphology does appear to be different from the constant cross flow results (Fig. 4.17).

Nonetheless, the increased α-SMA expression indicates that it is the solid stress produced from cyclic strain that is the determining factor in fibroblast response, not any transient effect.

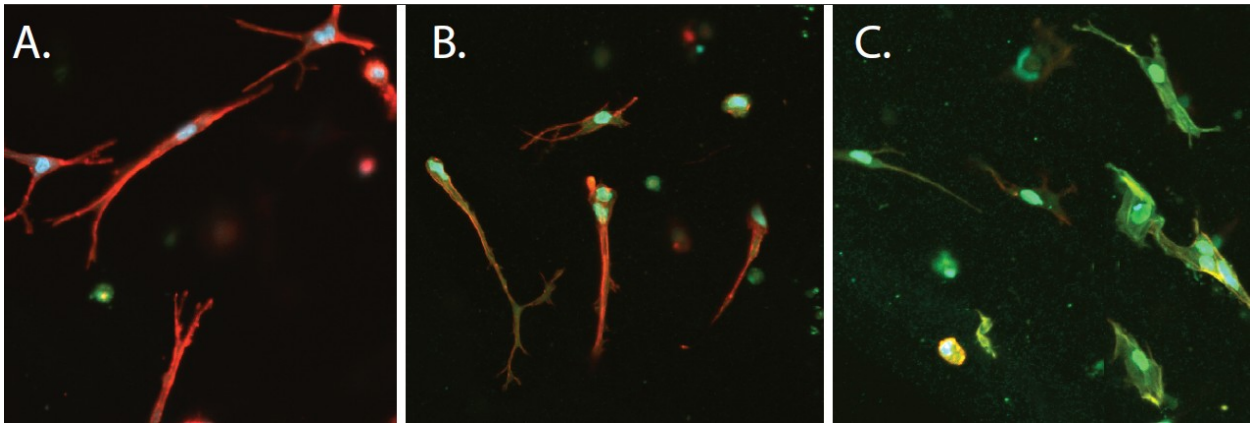

Figure 4.26 - **Effect of pulsatile flow on fibroblast morphology and α-SMA:** Immunofluorescence of cells at the initial time point (A), at 48hr controls (B), and after exposure to pulsatile (1 Hz) 10 μL/min cross flow. Blue: DAPI, Red: Texas Red-phalloidin, Green: anti-α-SMA-FITC. All images are 300 x 300 μm.

4.5. MSC injection and paracrine effect in fibroblast-seeded gels

The effect of MSC injection on fibroblast activation

The primary indicator of paracrine action of the injected MSC is the level of activation of surrounding cardiac fibroblasts seeded into the collagen hydrogel. The previous results indicated that fibroblasts seeded into the hydrogel have a baseline level of activation, as indicated by increased expression of collagens I and III, TGF-β, and αSMA, and augmented activation by fluid flow and hypoxia. Hence, fibroblasts removed from the injection site by at least 0.25 mm were immunostained for αSMA-FITC and visualized with a confocal microscope. The results are shown in Figure 4.27. For all time points and testing conditions, the morphology of the fibroblasts does not appear to change substantially with the exception of cells exposed to hypoxia, which appear to not spread as many cell processes into the extracellular matrix. There appears to be slightly higher αSMA expression at the initial time point and flow condition

compared to the other samples. Nonetheless, large stress fibers and high levels of positive αSMA staining appear to be absent from the cells, indicating a deactivation of the myofibroblast transition.

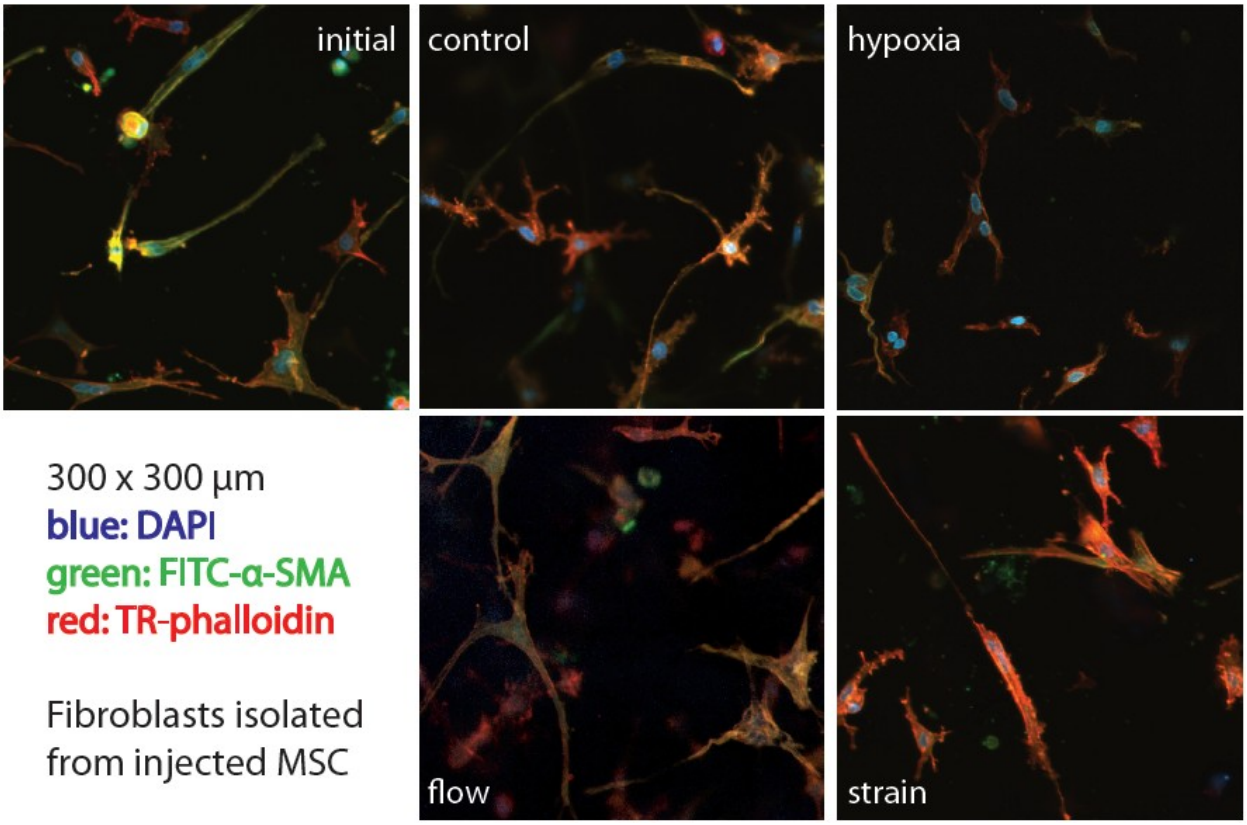

Figure 4.27 – **Effect of MSC injection on fibroblast morphology and α-SMA expression:** Immunofluoresence of cardiac fibroblasts isolated from the injection area for different testing conditions. Each image is 300 x 300 µm. DAPI is used to visualize the nuclei, Texas Red-phalloidin for the actin cytoskeleton, and FITC conjugated anti-α-SMA to observe the myofibroblast transition.

In order to quantify the fibroblast response, portions of the hydrogel removed from the injection site were homogenized to collect RNA for qRT-PCR. The results of the message level analysis are given in Figure 4.28. For all the messages measured, none of the testing conditions produced a significant increase from the initial control levels. In fact, with the exception of the

αSMA message in response to flow, all the messages were actually significantly downregulated compared to the initial time point. Interestingly, the addition of flow caused a significant decrease in collagens I and III message compared to control. Moreover, hypoxia nearly extinguished TGFβ levels in these cocultured fibroblasts. These message levels contrast starkly with the levels produced by fibroblast-only gels exposed to the identical testing conditions. Overall, the results indicate that not only does the addition of MSC attenuate fibroblast activation, but it appears to reverse the fibroblast to myofibroblast transition.

MSC response to mechanical and biochemical stimulation

Once implanted in the collagen gel, the MSC line the sides of the injection cone and attach to either the surrounding collagen gel or form cell-cell contacts. Over time, the MSC migrate out of this initial cone and into the surrounding collagen hydrogel. To understand how

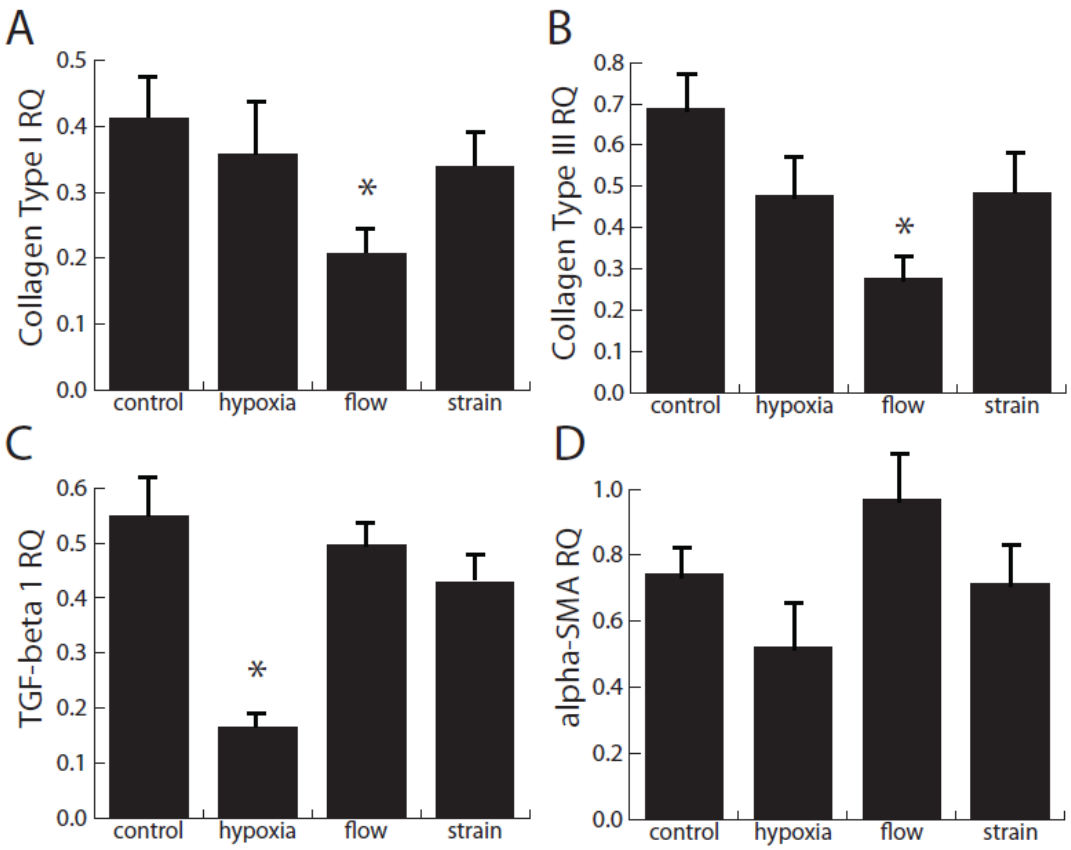

Figure 4.28 - **Message levels of fibroblasts isolated from the injection site:** This data complements the immunofluorescence images in the previous figure. Four markers for the myofibroblast transition were measured and compared to initial control levels (a * denotes significance from the control test condition, all levels are significant from initial levels except αSMA in response to flow).

specific stimuli affect this migration and the expression of cd90, a stem marker, immunofluoresence images are taken at the cone-gel interface. The results are summarized in Figure 4.29. At the initial time point, there is minimal migration because the stem cells have only been present in the gel for 12 hours. In the absence of stimulation, the control cells indicate that the MSC migrate regardless, but with no loss to the cd90 expression. In the presence of hypoxia, the migration of the stem cells is increased significantly from control samples, and again the stem marker is maintained in the cells. While both fluid flow and cyclic strain increased migration significantly compared to controls, mechanical stimulation appeared to attenuate the expression of cd90 within the stem cells. The phalloidin stain indicates that there is no substantial change in the morphology and distribution of the surrounding cardiac fibroblasts.

The migration distance of the stem cells is represented by a dotted line in Figure 4.29, and these distances are quantified in Figure 4.30. As expected from the immunofluorescence images, the migration distance of MSC is maximized by stimulation with hypoxia. Interestingly, mechanical stimulation by both interstitial fluid flow and cyclic strain produces statistically the same levels of migration. All stimuli produced significantly higher migration distances than control and initial levels. The highest migration distance approached 500 μm, which translates to an average cell velocity of 0.139 μm/s. Interestingly, this is approximately the same average velocity as the initial time point, which migrated about 100 μm in a time of 12 hours. This calculation suggests that only hypoxia is able to sustain the initial migration averaged velocity.

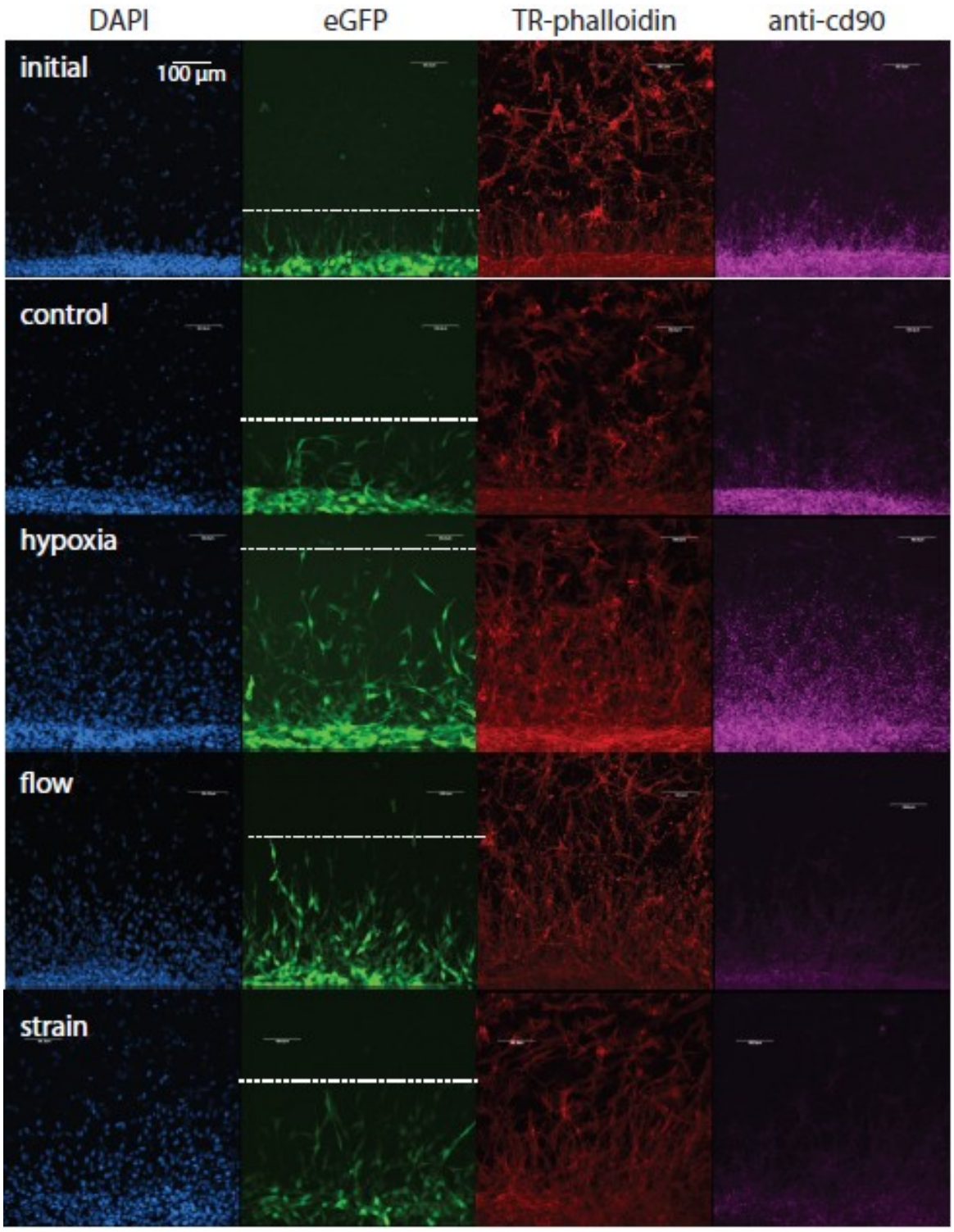

Figure 4.29 - **A summary of the MSC response to different conditions:** Each row represents a testing condition, and each column a specific fluorescence channel. DAPI and Texas Red phalloidin were used again, in addition to a cd90 antibody. MSC could be distinguished because of the GFP transfection. Dotted lines represent the calculated penetration distance.

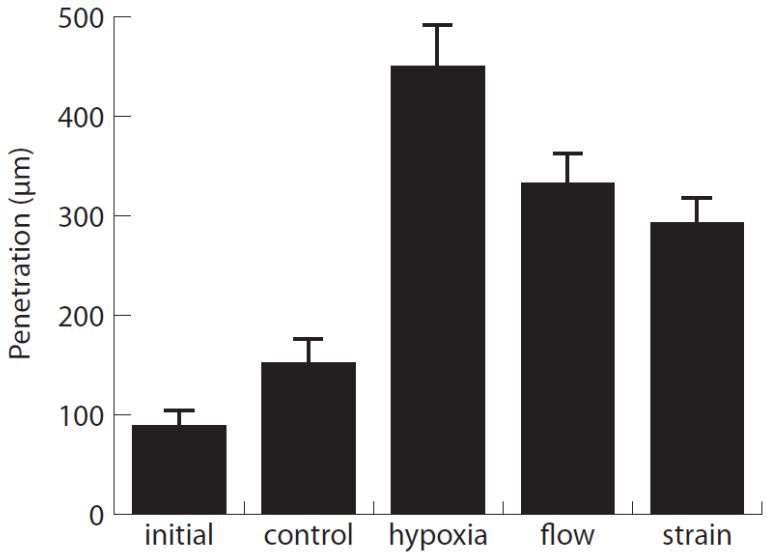

Figure 4.30 - **MSC penetration in response to exogenous stimuli:** Quantification of the penetration distance of the MSC from their initial injection cone into the cell-seeded collagen gel 48 hours after the initial time point. This penetration can be observed visually in Figure 4.29.

Paracrine release of VEGF and IGF-1 in stimulated cocultures

Having demonstrated that the injected MSC affect fibroblast activation, ELISAs were conducted to identify which paracrine factors were responsible for this beneficial effect. Supernatants from coculture gels as well as from gels populated only by fibroblasts were analyzed using ELISAs. To determine the levels produced by the MSC, levels from the coculture gels were subtracted from the fibroblast-only gels.

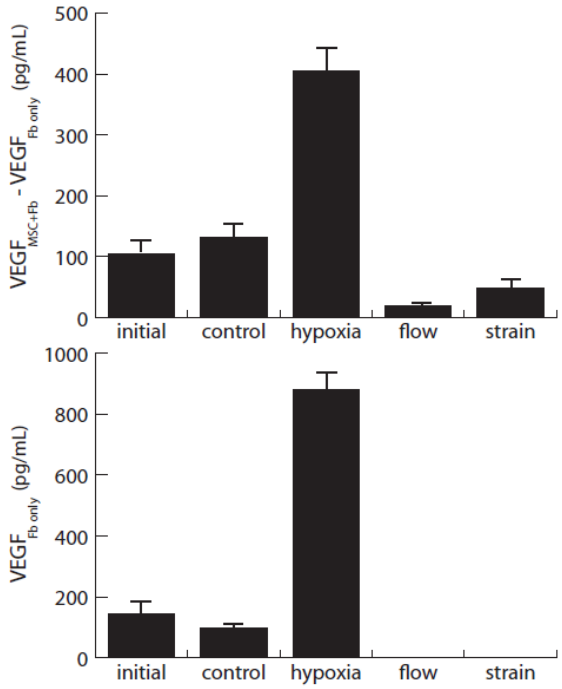

Figure 4.31 -**VEGF release by the MSC within the collagen gel:** Release of this factor was measured in gels containing only fibroblast gels (bottom plot), in order to determine the contribution of injected MSC (top graph).

This normalization does not necessarily yield the amount of growth factor produced by the MSC, because the presence of MSC most likely affects fibroblast paracrine release. Nonetheless, it provides a measure of the effect of MSC on total paracrine release by these two cell types. Two growth factors commonly associated with the paracrine effect of implanted MSC were analyzed, VEGF and IGF-1. The results of the VEGF ELISA are shown in Figure 4.31. VEGF release increases with time in the MSC, as evidenced by control levels exceeding the initial levels. Hypoxia stimulated substantial VEGF release from fibroblasts and from implanted MSC. Interestingly, mechanical stimulation in the form of both interstitial fluid flow and cyclic strain decreased the VEGF levels released by both MSC and fibroblasts below controls and the initial levels. The results suggest that VEGF is an important mediator in response to hypoxia, but not mechanical stimulation.

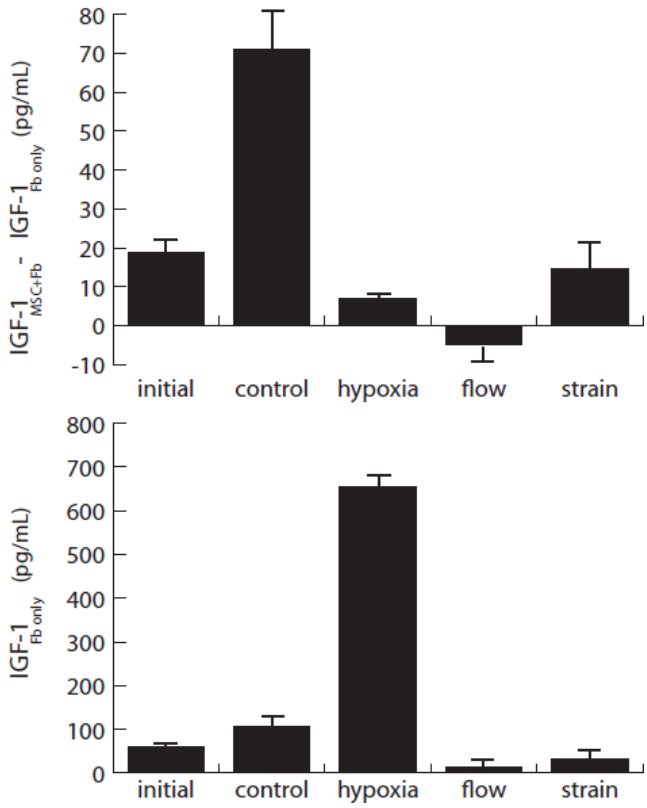

Figure 4.32 - **IGF-1 release by the MSC within the collagen gel:** Release of this factor was measured in gels containing only fibroblast gels (bottom plot), in order to determine the contribution of injected MSC (top graph).

Figure 4.32 shows the results of the IGF-1 ELISA. The production of IGF-1 by fibroblasts alone mirrored the release of VEGF stimulated by the testing conditions. However, in contrast to the VEGF ELISA, MSC did not appear to release much of this growth factor. In fact, no testing condition produced more than 100 pg/mL in the implanted MSC. Fibroblasts in response to hypoxia produced very high (> 600 pg/mL) levels of the growth factor. Mechanical stimulation from both interstitial fluid flow and cyclic strain produced negligible IGF-1 concentrations from the fibroblasts. As mentioned, the addition of MSC to the gels did not substantially increase the levels of this growth factor. Average IGF-1 levels in response to both

hypoxia and fluid flow were less than levels produced by the fibroblasts. Only the control testing condition resulted in any significant increase over the initial levels. The results of this ELISA indicate that IGF-1 production is not stimulated by either hypoxia or mechanical stimulation.

Chapter V

Discussion

The results presented in this dissertation generally support the two hypotheses stated in the introduction: first, mechanical stimulation dictates the myofibroblast transition through TGF-β-related signaling pathways, and second, MSC modulates cardiac fibroblast phenotype through release of cardioprotective and angiogenic paracrine factors. The myofibroblast transition was first studied in released and constrained collagen gels in order to understand the response of these primary cells to changes in substrate stiffness and culture conditions. After characterizing the cell response, an apparatus able to apply both interstitial fluid flow and cyclic strain was used to determine how fibroblasts responded to specific mechanical stimuli. Experiments were conducted to determine the mechanisms underlying the mechanotransduction of the fibroblasts. The hydrogel mechanics during application of these stimuli were modeled using an analytical, poroelastic model. Finally, the same levels of mechanical stimuli were applied to fibroblast-seeded gels injected with MSCs to determine how specific elements of the fibrotic myocardium affect paracrine release. The results not only indicate that the mechanical stress within the myocardium is a key regulator of both fibroblast function and MSC paracrine release, but provide insight into the mechanisms by which the cells sense and respond to mechanical stimuli.

This chapter provides a detailed discussion of the results in the context and order of the specific aims. The discussion also describes how these results may explain the development of scar tissue as well as assist in the development of treatments that impede the growth of fibrotic scars in the myocardium. For example, by showing that increased matrix stiffness facilitates the

myofibroblast transition that leads to augmented matrix production, a positive feedback mechanism is identified that has implications for scar growth. Another example is the different responses of the fibroblasts to solid stress and fluid stress. The in vivo scar environment is characterized by the death of beating cardiomyocytes (reduced strain), and by the formation of disorganized microvasculature (interstitial fluid flow). Taken together, the results of the study suggest a means by which altered mechanics in fibrosis can stimulate fibroblasts to transition to myofibroblasts.

Finally, the results are discussed in the context of other published studies focusing on the myofibroblast transition and MSC paracrine release. There have been exceptional studies investigating these topics, and this chapter will detail how the results both relate and add to previously published work. For example, the introduction described extensive work conducted on the effect of mechanical stress on the myofibroblast transition in 2D systems, and on the use of conditioned medium to elucidate the effect of MSC on cardiomyocyte and fibroblast response. Moreover, in vivo studies have also addressed the myofibroblast transition and benefit of MSC injection. The following sections will address areas in which the results both confirm and contrast with earlier work.

5.1 Characterization of the myofibroblast transition in vitro

The results presented in section 4.1 revealed the individual and combined effects of serum content and matrix stiffness on the myofibroblast transition, a key event in the fibrotic process that follows myocardial infarction. The transition was assessed at multiple levels by measuring gene expression of proteins associated with this transition, as well as qualitative protein expression, cellular morphology, and cell-mediated gel compaction. Lower serum content was found to significantly increase the ability of the fibroblasts to compact the gels (Fig. 4.1A). Both

serum levels and matrix stiffness modified gene expression of α-SMA and cellular morphology (Figs. 4.2-3) as these cells transitioned to myofibroblasts. Reduced nutrient availability at lower serum concentration also modified gene expression of TGF-β, another protein linked to this transition (Fig. 4.4-5). Moreover, gels cultured in both serum levels exhibited distinct patterns in the gene expression of collagens I and III in addition to α-SMA and TGF-β. Compression testing indicated that the transition to the myofibroblast phenotype in turn affected bulk mechanical properties of the hydrogels (Fig. 4.6).

The ability of fibroblasts to cause 3D protein gel compaction has been used as a measure of the intracellular actin-myosin interaction and the resulting increase in passive contractile function which develops as fibroblasts shift their phenotype to a myofibroblast state [Poobalarahi, 2006]. Lower serum levels accelerated the rate of gel compaction, which correlated generally with the increased expression of α-SMA, a marker of the myofibroblast phenotype. Experiments in which the cell concentration was varied showed that higher fibroblast concentrations resulted in increased gel compaction. Since cell proliferation can be expected to be decreased in low serum conditions, this finding supports the conclusion that cardiac fibroblasts in 3D collagen gels can be stimulated to become myofibroblasts by limitations in nutrient availability after a myocardial infarction.

Gels exposed to 10% serum showed a greater response to gel constraint than those cultured in 5% serum. It has been shown that serum modulates the response of cardiac fibroblasts to varying mechanical environment on a 2D substrate, e.g. collagen production was found to increase with mechanical load only when cells were cultured in high serum media [Butt, 1996]. Hence, the results of this study show a similar result in the 3D environment of a collagen gel. However, there was no significant difference in message levels for the collagens or TGF-β

between released and constrained gels. Interestingly, the morphology of the cells as measured by circularity was shown to correspond directly to α-SMA expression. Low serum and gel constraint were each associated with elevated α-SMA and circularity, while only low serum stimulated an effect on both α-SMA and TGF-β for cells cultured in M199. This divergence indicates nutrient levels and mechanical stimuli each contributes to the myofibroblast transition yet these two factors may work via variations in spatial/temporal activation of common pathways and/or activation via unrelated mechanisms. More work is required to determine such mechanisms.

The response of cardiac fibroblasts to serum level also was illuminated by characterizing gene and protein expression over time in culture in 3D collagen gels. Collagen type I gene expression decreased with time regardless of serum concentration or culture media. This effect can be attributed to the fact that collagen type I is the main component of the hydrogel matrix, which may cause downregulation of expression by embedded cells. Collagen type III expression increased over time in both serum concentrations, providing further phenotypic evidence of the cellular myofibroblast transition and subsequent increase in matrix secretion. In all treatments, expression of α-SMA was initially high immediately after gel formation (6 h time point), but decreased by 24 h and then increased over time in culture. This bimodal trend mimics the change in matrix compliance. The high initial α-SMA expression levels were probably a result of culturing the cells on stiff tissue culture plastic prior to making gels. Expression decreased as the gels remodeled, but subsequently increased as the compliance of the compacting gels decreased. The mechanical testing data corroborates this increase in stiffness between the 6 h and 120 h time points. In addition, α-SMA expression appeared to lag behind TGF-β expression, which was highest at the 24 h time point, suggesting a possible autocrine or paracrine effect in promoting

the differentiation of fibroblasts to myofibroblasts. Future mechanistic studies with this 3D matrix can be utilized to better understand whether TGF-β is required for the matrix compliance-induced shift in fibroblast function.

Mechanical testing showed that the stiffness of the 3D collagen matrix increased over time in released gels, regardless of serum content. This result verified that cells in released gels were exposed to an increasingly stiffer environment. There was an effect of serum: gels cultured in low serum exhibited higher stiffness, as measured from the elastic moduli and lower loss angles than their high serum counterparts at the initial time point. The fact that serum has a significant effect is evidence of a positive feedback loop between cell phenotype and matrix stiffness: reduced serum induces the myofibroblast phenotype, which increases the stiffness of the extracellular matrix, and in turn accelerates myofibroblast development. This process is illustrated in Figure 5.1.

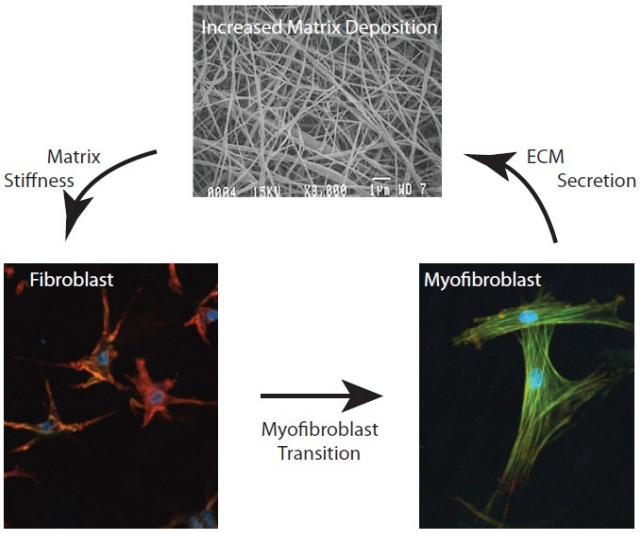

Figure 5.1 – **Fibroblast-myofibroblast positive feedback:** Summary of the positive feedback that occurs between the extracellular matrix environment and the fibroblast phenotype.

The mechanical feedback loop is likely to be an important component of the *in vivo* fibrotic process. It may be accelerated in ischemic regions with less access to serum factors and necrotic/scarred regions experiencing high stress. Thus, this process is likely to play a key role during pathophysiological cardiac remodeling and will require critical consideration for stem cell therapies targeted to heart failure.

The gene expression, morphology, and compression results of the present study suggest that there is a limit to which reduced serum content and increased matrix stiffness can initiate the myofibroblast transition. For example, the gene expression and morphology of cells cultured in reduced serum in released and constrained gels showed that the effects of serum and stiffness were not additive in increasing α-SMA expression or creating a more spherical morphology (Fig. 4.2-3). For higher serum content, the significant difference in α-SMA expression and spherical morphology between released and constrained gels lasted only for the first 24 hours (Fig. 4.2-3). Also, compression testing of released gels indicated that the effect of reduced serum content was abolished by the final time point, since there was no difference in elastic modulus or loss angle between gels cultured in 5 and 10% FBS (Fig. 4.6). These results suggest that the increased α-SMA expression caused by reduced serum reached a limit, and increasing matrix stiffness in the compacting gels could only produce increased α-SMA message levels in the higher serum data set. The results also lead to further work to determine if extraneous mechanical stimulation such as cyclic strain or interstitial flow could increase α-SMA expression beyond the levels produced by serum and matrix stiffness.

A better understanding of the cardiac fibroblast response to environmental factors is important to elucidate the causes and possible treatments of cardiac fibrosis and scarring as well as other diseases caused by unwanted tissue remodeling. Such knowledge also is important in

developing improved in vitro models of fibrosis, which can be used to study the disease and develop diagnostic and therapeutic strategies to treat the cardiac dysfunction and heart failure produced in the aftermath of myocardial ischemia. Interestingly, the cell-seeded hydrogels in this study exhibited elastic moduli in the range of in vivo fibrotic tissue [Discher, 2009], though it can be problematic to compare modulus values obtained by different test methods. Fibrosis can be studied in vivo and the process can be manipulated by the administration of pro-fibrotic factors (e.g. TGF-β, angiotensin II) or by knocking out anti-fibrotic cytokines (e.g. brain natriuretic peptide) [Tamura, 2000], but it is difficult to control all the mechanical and biological factors contributing to fibrosis in animal models. The development of in vitro testbeds, such as the hydrogel model described in the present study allows for a more controlled mechanical and chemical/hormonal environment to better understand the mechanisms responsible for cardiac fibrosis.

5.2 Application of simultaneous flow and strain

The results of section 4.2 validate the use of the PDMS apparatus to apply simultaneous fluid flow and cyclic strain to cell-seeded hydrogels. The design is based on previously described interstitial flow bioreactors [Chee Ping, 2003], with the key addition of applying simultaneous uniaxial, cyclic strain. The flexible PDMS chamber allowed for strain application and the surface could be modified to retain gel adherence over the duration of the experiment (72 – 120 h). Finite element modeling was used to determine that the main component of the applied strain was in the axial direction, though the strain applied to each of the 3D constructs was slightly higher than the global strain on the PDMS well. Because of the Poisson's ratio of the PDMS, the gels experience minimal strain in the components perpendicular to the axial direction of cyclic strain.

The results of the permeability and flow visualization experiments directly validated the approach of using an acellular gel upstream of the cell-seeded gel to distribute the fluid flow evenly across the seeded construct. The acellular gel yielded higher permeability values than the cell-seeded gel, which caused the flow to distribute prior to passing through the cell-seeded gel. It is unclear why the acellular gel has a higher permeability, since the gels are constrained at the edges by the walls of the PDMS. One possibility is that the cell-seeded gel is compacting in the y direction, which is causing the permeability to decrease. It is also possible that the fibroblasts in the cell-seeded gel are secreting their own matrix, though matrix secretion was not explicitly quantified beyond message levels of collagens I and III. Imaging and viability studies confirmed that cells survived in the 3D protein hydrogel, under both static, as well as strained and fluid flow conditions. All testing conditions produced viability levels higher than 90%. For the time span observed, the control fibroblasts showed no substantial change in viability. This result implies that nutrients within the medium were able to freely diffuse into the gels to reach the embedded cells.

The ability to apply simultaneous interstitial flow and cyclic strain has relevance to the study of in vivo microenvironments. The type of simple bioreactor system described here can be used to model tissues such as the myocardium, which experiences interstitial fluid flow from perfusion through the extracellular matrix as well as cyclic strain from the systole-diastole cycle of the heart. It is not trivial to apply both cross flow and cyclic strain to cell-seeded hydrogels because of gel attachment. Moreover, the myofibroblast transition is characterized by increased contractility, which makes gel attachment even more difficult because of augmented gel compaction. Nonetheless, the apparatus was able to successfully apply both mechanical stimuli to the gels. Unfortunately, the apparatus could not control oxygen concentration, since it did not

fit within an incubator. Future work may involve decreasing the size of the system so that mechanical stimuli can be combined with hypoxia to further imitate the microenvironment of the in vivo fibrotic scar.

5.3 Mechanisms of fibroblast response to exogenous stimuli

There is increasing evidence that mechanical stimulation is a key regulator of the fibroblast to myofibroblast transition in the myocardium. Our experimental and computational data suggest that cardiac fibroblasts distinguish between fluid-induced and strain-induced mechanical stresses, though there is crosstalk between the mechanotransduction mechanisms. The cellular response to both types of mechanical stress involves the TGF-β and AT1R signaling pathways, and the possible interaction between these pathways is shown schematically in Figure 5.2.

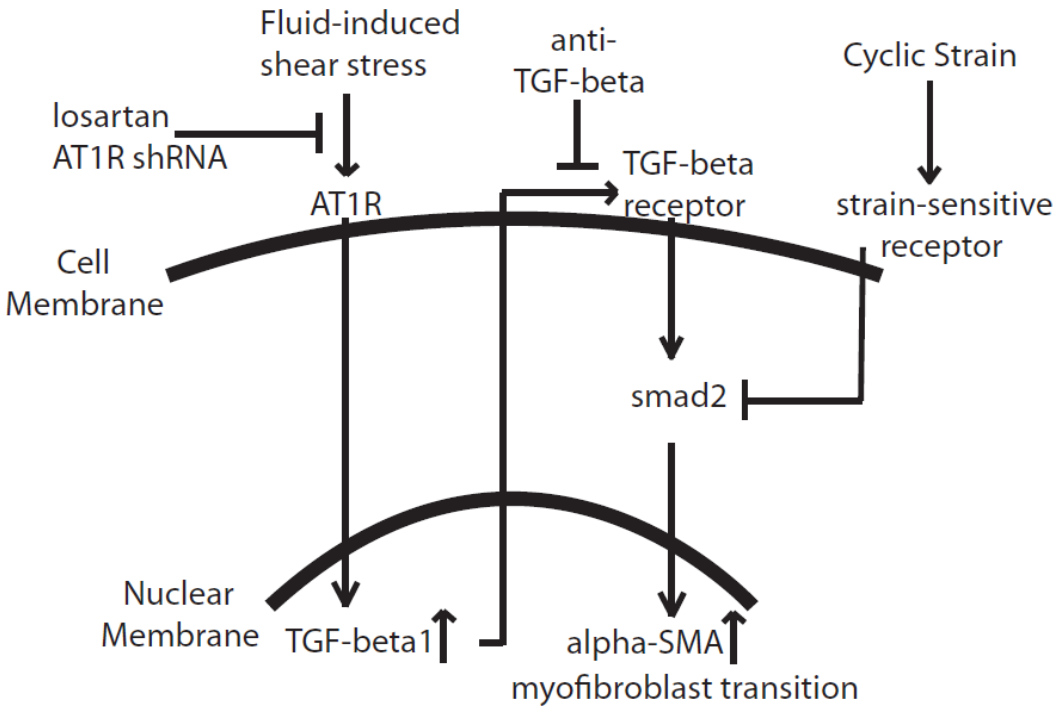

Figure 5.2 - **Schematic of experimental results:** Summary of the crosstalk between AT1R activation and TGF-β signaling in cardiac fibroblasts undergoing fluid- and strain-induced mechanical stimulation.

Direct activation of AT1R by fluid-induced shear stimulates the production of TGF-β1, which in turn acts in an autocrine and paracrine manner to create a positive feedback loop promoting the myofibroblast phenotype. Blocking of AT1R using losartan or shRNA negates this effect. At the same time, cyclic strain attenuates the phosphorylation of smad2, a downstream effector of TGF-β signaling, and therefore prevents the myofibroblast transition. These mechanisms indicate that increased interstitial perfusion would initiate the fibrotic response, while also suggesting a protective effect of cyclic strain in preventing cardiac fibrosis. This finding may have a direct impact on both the understanding and treatment of fibrosis in the myocardium, since our study suggests AT1R is a potential target to block the mechanical stress-induced transition to the myofibroblast phenotype. These results also provide insight into recent clinical findings that AT1R inhibitors used to treat hypertension can also improve the function of fibrotic hearts, and reduce the occurrence of heart failure [Konstam, 2009].

Changes in α-SMA message levels provided the clearest demonstration of the divergent signal transduction of cross flow and cyclic strain. Cross flow alone caused a nearly nine-fold increase in message, while cyclic strain caused a decrease to the initial control level. However, the combination of cyclic strain and cross flow resulted in α-SMA message levels not significantly different from the 48 h control, suggesting that the two modes of mechanical stimulation act through connected signaling pathways. Inhibition experiments indicated that inactivation of AT1R attenuated the cross flow-induced effect, but only blocking TGF-β negated both the flow-induced α-SMA message increase and the baseline rise between the initial and 48 h controls. A summary of the different stimuli on message levels is provided in Figure 5.3.

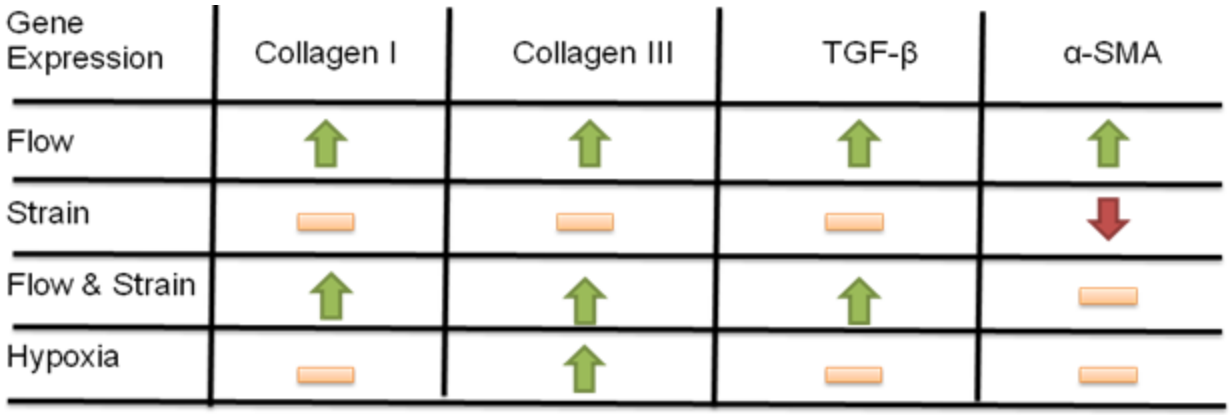

Figure 5.3 - **Summary of fibroblast response to mechanical and hypoxic stress:** Message levels of four markers for the myofibroblast transition, col1a1, col3a1, TGF-β, and α-SMA were compared to 48 hr control levels.

This result not only identifies AT1R as a transduction receptor for cross flow, but also suggests that TGF-β1 is a master regulator of the mechanical stress-induced myofibroblast transition. Further evidence for the role of TGF-β1 as a regulator of mechanotransduction was provided by experiments in which fibroblasts were exposed to hypoxic conditions. The low oxygen environment stimulated the myofibroblast transition, as evidenced by increased collagen type III message levels, but did so without the increase in TGF-β1 expression observed in cells exposed to cross flow. Finally, immunoblotting for phosphorylated smad2 indicated that cyclic strain affected TGF-β signaling, providing the link between the transduction of flow and strain.

Analytical studies of the mechanics of hydrogels tested in our flow-strain bioreactor have shown that the deformation of the hydrogel and interstitial fluid flow are also strongly coupled in this system, as they are in vivo [Ashikaga, 2008]. Due to the high porosity of the 3D protein hydrogel, cyclic strain can cause substantial interstitial fluid flow within the matrix, even in the absence of cross flow. In contrast, cross flow itself induces negligible strain-induced stress within the hydrogel. In the present study only the cross flow condition caused a marked increase

in α-SMA, although the model predicted a considerable amount of interstitial flow for the all three mechanical stimulation conditions examined (flow, strain, and combined flow/strain). Therefore, application of mechanical strain clearly attenuated the rise in α-SMA, even though it also induced interstitial flow. There is also a possibility that the response of the fibroblasts has some temporal dependence, since strain is applied cyclically and interstitial fluid flow at a constant flow rate. However, Figure 4.26 indicates that pulsatile flow also stimulates the myofibroblast transition. Taken together, these results suggest that interstitial fluid flow is a potent initiator of signaling through AT1R, but that cyclic deformation of the extracellular matrix is able to override or diminish these effects. Further explanation of the results of the analytical model is provided in the following section.

The findings of the present study serve to illuminate the fibrotic response in cardiac tissue. Since a fibrotic scar is characterized by excessive extracellular matrix deposition, it is stiffer than surrounding myocardium. And because a cardiac scar is also characterized by an absence of healthy, contracting cardiomyocytes, there is considerably less strain in the scar than in surrounding regions. However, the scar region is still perfused by capillary networks [Boudoulas, 2009]. Our study provides evidence that this combination of mechanical factors may play a role in causing the transition of healthy fibroblasts to the myofibroblast phenotype, thereby propagating the fibrotic response. Our findings also provide a potential mechanism for the effects of losartan in treating fibrotic hearts, since blocking of flow-mediated phenotype shifts in cardiac fibroblasts may be of particular benefit. The *in vitro* model we used is necessarily a simplified version of the complex cellular milieu of the myocardium. However it is a promising system for isolating the effects of mechanical stresses in 3D systems, and therefore

is of potential importance to clinical trials focusing on the anti-fibrotic potential of losartan and its conjugates [NCT ID: NCT01150461].

5.4 The collagen gel as a poroelastic medium

Predicting the pressures, relative velocities, and solid deformation within mechanically stimulated hydrogels is important when analyzing the response of embedded cells. This holds true not only for the particular experimental configuration used in the present study, but also more broadly for any system that applies solid or fluid stress to three-dimensional cell-seeded scaffolds. Cells are exposed to solid stress from the deformation of the matrix as well as shear stress from the flow of fluid within the gel. Models such as the one we have developed can therefore provide insight into the specific mechanical factors that affect cell function. In the present study we applied cyclic strain, cross flow, or a combination of both. The results indicated that although cyclic strain can induce fluid flow, imposing a cross-flow causes negligible strain in a poroelastic medium. In fact, the fluid velocity induced by 1 Hz cyclic strain was about 10 times higher than for a static gel exposed to cross flow for the same pressure difference across the gel. Because the model assumes no flow-induced deformation in the medium, the results suggest that although strain induces fluid flow, fluid flow does not induce strain.

The results of the experimental portion of the study indicate that fibroblasts respond differently to all three loading scenarios. Combining cross-flow and cyclic strain did not affect the solid deformation within the gels, but did affect the relative velocity in the y direction. Without cross flow, the relative fluid flow at the centerline of the gel in the x direction was zero, indicating no net fluid flow across the gel. Using a common analogy between fluid flow and electric current, cyclic strain can be considered to induce an AC current while cross flow causes a DC offset to that current. Therefore, even though the effects of strain and cross-flow are very

much intertwined, the three loading scenarios of cyclic strain, cross-flow, and a combination of both create three different stress states within the gels. This supports the experimental results, which indicated a unique response between cells exposed to the different loading conditions.

It is unlikely that diffusion of nutrients is a factor, since the high porosity of the hydrogel (>99%) does not create a substantial barrier to diffusion. Nonetheless, the Peclet number of the hydrogel is still high, meaning that convection does influence the transport of solutes in the cycled gel. Because fluid velocity is highest at the ends of the gel, it is possible that cells in the middle of hydrogels being cyclically strained are not receiving the same concentrations of nutrients as cells near the ends. This effect provides another example of the heterogeneity within the stimulated hydrogel. As the results indicated, the stress exerted on the embedded cells exhibits both a spatial and temporal dependence. However, this heterogeneity is not captured by the quantitative reverse transcription PCR, which involves homogenization of the entire gel. However, it would be quite difficult to create a homogenous stress state in a 3D material, and the results of the poroelastic model suggest that all three stimuli produce generally distinct stresses within the hydrogel.

5.5 The effect of MSC on the fibroblast transition

The present study describes a 3D coculture model of MSC injected into a myocardial fibrotic scar. The model allows for testing the response of the MSC to specific biochemical and mechanical stimuli, in addition to observing the effect of MSC implantation on cardiac fibroblast phenotype. The results indicate that the presence of MSC significantly impedes the myofibroblast transition, no matter what stimuli the gels are exposed to. Message levels of collagens I and III, TGFβ, and αSMA were all held at or below initial levels, a result supported by immunofluorescence of the fibroblasts isolated from the MSC injection cone. The behavior of

the injected stem cells was modulated by the different stimuli: hypoxia resulted in higher migration distances, but mechanical stimulation resulted in decreased cd90 expression. Finally, the levels of VEGF and IGF-1 within the gels were measured using ELISA. Neither factor was affected by mechanical stress, but hypoxia had a substantial affect on VEGF production by the implanted stem cells. Gels seeded only with fibroblasts also produced significant VEGF and IGF-1 levels, indicating that fibroblasts themselves contribute to the paracrine environment in the ischemic myocardium.

The results of the study do not reveal much about the fate of the stem cells after injection into the collagen gel. It is notable that the expression of the stemness marker, cd90, is attenuated by both cyclic strain and interstitial fluid flow. The result is nonintuitive because the two mechanical stimuli had such different effects on the myofibroblast transition. The loss of the stem marker, in addition to reduced migration compared to MSC stimulated by hypoxia, suggests that mechanical stress and hypoxia lead to differentiation and proliferation, respectively. The study does not reveal what lineage the cells are differentiating to, nor is it clear what lineage would be optimal for benefiting the myocardium. The MSC can become pro- or anti-inflammatory, which would substantially affect the set of paracrine factors released by the cells and their effect on the surrounding cardiomyocytes and vascular cells. Further work elucidating the fate of MSC in engineered cardiac tissue, as well as the mechanisms of action on heart failure will be important to advancing the field of cell-based therapies for cardiac pathology

Nonetheless, the coculture model presented in this study provides a new way to study the interaction of implanted stem cells with the fibrotic environment. Injected stem cells are surrounded in three dimensions by cardiac fibroblasts, which allows for crosstalk between the two cell types. However, although the hydrogel model adds complexity to existing 2D coculture

models, it does not come close to mimicking the complete microenvironment of an in vivo scar. The microenvironment of a scar not only includes fibroblasts, but also smooth muscle and endothelial cells from the vasculature, and possibly even immune cells depending on when the cells are injected into the injury site. These cells can certainly modulate stem cell function and response, and this effect is not captured by the present model. Nonetheless, it is possible to envision incorporating these cells into a collagen hydrogel, similar to the fibroblast-populated gels presented in this study.

As mentioned in the introduction, one current problem with MSC treatment of heart disease is the inherent variability in stem cell function. Therefore, it is possible that this hydrogel model can be used as a screening system to identify the populations of cells that are more likely to produce a beneficial effect. The question remains what element of MSC cell response is actually beneficial in vivo. It is unclear whether increased migration is a good thing to have in the heart, especially when alterations in the complex microstructure can lead to arrhythmias. The immunofluorescence images indicated that mechanical stimulation reduced expression of cd90, a marker of stemness, but it is unclear how differentiation would affect MSC-mediated repair. The present study does not provide insight into these questions because all the mechanical and biochemical stimuli caused downregulation of markers for the myofibroblast transition in adjacent fibroblasts, regardless of migration distance, cd90 expression, and paracrine release of VEGF and IGF-1. The results of this study verify that stem cell paracrine action is a time-dependent process, since release of VEGF and IGF-1 changed substantially with time. Quantification of migration distance also revealed that cell velocity was significantly different between testing conditions. This complicates the design of a “growth factor cocktail” to replace the need for cell transplantation. It is unknown whether there was any spatial variation in the

paracrine release, since gels were processed in bulk. For example, it would be interesting to partition the gel with higher resolution in order to compare the activation of the fibroblasts closer to the injection cone with cells further away. Interestingly, neither VEGF nor IGF-1 was released more in response to mechanical stress. Even though the list of possible paracrine factors from MSC is very long, future work may include measuring the release of other factors beyond VEGF and IGF-1.

6. Conclusions, Impact, and Recommendations

This dissertation centered on five specific aims, and the results produced five primary conclusions from those aims:

- Cardiac fibroblasts seeded in a collagen hydrogel undergo a baseline myofibroblast transition under static culture conditions, which is augmented by reduced serum and matrix compliance.

- Cross flow and cyclic strain can be applied simultaneously to cell-seeded collagen hydrogels in an open PDMS chamber, using an acellular gel layer to evenly distribute cross flow.
- Interstitial fluid flow stimulates the myofibroblast transition through an AT1R/TGFβ mediated response, but cyclic strain attenuates this transition through a related pathway.

- Cyclically deforming a porous collagen hydrogel produces substantial fluid flow within the gel.

- Coculturing MSC with cardiac fibroblasts in a collagen hydrogel, regardless of mechanical and biochemical stimulation, results in reduced transition to the myofibroblast phenotype.

These conclusions have several implications for how mechanics influences the pathogenesis of fibrosis in the myocardium. The preliminary collagen gel model provided in vitro evidence of a positive feedback loop in the myofibroblast transition; low serum caused fibroblasts to transition to myofibroblasts, which caused an increase in contractility and subsequent matrix compaction. The resulting increase in stiffness then further stimulated the

myofibroblast transition. This process may explain what happens in vivo, because fibroblasts are starved for nutrients during the ischemic phase after a myocardial infarction, and begin to transition to a myofibroblast phenotype that secretes thick extracellular matrix. However, identifying the presence of this feedback loop does not necessarily lead to treatments to prevent it. Currently, there is no means available to simply reduce the stiffness of fibrotic scars, nor would that necessarily be a beneficial option. In many cases, especially in systolic heart failure, the body forms the stiff scar tissue to maintain the integrity of the myocardium, preventing rupture of the ventricle. Reducing the stiffness of fibrotic tissue may alleviate the positive feedback cycle leading to the myofibroblast phenotype, but it could have disastrous effects on the patient.

Mechanical stimulation, both interstitial fluid flow and cyclic strain, were applied to represent the stress exerted on cells in vivo. Cyclic strain was used to mimic the beating of the heart during systole and diastole, while interstitial fluid flow was employed to account for the perfusion of capillaries within the tissue. However, the magnitude and frequency of these stimuli did not match the in vivo rat heart. For instance, the neonatal rat heart rate is about 300 bpm, and there have been no estimates of the interstitial flow rates in the rat heart. Nonetheless, the study provides an indication of how the fibroblasts respond to two different modes of mechanical stress (shear from fluid flow versus structural strain from the deformation of the matrix). The results indicate that the fibroblasts respond differently to these two modes, which has implications for how the fibroblasts behave in a scar environment. As mentioned, the scar is characterized by increased stiffness, reduced cyclic strain, but the persistence of perfusion from microvasculature. The ability of fibroblasts to distinguish between two different modes of mechanical stimulation may help explain why the microenvironment of the scar instigates the myofibroblast transition.

The present work also identifies key pathways that are involved in the myofibroblast transition, and can be used to influence the development of treatments that prevent scar growth. For example, AT1R inhibitors have been used for many years to block the renin-angiotensin system to treat hypertension. By identifying the role of this receptor in the myofibroblast transition, the results lend credence to the use of losartan as an anti-fibrotic agent. Moreover, by identifying how cyclic strain and interstitial fluid flow differentially affect fibroblast phenotype, the present study produces questions about how LVADs affect myocardial fibrosis. For example, by unloading the left ventricle, the solid and fluid mechanics are substantially altered, perhaps in a manner that facilitates or attenuates scar growth. The results can also be applied to in vivo scar conditions, which are characterized by decreased cyclic strain due to death of the cardiomyocytes as well as the presence of interstitial fluid flow from the scar microvasculature.

There are still several questions that have not been answered by this work. The following bullet points detail areas of future work:

- What MSC paracrine factor is being affected by mechanical stress? And what is the fate of other stem markers after mechanical stimulation? What lineage are the MSC committing to?
- Determine how cyclic strain is being transduced by the cell. What receptor(s) are activated by cyclic strain in a three-dimensional environment?
- Use the collagen hydrogel/myofibroblast model to study cell delivery methods.
- Can the hydrogel/myofibroblast model be used as a testing platform for evaluating the potential of patients' stem cells to attenuate fibrotic scar growth?
- Adapt the current testing platform to include simultaneous hypoxia and mechanical stimulation that is more comparable to in vivo levels.

This dissertation demonstrates in vitro that the presence of MSC in the collagen hydrogel significantly reduces the myofibroblast transition. However, the results do not identify a

mechanism for this beneficial effect. Future work may involve performing more ELISAs to determine the paracrine factor induced by mechanical stress. Other assays can be used to determine if the MSC are differentiating, beyond observing cd90 expression. Moreover, studies can be performed to determine what lineage the cells are differentiating into. Another ambiguity is the identity of the receptor through which cyclic strain is transduced in the 3D collagen hydrogel. Because the receptor would be sensing structural deformation, it is plausible that integrins may be responsible for the mechanism. Nonetheless, the cyclic stretch could be affecting ion channels and other cell surface receptors not involved in cell adhesion. Future assays could use shRNA to block certain receptors, similar to the method used in this study to block AT1R, to identify the responsible receptor.

Finally, the collagen hydrogel model has potential to be used as a testing platform to further study cell delivery methods as well as to assess the ability of a patient's MSC to produce a beneficial effect in the heart. One of the major issues with cell therapy is the successful engraftment of the cells to the tissue. The collagen hydrogel model presented in this study can be used to test these delivery methods, which may include encapsulating the cells in a protein matrix prior to injection. The model presents a platform to study the effects of mechanical and biochemical stimuli on cell attachment and viability during delivery. Moreover, because the collagen gel mimics certain aspects of the in vivo myocardium, it can be used to assess how a patient's MSC might behave once injected. For this reason, combining hypoxia with more relevant mechanical stimulation may more faithfully represent the in vivo microenvironment. For example, prior to delivery, MSC can be isolated from a patient and injected into the hydrogel as described previously. The behavior of the cells could be observed in the in vitro environment, to

predict their response in vivo. Future work will involve identifying metrics to differentiate MSC that will be beneficial from those that will not produce an improvement.

It is clear that the fields of biomechanics and regenerative medicine have yet to fully bridge the gap between traditional engineering approaches and rigorous cell and molecular biology. For example, many of the tissue engineering approaches currently rely on "letting the body do the work". Understanding how cells behave in the in vivo microenvironment will not only aid tissue engineering approaches, but will also assist in the comprehension of pathology. For these reasons, comprehending the mechanism of cell response to stimuli like mechanical stress is crucial. This advance will involve both improvements in understanding cell biomechanics, as well as development in applying new molecular and biological approaches to discerning cell response. As the work in this dissertation implies, further work is required to better characterize the in vivo mechanical environment before these advancements can be made. Nonetheless, the present work is an example of how understanding cell mechanics in vitro has significance to characterizing cell behavior in vivo.

Chapter VI

Appended Works

6.1 Selected Protocols

6.1.1 Mechanical Testing of Released Collagen Gels

Materials needed

Delrin compression platens
Stainless steel spatula
Thumb drive
Ruler
Digital camera

Setup

1. Turn on the controller (large black box) and the computer 5-10 minutes prior to turning on the power supply (gray box).
2. Open the application "Start 1st 800", and wait until window opens.
3. Open the application "V2".
4. Click File > Open, and choose any file.
5. Click "Switch On" to engage the power supply.
6. Click the "DAQ" button and set the destination file, sampling rate, and starting specification (manual, automatic, time delayed, etc.)
7. Click Settings > Offset Readout
8. Move LVDT or encoder at 5 mm intervals to position the platen before testing (< is compression, and > is tension).
9. Click Test and choose either dynamic or static.
10. For manual DAQ, click "start recording" prior to clicking "start test".
11. Once the test is completed, click "stop recording".
12. Either repeat the testing, or shut down the machine by closing the V2 and start 1st applications.

Testing tips

1. Decrease the platen height by 0.5 mm until a substantial change in load is observed, to ascertain contact with the sample. Once contact is made, then offset the readout of the encoder.
2. Take a picture of the sample after contact has been made, with a ruler in the frame, to measure the starting height of the gel (and to estimate levels of strain).
3. Prior to testing, compress the sample at 10% strain/s to about 5-10% strain before returning platen to original height, in order to precondition the gel.

4. Never strain the sample more than 15-20% strain, to keep within the limits of infinitesimal strain assumption.

Analysis

1. Convert the "encoder" column to a "strain" column using the change in height divided by the original height.
2. Convert the "load" column to a "stress" column by calculating the cross-sectional area of the sample (from the digital image used to determine height), and changing grams force to Newtons (multiply by 0.00981).
3. Plot the stress versus strain and take the slope in a linear region near 10% strain.

6.1.2. Quantitative reverse transcription PCR

Materials needed

TRIzol reagent
1.5 mL microcentrifuge tubes
Chloroform
Isopropanol
75% ethanol
DNAse free water
Temperature-controlled microcentrifuge
Hotplate
Nanodrop, or some method to quantify nucleic acid

RNA isolation

1. Add 0.2 µL of TRIzol to a 1 mL gel in a 1.5 mL microcentrifuge tube
2. Manually homogenize the gel until collagen gel fragments transition from white to reddish in color
3. Pipette the solution up and down 5 times until fragments are nearly invisible.
4. Add 0.8 µL of TRIzol to the solution, and let incubate at room temperature for 5 minutes.
5. Either place in -80 C freezer or use in the next step.
6. Add 0.2 µL of chloroform, and shake vigorously by hand for 15 seconds.
7. Incubate at room temperature for 2.5 to 3 minutes.
8. Centrifuge at 12 g at 4 C for 15 minutes.
9. Remove the clear portion in the top layer, and add to 0.5 µL of isopropanol.
10. Incubate for 10 minutes at room temperature, then centrifuge at 12 g, 4 C for 10 minutes.
11. Remove the supernatant, and replace with 1 mL of the 75% ethanol solution.
12. Vortex for 15 seconds. There should be a white RNA pellet visible during vortexing.
13. Centrifuge at 7.5 g at 4 C for 5 minutes.
14. Remove supernatant, and let incubate with the cap open for 7.5-10 minutes.
15. Add 26 µL of RNAse free water, and incubate at 55 C for 10 minutes.
16. Quantify the RNA using the nanodrop.
17. (optional) dilute samples to create a uniform RNA quantity prior to qRT-PCR.

Reverse Transcription and PCR

1. Follow the instructions on the reverse transcription (RT) kit to create the correct mixture.
2. Add 25 μL of the RNA solution to 25 μL of the RT cocktail.
3. Run the "cDNA" program in Limin's file directory in the thermal cycler (~2.5 hrs in length).
4. Create dilutions of the selected primers, and dilutions of the cDNA mixtures according to the Excel worksheet entitled "Taqman RTPCR" in the protocols folder.
5. Run the Applied Biosystems PCR program, following the instruction manual for setup and operation. It is important to change the second temperature step from 20 seconds to 2 minutes.

6.1.3. Immunofluorescence

Materials needed

Triton X-100
3.7% paraformaldehyde
Normal goat serum
Primary antibodies
Secondary antibodies
PBS

Fixing

1. Wash sample 3x in PBS
2. Add 1 mL of paraformaldehyde for each 1 mL of collagen gel
3. Incubate on the shaker for 10-20 minutes
4. Repeat step 1
5. Either store the sample at 37 C and 5% CO_2, or begin the blocking step immediately

Blocking/Permeabilizing

1. Add 1 mL of PBS containing 0.1% X-100 and 5% NGS for each 1 mL of collagen gel
2. Incubate at 37 C and 5% CO_2 for 30 minutes.
3. Wash sample 3x in PBS

Primary/secondary staining

1. Make a PBS cocktail containing 0.1% X-100 and 2% NGS in addition to primary antibodies in the correct dilutions.
2. Incubate at 37 C and 5% CO_2 for 45 minutes, or at 4 C for up to two days.
3. Wash sample 3x in PBS, in consecutive 10 minute steps.

4. If using monoclonal antibodies derived from the same species, incubate sample with F_{ab} fragments at 37 C and 5% CO_2 for 30-45 minutes, followed by 3x washes in PBS.
5. Incubate with correct secondary antibodies at 37 C and 5% CO_2 for 30-45 minutes.
6. Wash 3x in PBS and visualize with the confocal microscope.

6.1.4 Western blotting

Materials needed (Westfall lab, except antibodies)

Pyrex dishes
Saran wrap
Transfer apparatus
Running apparatus
TBS
Methanol
Ethanol
Trizma base
Glycine
TBS-T
Dry milk
Polyacrylimide gel
PVDF transfer membrane
Primary/secondary antibodies

Sample preparation

1. Homogenize the gel in Garner buffer, with phosphatase inhibitors added for phosphorylation studies, into gel fragments
2. Vortex samples, and continue manual homogenization with a pestle.
3. Spin down the samples at 2 g for 20 seconds, in order to separate the large collagen fragments from the lighter cellular protein.
4. Centrifuge the supernatant at 12 g for 15 minutes, and then dissolve in sample buffer.
5. Boil the samples for 3 minutes, and then sonicate them for 10 minutes.

Running the gel

1. Create a polyacrylimide gel of desired PA percentage, or purchase a BioRad gel.
2. Wash the gel lanes with DI water, and aspirate after soaking at room temperature for 5 minutes.
3. Fill the lanes with samples, dissolved in sample buffer.
4. Run the gel at 200 V and 25 mA for 2-3 hours, depending on the molecular weight of the protein.

Transfer the gel

1. Remove the gel from the running apparatus (and its cassette if using a BioRad gel).
2. Soak the gel in transfer buffer for 15 minutes.
3. Cut a piece of transfer membrane that fits the gel, and soak in methanol for 15 seconds.
4. Remove the membrane from the methanol, and wash in ddH_2O for 10 minutes.
5. Soak the membrane in transfer buffer for an additional 10 minutes.
6. Create a sandwich of the gel, the transfer membrane, and chromatography paper (in that order), and place in the transfer apparatus.
7. Run the transfer apparatus at 50 V and 500 mA overnight.

Staining the membrane

1. To normalize protein loading, the blot can be stained for GAPDH or another housekeeping protein, or the gel can be silver stained (see silver staining protocol).
2. Wash blot 3x in TBS.
3. Block the blot in TBS containing 5% dry milk in TBS-T for 45 minutes.
4. Wash blot 3x in TBS-T.
5. Incubate in TBS-T, 5% dry milk mixture containing primary antibodies in the correct dilutions at room temperature for an hour or at 4 C overnight.
6. Wash blot 3x in TBS-T.
7. Incubate in TBS-T, 5% dry milk mixture containing secondary antibodies for an hour at room temperature.
8. Wash blot 2x in TBS-T
9. Wash blot once in TBS

Visualizing the blot using chemiluminescence

1. Place the blot in Pierce substrate for 15 seconds.
2. Use undeveloped film to visualize the gel

6.1.5 Lentiviral delivery

Materials needed

Lentiviral particles
Polybrene
Puromycin
Culture media
Tissue culture plates
PBS

Preparation

1. First, determine the lowest concentration of puromycin able to kill 99% of the cells on the tissue culture plastic. For neonatal cardiac fibroblasts and rat-derived MSC, this is about 2.5 mg/mL.
2. Second, determine the highest concentration of polybrene that does not affect cell viability.
3. Find an estimate of cell proliferation after plating. For example, count the cells 12, 24, 48 hours after plating to get an idea of how many cells there will be a day or two after plating.
4. From this number, calculate the number of particles needed for the desired MOI. It is recommended that the infection be made at 60-70% confluency.

Infection

1. At time of infection, remove media and wash 3x with PBS.
2. Replace with media containing polybrene in the predetermined concentration.
3. Use a pipette to add the lentiviral particles dropwise in different locations of the tissue culture plate.
4. Incubate the cells and the lentiviral particles for 12-16 hours at 37 C and 5% CO_2.
5. After incubation, aspirate particle-containing media and wash 3x in PBS.

Cell Isolation

1. To isolate infected cells, add culture media containing puromycin
2. After 48 hours, wash the plate thoroughly and replace with non-puromycin media
3. Monitor the cells for a day or two to assure normal cell growth
4. Split the cells and freeze to store or use them immediately.

6.1.6 Operation of flow/strain wells

Materials needed

Acrylic chamber
Inlet tubing and luer inlets
PDMS wells
HEPES buffer
Culture medium
Nylon grips
Stainless steel fittings
Forceps

Preparation

1. Autoclave all pieces of the apparatus, including tubing, luers, and gripping apparatus.
2. Prepare HEPES containing media by adding 15 mM HEPES.

3. Sterilize the acrylic chamber by filling it with 50% bleach, sealing it, and incubating it at room temperature overnight. Prior to use, wash in ddH_2O 10-15 times.

Setup

1. Attach the lower fitting to the acrylic bath, and fill about ¼ way with HEPES-containing media.
2. Fit the PDMS well into the grip, using the bottom fitting to attach the grip to the bath.
3. Fill the media past the PDMS wells, to assure the samples don't dry out, and to submerge the inlet dowels for flow experiments.
4. Remove the dowels, and use forceps to insert the inlet tube into the PDMS well inlets.
5. For flow-only experiments, cover the top of the acrylic chamber with parafilm, with a 0.22 μm hole fixed on top of punctured holes to allow sufficient respiration.
6. For strain experiments, affix the top grip to the PDMS chamber and use parafilm to create a pseudo cap on the acrylic chamber.

Operation

1. Place the assembly into the large water bath underneath the mechanical testing platen.
2. Attach the stainless fittings to the top platen and the bottom surface of the bath.
3. Refer to the mechanical testing protocol to set cyclic strain parameters.
4. For flow, attach the inlet tubes to a syringe, placed in a syringe pump with a specified volume flow rate.

6.1.7 Stem cell injection into collagen hydrogels

Materials needed

Micro-manipulator (Mayer lab)
25 gauge needle, 1 ½ " in length

1. Set the position of the micro-manipulator to determine the angle of injection (this can be done using a protractor or ruler with a digital camera and ImageJ.
2. Determine the penetration distance, using the knobs to specify the exact distance.
3. Dilute the stem cells in a high concentration, to minimize the amount of fluid needed for injection.
4. When injecting, move the manipulator quickly using the joystick. At slower penetration speed, the gel is not punctured correctly, and the cells do not enter the collagen gel.
5. To assure successful injection, the stereoscope can be used to indicate the injection cone and the presence of any cells within the gel.
6. Incubate for an hour at 37 C and 5% CO_2 for two hours to allow for cell attachment.
7. Add culture media to the gels after 2 hours.

6.2 Adult cardiomyocyte response to substrates of varying stiffness

Introduction:

Substrates with tunable stiffness provide crucial information about how cells sense and respond to the mechanics of their environment. This tool has been used with substantial success for controlling stem cell fate [1], discerning the contractility of smooth muscle cells and other mesenchymal cell types [2,3], and observing the response of neonatal cardiomyocytes to the stiffness environment of the developing heart [4,5,6]. However, few studies have observed the effect of substrate stiffness on adult cardiomyocytes. In vivo, the cells secrete a basement membrane containing laminin and collagen IV that allows for integration with the myocardial extracellular matrix. An exciting field of research is emerging to understand how the extracellular microenvironment, especially its mechanical aspect, affects cardiomyocyte function. The goal of such research is to identify the mechanisms by which this cell-matrix interaction malfunctions in pathology, so that treatments can be developed to impede heart failure. The present study uses tunable stiffness substrates to study the effect of extracellular compliance on sarcomere and costamere organization and cardiomyocyte contraction dynamics.

The question of how cardiomyocytes sense strain is crucial for understanding how these cells regulate their contraction/relaxation dynamics during systole and diastole, and multiple studies have identified proteins associated with a "stretch sensor" mechanism [7,8]. But it is intuitive that cardiomyocytes would also have a "stress sensor", considering the changes in myocardial stiffness that occur as a result of pathology (myocardial infarction, hypertrophic cardiomyopathies, etc.) as well as aging. Atomic force microscopy measurements of fibrotic myocardium elastic moduli have found values between 20 and 55 kPa [9,10], compared to 2 and 8 kPa for the non-fibrotic myocardium as determined by MRI [11]. Though it is often difficult to quantitatively compare elastic moduli measured by different methods [12], fibrotic tissue is characterized by increased extracellular matrix that facilitates a stiffer environment. A recent study indicated that substrate stiffness resembling a fibrotic scar inhibited beating of embryonic cardiomyocytes [13].

Proteins involved in the mechanism of sensing stretch have been identified in both the sarcomere and the costamere complex [7]. The function of the costamere is to couple the z disk to the basement membrane, so that force generated by the sarcomere can be translated to the surrounding extracellular matrix. The costamere complex encompasses membrane receptors including integrins β1 and α7 [14]. Integrin β1 is an important surface receptor in cardiomyocytes, regulating cell matrix interactions [15] and even playing a role in cytoprotection [16]. Integrins are anchored to the z-disk by structural proteins including vinculin, talin, desmin, and zyxin [8]. The z-disk complex is a complicated array of proteins that also includes candidates for the stretch sensing mechanism, with α-actinin forming the backbone of the structure. Recent studies have indicated that the z-disk is among the initial targets for deterioration during isoproterenol-induced adult cardiomyocyte apoptosis [17], suggesting that z-disk integrity is a crucial indicator of cardiomyocyte function.

In the present study, components of both costamere and sarcomere structure and function in culture are analyzed in response to substrate stiffness. Adult cardiomyocytes in culture beat spontaneously and undergo a slow dedifferentiation process, which involves changes in the cytoskeleton and t-tubule structure [18,19]. The calcium handling in these cells also changes with time, possibly due to influx through protein kinase A-activated L-type Ca^{2+} channels [20]. To determine how the stiffness of the extracellular environment affects these properties, isolated

cardiomyocytes are plated on different stiffness substrates coated with laminin and cultured for 48 hours. The organization of α-actinin and integrin β1 is observed with immunofluoresence, and message levels of proteins associated with the sarcomere and costamere are measured using quantitative reverse transcription PCR. Calyculin A, a general phosphotase inhibitor, is used to determine if the effects are related to some proteolytic activity. Finally, cells are paced at three different time points to determine how the changes in cell structure affect the function of the cardiomyocytes, as well as to identify any time-dependence in the cell response.

Methods:

Cell Isolation and Culture: Adult rat ventricular cardiomyocytes were isolated as previously described [21]. Hearts from Sprague–Dawley rats were enzymatically digested in a modified Langendorff perfusion apparatus to isolate the cardiomyocytes. The protocol was approved by The University of Michigan University Committee on Use and Care of Animals (UCUCA) in accordance with university guidelines. 2.0 x 10^4 cells were plated on PDMS coated with 40 μg/mL of laminin in M199 supplemented with 5% fetal bovine serum, 50 U/mL penicillin, and 50 μg/mL streptomycin for 2 hours. After that period, the media was replaced with M199 supplemented with 10 mM HEPES, 0.2 mg/ml bovine serum albumin, 10 mM glutathione, and the same concentrations of penicillin and streptomycin. For experiments involving calyculin A, 0.5 μg/mL of the phosphotase inhibitor was added to the media.

PDMS Substrate Fabrication and Validation: The base and curing agent of Sylgard 184 were mixed in ratios of 10:1, 20:1, 30:1, and 50:1 by weight, and 1 mL of the elastomer was cured in 6 well polystyrene plates, creating approximately 1 mm thick slabs. For experiments that required electric field stimulation, blocks of the elastomer were cut out of the 6 well plate and bonded to glass coverslips. Prior to coating with laminin, the PDMS was etched with 5 M sulfuric acid for 60-90 minutes, washed thoroughly in distilled water, and sterilized using a UV lamp for 30 minutes. To determine elastic modulus, the elastomer was molded in a rectangular mold with defined width and length. A uniaxial mechanical testing system was used to apply a 20% total strain at a rate of 10%/s. The elastic modulus was calculated by taking the slope of the stress/strain curve at approximately 10% strain, in order to keep within the limits of linear strain theory. PDMS mixed in ratios of 10:1, 20:1, 30:1, and 50:1 produced mean moduli of 255 kPa, 117 kPa, 27 kPa, and 7 kPa respectively.

Immunofluoresence: After 48 hours in culture, cells were fixed, permeabilized, and stained using previously described protocols [3]. Immunostains included fluorescent DAPI (1:50 dilution), phalloidin (1:50) conjugated to Alexa Fluor 488, and monoclonal mouse antibodies for α-actinin (1:500) and integrin β1 (1:50). A secondary Texas Red-tagged anti-mouse antibody was used to visualize these proteins. Cells were visualized using confocal microscopy. Projection image Z-stacks of approximately 10 μm were collected using a confocal microscope.

Immunoblotting: After 48 hours in culture, cells were lysed in ice cold sample buffer(24.77% glycerol, 1.63% SDS, 0.1 M Trizma stacking buffer, 3.31% Bromophenol Blue stock solution, 24.88 mM DTT, 1.78 mM leupeptin), and then stored at -20C. In preparation for protein separation, samples were boiled for 3 min, sonicated for 10 min. Protein separation was performed as previously described [21] using 12% or 4-12% gradient SDS-polyacrylimide 12

well gels (Bio-Rad), and then transferred onto a PVDF membrane overnight. The PVDF membrane was then blocked in either 5% dry nonfat milk or BSA, washed in Tris buffered saline (TBS), and incubated overnight at 4^{o}C with either a mouse monoclonal antibody against α-actinin (1:5000) The next day, blots were rinsed with TBS and incubated for 45 minutes at room temperature with HRP-linked anti-mouse secondary antibodies (1:2000). Gels were silver stained and a representative protein band was used to normalize for protein loading on the blot. Immunodetection was visualized with chemiluminescence using Pierce ECL Western Blotting substrate (Thermo-Fisher).

qRT-PCR: A guanidium thiocyanate-phenol-chloroform extraction protocol (TRIzol) was used to isolate mRNA from the cells after 48 hours in culture. Briefly, cells were dissolved in TRIzol, buffer, and reverse transcription of mRNA was performed with a high-capacity cDNA Archive Kit and a C-1000 Thermocycler. The quantitative PCR protocol is described in a previous publication [3].

Cell Shortening Assay: At 2, 24, and 48 hours, PDMS coverslips were transferred to a stimulation chamber mounted on a Nikon microscope stage. A video-based detection system (Ionoptix) was used to determine sarcomere shortening in response to 40V, 0.2 Hz electrical shortening.

Calcium Transient Assay: At 2, 24, and 48 hours, cells on PDMS coverslips were loaded with 5 μM Fura-2 AM for 4.5 minutes at 37C followed by a 4 minute wash in media without Fura-2 AM for de-esterification. Coverslips were again transferred to a stimulation chamber and paced using 40V amplitude at 0.2 Hz frequency. Calcium transients were measured by taking the ratio of emission at 510 nm from excitations at 360 nm and 380 nm.

Statistical Analysis: Data was expressed as mean+SE. For comparisons of immunoblotting and message levels, an unpaired Student's t test was used to determine statistical significance for comparisons between two groups, with $p<0.05$ considered significantly different. For grouped comparisons of the contractility and calcium transients, a two-way analysis of variance (ANOVA) followed by Bonferroni's multiple comparison test ($P<.05$) was used to compare multiple groups using GraphPad Prism 5 software.

Results:

Effect of substrate stiffness on α-actinin and integrin β1 organization

To assess the structural changes in response to substrate stiffness, α-actinin and integrin β1 were visualized using immunofluorescence. As Figure 1 indicates, the organization of α-actinin into uniform, periodic z-disks is substantially affected by substrate stiffness. Despite the changes to z-disk integrity, the morphology of all the cells appears to be uniform, with predominantly binucleated, rod-shaped cells on the substrates. At 255 kPa and 7 kPa (Fig. 1A, 1D), the α-actinin staining produces a clearly defined sarcomeric pattern that is not clearly apparent for cells seeded on substrate stiffnesses of 117 kPa (Fig. 1B) and completely absent for cells on 27 kPa substrates (Fig. 1C). Nonetheless, at these intermediate stiffnesses, the antibody does produce positive staining. This indicates that α-actinin, or at least an immunoreactive

degradation product, is still present in the cytoplasm. Immunoblotting was used to quantify the amount of α-actinin present within the cells, and to determine if any immunoreactive degradation products were being produced by the cells seeded on substrates with stiffness values of 117 and 27 kPa. As Figure 2 indicates, the blot does not indicate the presence of any degradation products. Rather, the amount of α-actinin within cells appears to be constant for all the substrate stiffness values tested, even though Figure 1 indicates a substantial affect on α-actinin immunofluoresence. This result suggests that the effect of substrate stiffness on α-actinin organization is not due to decreased levels of the protein.

To determine the effect of substrate stiffness on the costamere complex, integrin β1 was visualized using immunofluoresence. In cells seeded on 255 kPa and 7 kPa substrates, the integrin β1 appears to colocalize with the z-disk of the sarcomere (Fig. 3A, 3D). As for the results of the α-actinin staining, this pattern disappears for cells on the 117 kPa and 27 kPa substrates (Fig. 3B, 3C). In cells on intermediate stiffness, the integrin β1 appears to be spread homogeneously throughout the cell, with small blotches of positive staining. It is impossible to tell if these areas of positive staining correspond to the location of z-disks. Nonetheless, in cells plated on the 255 kPa and 7 kPa substrates, the β1 staining nearly illuminates the entire z-disk. Again, the immunofluorescence images indicate that the general cell morphology is unchanged despite the cytoskeletal alterations.

Effect of substrate stiffness on message level

Having shown that substrate stiffness affects the organization of key proteins in the sarcomere and costamere complex, qRT-PCR was used to determine its effect on message levels. Messages of α-actinin and integrin β1 were measured because of the immunofluoresence and immunoblotting results. Additionally, the messages of integrin α7 and vinculin, two other costamere-related proteins were also measured. For cells plated on 117 kPa substrates, messages for integrin α7 and vinculin were significantly increased compared to the levels at 255 kPa (Figure 4B, 4D). For cells on 27 kPa substrates, the messages for all four proteins measured significantly increased (Figure 4). In contrast, no messages for cells on 7 kPa substrates had any significant difference to the 255 kPa levels. Hence, although cells on intermediate stiffness show substantial disorganization of a sarcomere-related protein (α-actinin) and a costamere-related protein (integrin β1), the message levels of these and other related proteins are actually increasing. Hence, substrate stiffness affects the cells not only at a protein level, but also at a transcriptional level.

Addition of calyculin A

The general phosphotase inhibitor, calyculin A, was used to determine if the sarcomere and costamere disorganization caused by plating on intermediate stiffness involved proteolytic activity within the cells. The α-actinin immunofluorescence and immunoblotting assays were repeated for cells cultured in calyculin A-containing media. As Figure 5 indicates, cells plated on all substrates presented clear z-disk organization, and immunoblotting again showed no significant difference in α-actinin protein levels (data not shown). Interestingly, the present of calyculin did have a substantial effect on general cell morphology. This effect is especially apparent in cells on 255 kPa substrates, which display actin fibers of varying orientation and a loss of the usual rod-shaped morphology (Figure 5a). Cells plated on the other substrates also showed varying levels of actin uniformity and rod-shaped morphology. Hence, the presence of

calyculin A is affecting various cell processes in addition to blocking the degradation of the sarcomere and costamere structure at intermediate stiffness substrates.

Cell contractility assays

Cardiomyocytes were paced at different times in culture to understand how the described changes in sarcomere and costamere organization affected cross bridge cycling at different time points in culture. Moreover, these tests were used to demonstrate that varying substrate stiffness was not solely determining cell stretch and consequently the preload on the cardiomyocytes. For instance, if cardiomyocytes exerted the same level of force regardless of substrate stiffness, the cells on softer substrates would always have higher levels of strain and the observed changes could be caused solely by levels of stretch. Rather, the results of the contraction assay indicate that after 2 hours, all the cells contract roughly the same amount (Figure 6). At 24 hours, cells on the intermediate stiffness (24 kPa) actually contract the most, even higher than cells plated on the 7 kPa substrates. These results indicate that the varying substrate stiffness is affecting the stress generated within the cardiomyocytes, not just the levels of strain. These transient results also indicate that the cell response is an adaptive, time-dependent process.

For cells plated on the stiffest substrate, 255 kPa, shortening amplitude decreased significantly at the 24 hour time point, but recovered by the 48 hour time point. This recovery in amplitude was not mirrored in departure or return velocities, which were significantly less at both the 24 and 48 hour time points. Cells on the 27 kPa substrates followed a similar trend, with significantly less shortening amplitude and velocities at 48 hours. However, in contrast to cells on the stiff substrate, shortening amplitude in these cells increased significantly between the 2 and 24 hour time points. Cells on the 7 kPa substrate exhibited significant increases in shortening amplitude and velocities at 48 hours. Hence, even though cells plated on 255 kPa and 7 kPa substrates both exhibited normal α-actinin and integrin β1 organization, their shortening dynamics follow nearly opposite trends over the 48 hours in culture.

Calcium transient assays

Having shown that the shortening trends produced by substrate stiffness is an adaptive response, the calcium transients were measured to determine if the sarcomere degradation at the intermediate stiffness was caused by increases in calcium signaling. Previous studies have postulated that increased calcium transients, either by PKA activation of L-type channels or inositol trisphosphate (which facilitates calcium release from the sarcoplasmic reticulum), are associated with negative cardiomyocyte function [17]. Moreover, the calcium transient is often an indicator of force generation in the cardiomyocyte, and should be closely tied to the shortening response of the cells. However, the calcium transient of cells plated on the 27 kPa substrate significantly decreases at the 24 hour time point (Fig. 7), even though the shortening for this data point is significantly increased (Fig. 6). This result indicates that the adaptive response of cardiomyocytes is not mediated solely through calcium signaling.

In cells plated on 255 kPa substrates, the amplitude and velocity of the calcium transient does not significantly change over the 48 hour testing period. Cells plated on 7 kPa substrates also have relatively constant calcium transients over the testing period. There was no significant difference between cells on the two substrates, with the lone exception being the departure velocity of the calcium transient at the 48 hour time point. As mentioned, the calcium transient in cells plated at 27 kPa significantly decreased at the 24 hour time point. These cells had transient

amplitudes and velocities significantly less than cells plated at 255 kPa at the 24 hour time point. The return velocity was also significantly less compared to cells on 255 kPa substrates at the 48 hour time point. Hence, even though higher calcium gradients are often associated with negative cell effects, the cells displaying the sarcomere and costamere degradation had a significant drop in calcium signaling at the 24 hour time point.

Discussion:

The results of this study provide further evidence that cardiomyocytes are affected by the mechanical stiffness of their extracellular environment, and that the stress sensor in cardiomyocytes may be sensitive to a specific range of substrate stiffness. Although the present paper does not attempt to identify a specific mechanism by which cardiomyocytes transduce mechanical information from the extracellular environment beyond blocking phosphotase activity, it suggests that the myocyte mechanotransduction mechanism exhibits nonlinear behavior. For many other cell types, there is a specific range of substrate stiffness that produces normal cell function. The results described in this study suggest there is a range of substrate stiffness that instigates degradation of a crucial structure in the myocyte. This finding has obvious implications for the study of scar growth following myocardial infarction, as well as the appropriateness of culturing these cells on laminin-coated glass and plastic substrates.

Using PDMS substrates with defined stiffness values, immunofluoresence indicated that for substrates between 27 and 117 kPa, α-actinin is not organized in discrete z-disk structures, and integrin β1 doesn't colocalize to the z-disk. Immunoblotting showed that there are still equal amounts of α-actinin within the cells plated on different substrates, but qRT-PCR showed that cells upregulated expression of α-actinin as well as integrins β1 and α7 and vinculin. This change in transcription indicates that information about the structure disorientation might be signaled back to the nucleus in a feedback loop. Moreover, because immunoblotting indicates equal amounts of protein within the cell despite message upregulation, these results suggest that there may be some level of proteolytic activity occurring in the cells. Interestingly, the detrimental effects of the intermediate stiffness substrates were attenuated by the phosphotase inhibitor, calyculin A. Assays for cardiomyocyte contractility and calcium transients indicated that even though cells on 255 kPa and 7 kPa substrates both retain their sarcomere and costamere structure, their dynamics under pacing can be quite different. Sarcomere shortening significantly increased by the 48 hour time point in cells on 7 kPa, whereas cells on 255 kPa exhibited significantly less shortening at that time.

Moreover, the fact that cardiomyocytes on soft substrates did not sustain larger contractions demonstrates that the cardiomyocyte can be modeled as a dynamically controlled system with some element of sensing, actuating, and feedback. If the cardiomyocyte were an open loop system, it would exert the same amount of force despite the substrate stiffness. Instead, the contractility and calcium transient data indicates a complex, time-dependent response to the stiffness of the extracellular substrate that suggests there is a stress sensor located in the sarcomere and/or costamere. Additionally, the results of the message levels provide evidence of some feedback to the nucleus of the structural changes occurring in the myocyte cytoskeleton. Considering the differences between the trends in calcium transients and contractility, it is clear that these mechanisms cannot be explained solely by changes in calcium handling.

As mentioned, the results of this study have clear clinical implications. Although the majority of cardiomyocytes in a fibrotic scar following infarction die immediately due to ischemia, the cardiomyocytes in the border zone eventually die off. This facilitates scar growth and eventual heart failure. The stiffness in and surrounding the scar is increased due to augmented matrix deposition, and it is possible that the tissue reaches stiffness values that promote the structural deformations described in the present study. If the mechanism by which these cells sense extracellular stiffness can be discerned, then perhaps the pathways responsible for the malfunction can be blocked to create a cytoprotective effect. Hence, future work will focus on identifying that mechanism, for which there are plenty of candidates from all the studies seeking the cardiomyocyte stretch sensor.

Works Cited

1. Discher DE, Janmey P, Wang Y. Tissue cells feel and respond to the stiffness of their substrate. Science (2005) *310(5751): pp. 1139-1143*
2. Fu J, et al. Mechanical regulation of cell function with geometrically modulated elastomeric substrates. Nature Methods 7, 733–736 (2010)
3. Galie P, Westfall MV, Stegemann JP. Reduced serum content and increased matrix stiffness promote the cardiac myofibroblast transition in 3D collagen matrices. *Cardiovascular Pathology*. Article in press.
4. Bajaj P, et al. Stiffness of the substrate influences the phenotype of embryonic chicken cardiac myocytes. J Biomed Mater Res Part A (2010) 95A: 1261-1289.
5. Bhana B, et al. Influence of substrate stiffness on the phenotype of heart cells. Biotech and Bioeng (2009) 105:1148-1160.
6.Jacot JG, Martin JC, Hunt DL. Mechanobiology of cardiomyocyte development. Journal of Biomechanics. (2010) 43:93-98.
7. Cox L, Umans L, Cornelis F, Huylebroeck D, Zwijsen A. A broken heart: a stretch too far: an overview of mouse models with mutations in stretch-sensor components. Int J Cardiol. 2008 Dec 17;131(1):33-44.
8. Hoshijima M. Mechanical stress-strain sensors embedded in cardiac cytoskeleton: Z disk, titin, and associated structures. Am J Physiol Heart Circ Physiol (2006) 290:1313-1325.
9. Discher D, Mooney D, Zandstra P. Growth factors, matrices, and forces combine and control stem cells. Science. 2009 Jun 26;324(5935):1673-7.
10. Am J Physiol Heart Circ Physiol 290:H2196-H2203, 2006
11. Magn Reson Med. 2005 September; 54(3): 538–548.
12. Indentation Versus Tensile Measurements of Young's Modulus for Soft Biological Tissues Clayton T. McKee, Ph.D.,1 Julie A. Last, Ph.D.,2 Paul Russell, Ph.D.,1 and Christopher J. Murphy, D.V.M., Ph.D.
13. Engler AJ, Carag-Krieger C, Johnson CP, et al. Embryonic cardiomyocytes beat best on a matrix with heart-like elasticity: scar-like rigidity inhibits beating. J Cell Science (2008) 121:3794-3802.

14. Maitra N, Flink IL, Bahl JJ, Morkin E. Expression of alpha and beta integrins during terminal differentiation of cardiomyocytes. Cardiovasc Res. 2000 Sep;47(4):715-25.
15. Laser M, Willey CD, Jiang W, Cooper G, Menick DR, Zile MR, Kuppuswamy D, et al. Integrin activation and focal complex formation in cardiac hypertrophy. JBC (2000) 275(45):35624-35630.
16. Amin P, Singh M, Singh K.J β-Adrenergic Receptor-Stimulated Cardiac Myocyte Apoptosis: Role of β1 Integrins. Signal Transduct. 2011;2011:179057.
17. Maruyama R, Takemura G, Tohse N, et al. Synchronous progression of calcium transient-dependent beating and sarcomere destruction in apoptotic adult cardiomyocytes. Am J Physiol Heart Circ Physiol (2006) 290: H1493-H1502.
18. Hein S, Kostin S, Schaper J. Adult rat cardiac myocytes in culture: 'Second-floor' cells and coculture experiments. Exp Clin Cardiol 2006;11(3):175-182.
19. Ibrahim M, Masri AA, et al. Prolonged mechanical unloading affects cardiomyocyte excitation-contraction coupling, t-tubule structure, and the cell surface. FASEB journal (2010) 24:3321-3329.
20. Oshimi Y, Miyazaki S. Fas antigen-mediated DNA fragmentation and apoptotic morphologic changes are regulated by elevated Ca2+ levels. J Immunol (1995) 154:599-609.
21. Margaret V. Westfall, Elizabeth M. Rust, Faris Albayya, Joseph M. Metzger. Adenovirus-mediated myofilament gene transfer into adult cardiac myocytes. Methods in Cell Biology (1997) 52:307-322.

Figure 1: Immunofluorescence images of z-disk organization after 48 hours in culture on different substrate stiffnesses. Actin is stained by a conjugated phalloidin-FITC antibody, cell nuclei with DAPI, and α-actinin of the z-disk with a monoclonal antibody. Images are 150 x 150 μm.

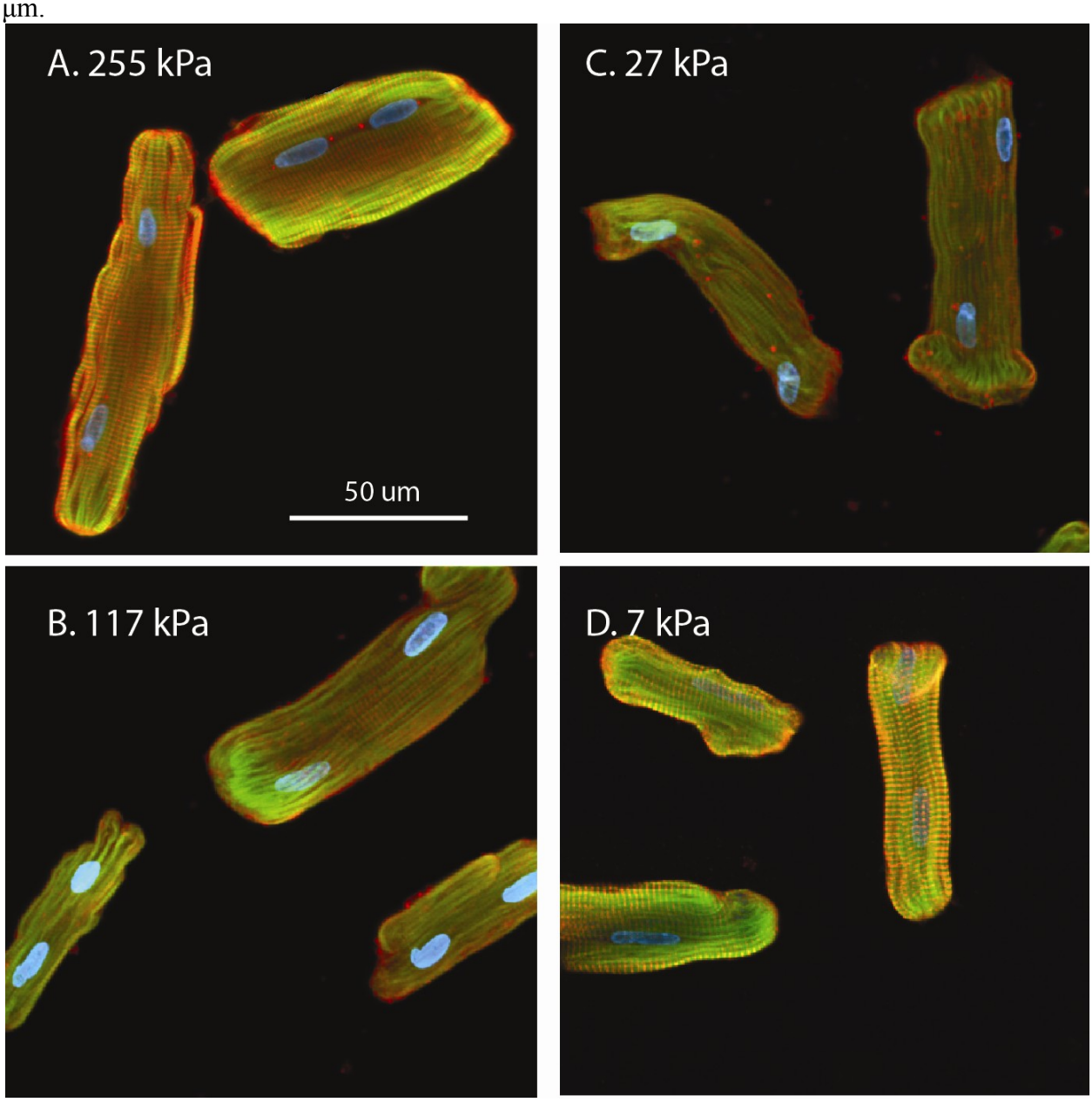

Figure 2: Immunoblot of cell homogenates from cardiomyocytes seeded on substrates with elastic moduli ranging from 255 kPa to 7 kPa for 48 hours. The blot in (A) shows representative lanes for three of the stiffnesses and (B) displays the quantification of the immunoblots.

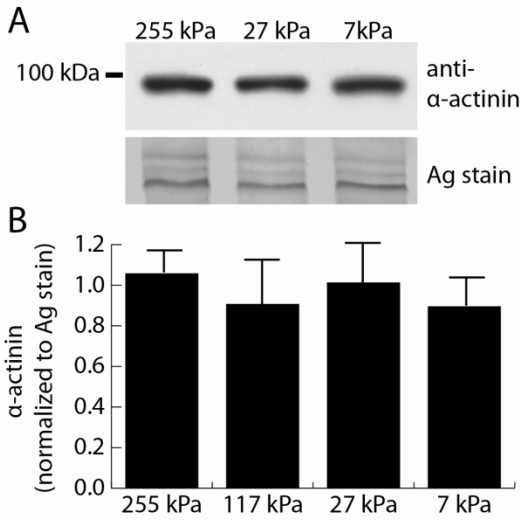

Figure 3 Immunofluorescence images of integrin β1 colocalization with the Z disk after 48 hours in culture on different substrate stiffnesses. Actin is stained by a conjugated phalloidin-FITC antibody, cell nuclei with DAPI, and integrin β1 with a monoclonal antibody.

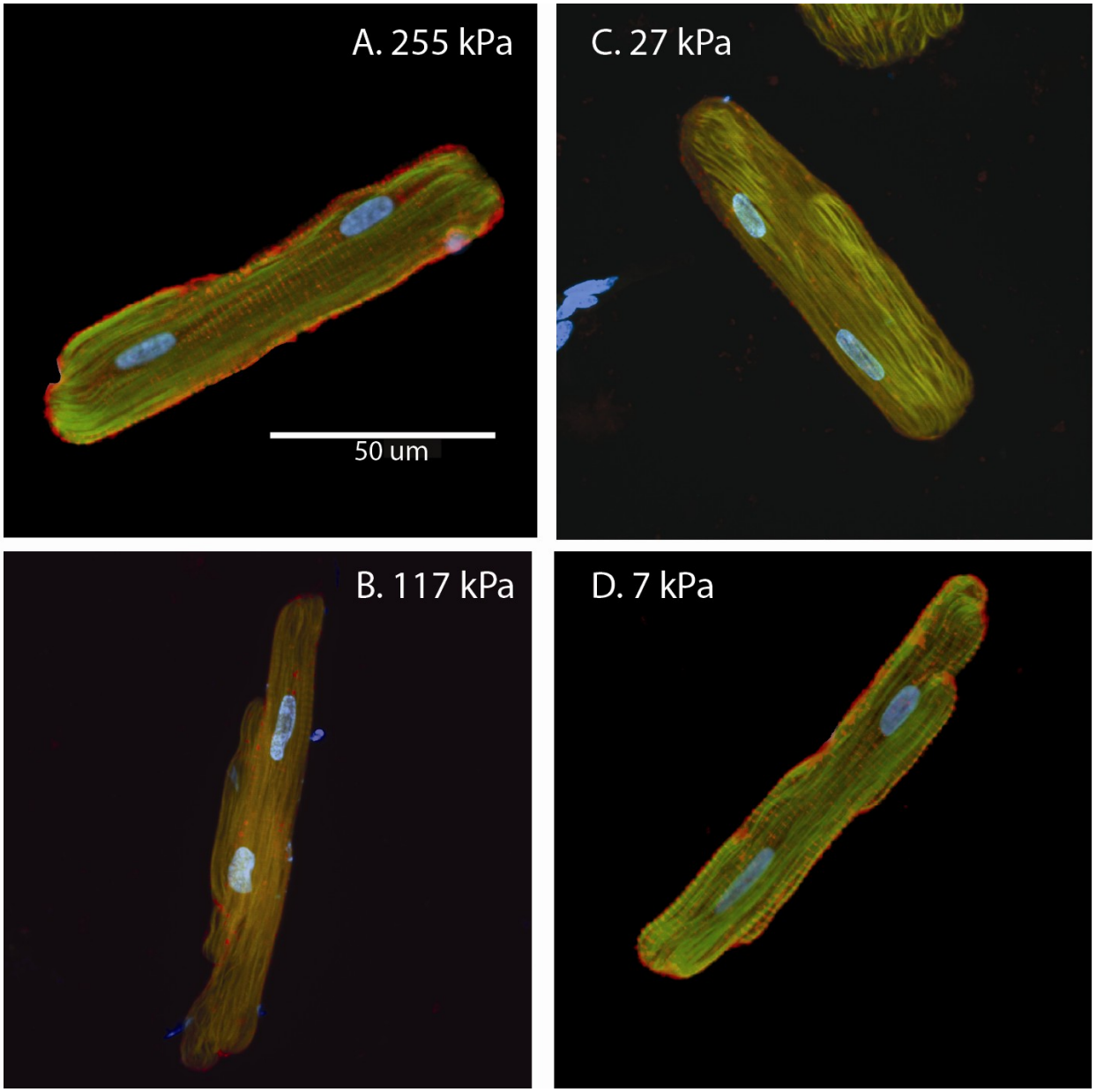

Figure 4: Message levels of four proteins associated with the sarcomere (α-actinin) and costamere complex (integrin α7, integrin β1, and vinculin) for cells seeded on substrates of four different elastic moduli at 48 hours. Significance from the 255 kPa message is denoted with a *, indicating $p < 0.05$.

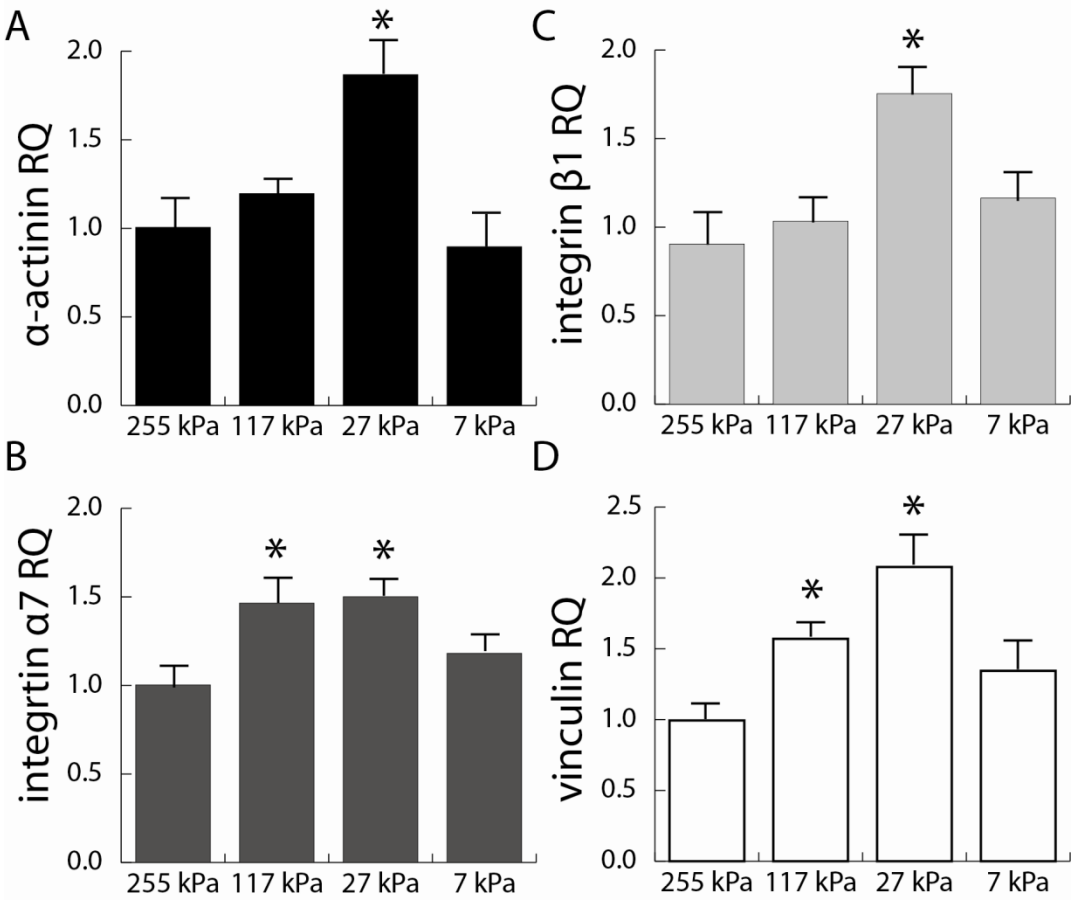

Figure 5: Immunofluorescence images of z-disk organization after 48 hours in culture on different substrate stiffnesses with the addition of 0.5 μg/mL of calyculin A. Actin is stained by a conjugated phalloidin-FITC antibody, cell nuclei with DAPI, and α-actinin of the z-disk with a monoclonal antibody.

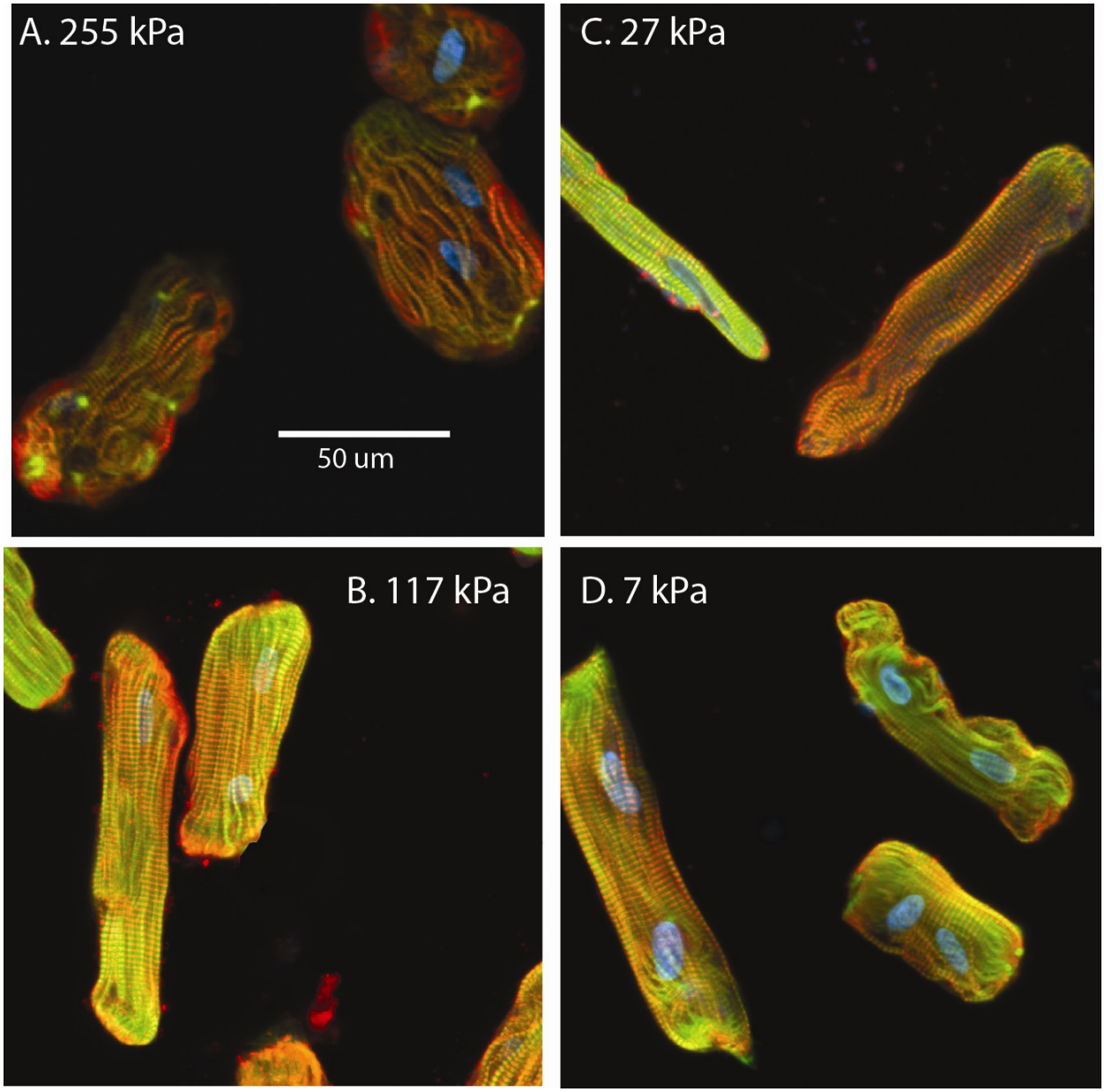

Figure 6: Contractility tests of cardiomyocytes plated for 2, 24, and 48 hours on substrates with elastic moduli of 255, 27, and 7 kPa. The left column shows averaged traces of sarcomere shortening at 2, 24, and 48 hours during electrical stimulation. The right column displays quantification of total shortening amplitude, departure velocity, and return velocity. A + denotes significance ($p < 0.05$) compared to the 2 hour time point for each stiffness value, and a * denotes significance ($p < 0.05$) compared to the 255 kPa stiffness value for each time point, as determined by Bonferroni posttests following a two-way ANOVA.

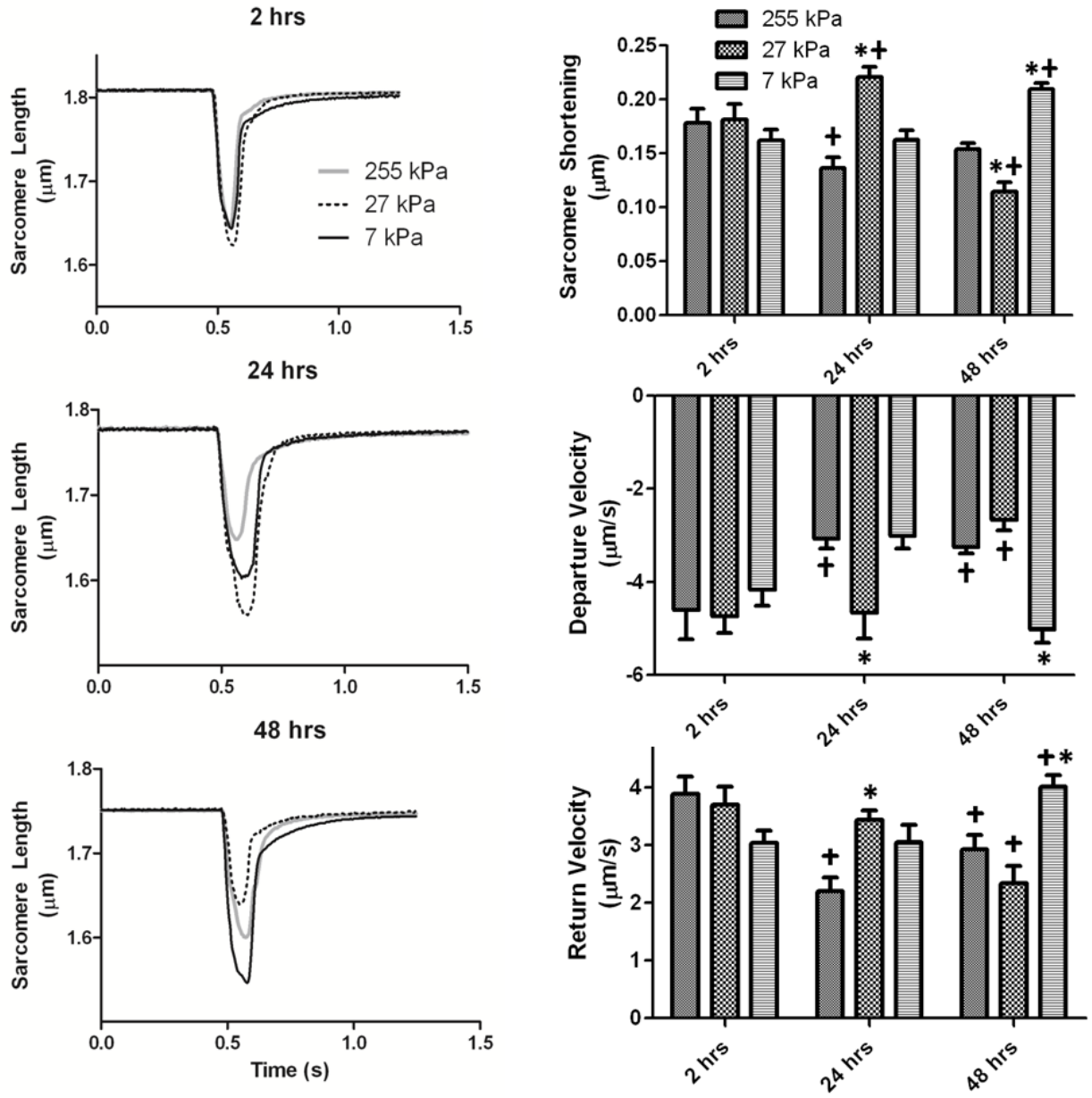

Figure 7: Intracellular calcium flux for cardiomyocytes plated for 2, 24, and 48 hours on substrates with elastic moduli of 255, 27, and 7 kPa. The left column shows averaged traces of the calcium transients of cells electrically stimulated at 2, 24, and 48 hours. The right column displays quantification of total shortening amplitude, departure velocity, and return velocity. A + denotes significance ($p < 0.05$) compared to the 2 hour time point for each stiffness value, and

a * denotes significance ($p < 0.05$) compared to the 255 kPa stiffness value for each time point, as determined by Bonferroni posttests following a two-way ANOVA.

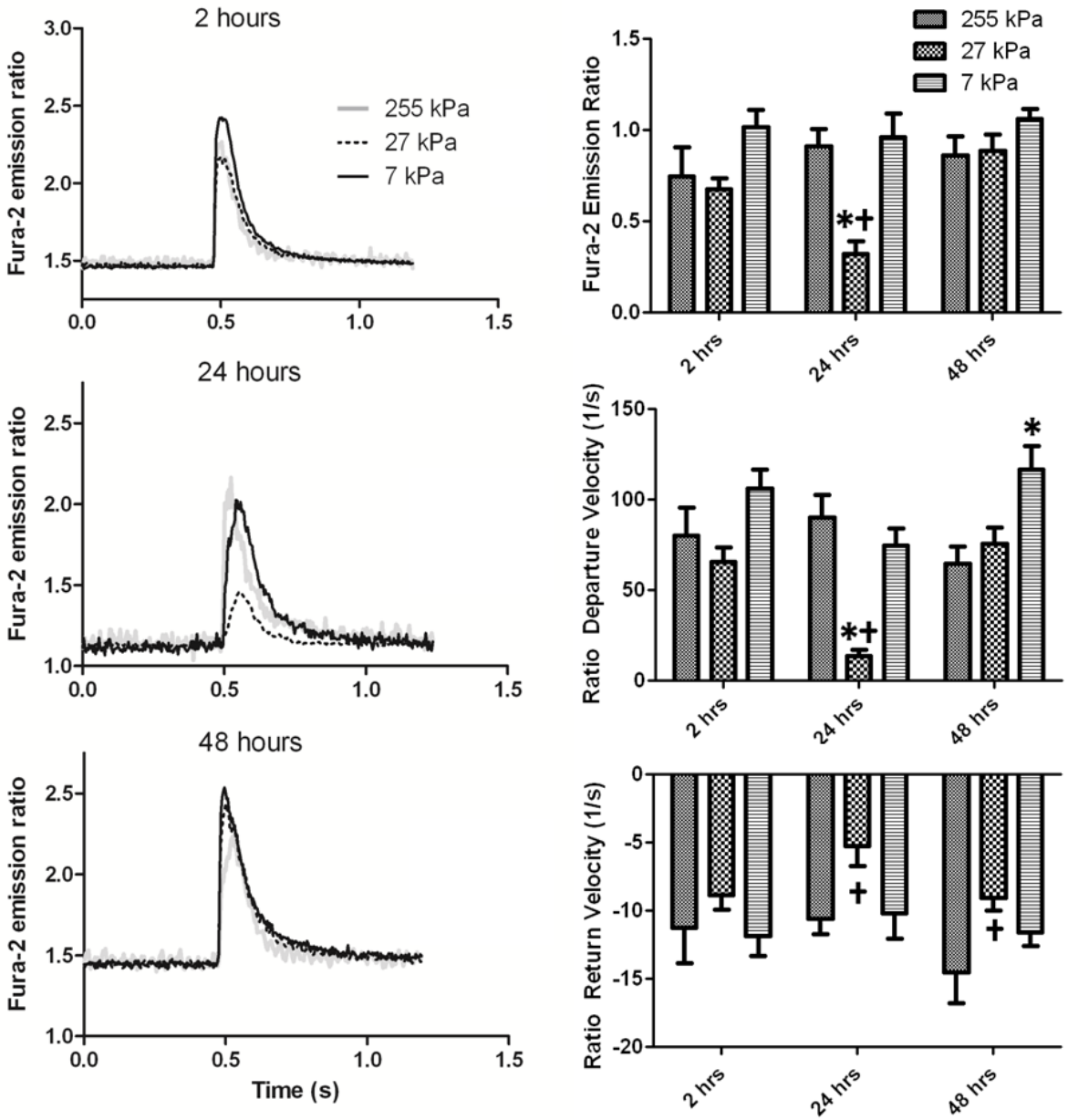

6.3 Statistical Analysis

6.3.1 Serum and matrix effects on fibroblast phenotype

<u>Compaction of released gels, Figure 4.1</u>

Welch Two Sample t-test – null hypothesis comparisons not included.

1. data: M199 6 hours
t = -8.0481, df = 2.906, p-value = 0.004493
alternative hypothesis: true difference in means is not equal to 0
95 percent confidence interval:
-0.18455874 -0.07858126
sample estimates:
mean of x mean of y
0.2782667 0.4098367

2. data: M199 24 hours
t = -3.8999, df = 3.199, p-value = 0.02662
alternative hypothesis: true difference in means is not equal to 0
95 percent confidence interval:
-0.12430591 -0.01473859
sample estimates:
mean of x mean of y
0.2341000 0.3036222

3. data: M199 48 hours
t = -6.1346, df = 4.942, p-value = 0.001742
alternative hypothesis: true difference in means is not equal to 0
95 percent confidence interval:
-0.13300863 -0.05425837
sample estimates:
mean of x mean of y
0.1367590 0.2303925

4. data: M199 120 hours
t = -5.0726, df = 2.666, p-value = 0.01958
alternative hypothesis: true difference in means is not equal to 0
95 percent confidence interval:
-0.08613980 -0.01675636
sample estimates:
mean of x mean of y
0.08133867 0.13278675

5. data: DMEM 6 hours
t = -4.2184, df = 2.327, p-value = 0.03955
alternative hypothesis: true difference in means is not equal to 0
95 percent confidence interval:
-0.076791803 -0.004288197
sample estimates:
mean of x mean of y
0.32630 0.36684

6. data: DMEM 24 hours
t = -8.8441, df = 3.995, p-value = 0.0009071
alternative hypothesis: true difference in means is not equal to 0
95 percent confidence interval:
-0.06230362 -0.03252172
sample estimates:
mean of x mean of y
0.2544707 0.3018833

7. data: DMEM 48 hours
t = -2.6051, df = 5.318, p-value = 0.0452
alternative hypothesis: true difference in means is not equal to 0
95 percent confidence interval:
-0.070397705 -0.001099228
sample estimates:
mean of x mean of y
0.1950313 0.2307798

8. data: DMEM 120 hours
t = -2.4967, df = 7, p-value = 0.04119
alternative hypothesis: true difference in means is not equal to 0
95 percent confidence interval:
-0.050762698 -0.001378702
sample estimates:
mean of x mean of y
0.1797965 0.2058672

Released gel message levels (1: 5%,6hrs, 2: 10%,6hrs, 3: 5%,24hrs, 4: 10%,24hrs, etc.), Figures 4.4-4.5

Post-hoc Tukey tests after one way ANOVAs

M199, col1a1

```
>col1a1=c(0.532,0.613,0.6058,0.773,0.902,0.787,0.7699,0.538,0.563,0.561,0.772,0.719,0.440,0.
364,0.3453,0.316,0.456,0.457,0.531,0.387,0.542,0.466,0.47,0.389,0.4514,0.404,0.314,0.429,0.42
4,0.56,0.393,0.416);
> time=c(rep(1,3),rep(2,4),rep(3,3),rep(4,3),rep(5,3),rep(6,6),rep(7,5),rep(8,5));
> time=as.factor(time);
> TukeyHSD(aov(col1a1~time),conf.level=0.95);
  Tukey multiple comparisons of means
    95% family-wise confidence level

Fit: aov(formula = col1a1 ~ time)

$time
          diff         lwr          upr     p adj
2-1  0.22437500  0.03845962  0.4102903816 0.0105553
3-1 -0.02960000 -0.22835190  0.1691519031 0.9995910
4-1  0.06006667 -0.13868524  0.2588185698 0.9698324
5-1 -0.24183333 -0.44058524 -0.0430814302 0.0097694
6-1 -0.11043333 -0.28255753  0.0616908638 0.4281169
7-1 -0.17792000 -0.35568911 -0.0001508936 0.0496976
8-1 -0.13920000 -0.31696911  0.0385691064 0.2065699
3-2 -0.25397500 -0.43989038 -0.0680596184 0.0029801
4-2 -0.16430833 -0.35022371  0.0216070483 0.1108789
5-2 -0.46620833 -0.65212371 -0.2802929517 0.0000004
6-2 -0.33480833 -0.49193551 -0.1776811575 0.0000067
7-2 -0.40229500 -0.56558635 -0.2390036490 0.0000006
8-2 -0.36357500 -0.52686635 -0.2002836490 0.0000032
4-3  0.08966667 -0.10908524  0.2884185698 0.8030440
5-3 -0.21223333 -0.41098524 -0.0134814302 0.0304991
6-3 -0.08083333 -0.25295753  0.0912908638 0.7706533
7-3 -0.14832000 -0.32608911  0.0294491064 0.1518542
8-3 -0.10960000 -0.28736911  0.0681691064 0.4768342
5-4 -0.30190000 -0.50065190 -0.1031480969 0.0008649
6-4 -0.17050000 -0.34262420  0.0016241972 0.0534772
7-4 -0.23798667 -0.41575577 -0.0602175602 0.0037118
8-4 -0.19926667 -0.37703577 -0.0214975602 0.0204707
6-5  0.13140000 -0.04072420  0.3035241972 0.2311043
7-5  0.06391333 -0.11385577  0.2416824398 0.9268929
8-5  0.10263333 -0.07513577  0.2804024398 0.5562325
7-6 -0.06748667 -0.21488502  0.0799116897 0.7915290
```

8-6 -0.02876667 -0.17616502 0.1186316897 0.9976788
8-7 0.03872000 -0.11523256 0.1926725622 0.9892190

DMEM, col1a1

```
>col1a1=c(1.393,1.282691,1.1718,1.382,1.004,1.363,1.227,0.7402,0.9257,0.862,0.731,0.8346,0.
665,0.865,0.5835,0.7074,0.4811,0.577,0.46,0.5999,0.733,0.597,0.289,0.304,0.3477,0.40244,0.67
4,0.382,0.386,0.3914,0.346,0.394,0.316,0.471,0.1888,0.3697,0.32213,0.296);
> time=c(rep(1,3),rep(2,4),rep(3,5),rep(4,5),rep(5,5),rep(6,4),rep(7,6),rep(8,6));
> time=as.factor(time);
> TukeyHSD(aov(col1a1~time),conf.level=0.95);
  Tukey multiple comparisons of means
    95% family-wise confidence level

Fit: aov(formula = col1a1 ~ time)

$time
           diff        lwr         upr     p adj
2-1 -0.038497000 -0.3207109  0.243716945 0.9998072
3-1 -0.463797000 -0.7336451 -0.193948855 0.0001077
4-1 -0.622097000 -0.8919451 -0.352248855 0.0000006
5-1 -0.689117000 -0.9589651 -0.419268855 0.0000001
6-1 -0.946712000 -1.2289259 -0.664498055 0.0000000
7-1 -0.853597000 -1.1148763 -0.592317657 0.0000000
8-1 -0.955225333 -1.2165047 -0.693945990 0.0000000
3-2 -0.425300000 -0.6731713 -0.177428651 0.0001105
4-2 -0.583600000 -0.8314713 -0.335728651 0.0000004
5-2 -0.650620000 -0.8984913 -0.402748651 0.0000000
6-2 -0.908215000 -1.1694943 -0.646935657 0.0000000
7-2 -0.815100000 -1.0536143 -0.576585683 0.0000000
8-2 -0.916728333 -1.1552426 -0.678214017 0.0000000
4-3 -0.158300000 -0.3919953  0.075395349 0.3776352
5-3 -0.225320000 -0.4590153  0.008375349 0.0650503
6-3 -0.482915000 -0.7307863 -0.235043651 0.0000138
7-3 -0.389800000 -0.6135463 -0.166053738 0.0000872
8-3 -0.491428333 -0.7151746 -0.267682071 0.0000016
5-4 -0.067020000 -0.3007153  0.166675349 0.9801132
6-4 -0.324615000 -0.5724863 -0.076743651 0.0040583
7-4 -0.231500000 -0.4552463 -0.007753738 0.0385035
8-4 -0.333128333 -0.5568746 -0.109382071 0.0008437
6-5 -0.257595000 -0.5054663 -0.009723651 0.0371807
7-5 -0.164480000 -0.3882263  0.059266262 0.2813424
8-5 -0.266108333 -0.4898546 -0.042362071 0.0112132
7-6  0.093115000 -0.1453993  0.331629317 0.9026563
8-6 -0.008513333 -0.2470276  0.230000983 1.0000000
8-7 -0.101628333 -0.3149620  0.111705357 0.7746776
```

M199, col3a1

```
>col3a1=c(0.532,0.452,0.613,0.8899,0.5249,0.7802,0.9014,0.521,0.606,0.4892,0.644,0.68,0.449
,0.616,0.844,0.352,0.274,0.437,0.432,0.4252,0.719,0.783,0.941,0.9477,1.122,0.620,0.634,0.762,
0.8055,0.7427,0.7481,1.237,1.437,1.439,1.4822,0.932,0.845,1.437,1.581,1.627);
> time=c(rep(1,3),rep(2,4),rep(3,6),rep(4,7),rep(5,4),rep(6,7),rep(7,4),rep(8,5));
> time=as.factor(time);
> TukeyHSD(aov(col3a1~time),conf.level=0.95);
  Tukey multiple comparisons of means
    95% family-wise confidence level

Fit: aov(formula = col3a1 ~ time)

$time
          diff        lwr        upr     p adj
2-1  0.241766667 -0.22778111 0.71131444 0.7067279
3-1  0.032533333 -0.40218344 0.46725010 0.9999969
4-1 -0.049447619 -0.47368775 0.37479251 0.9999358
5-1  0.315341667 -0.15420611 0.78488944 0.3921213
6-1  0.243995238 -0.18024489 0.66823537 0.5843787
7-1  0.866466667  0.39691889 1.33601444 0.0000293
8-1  0.752066667  0.30309312 1.20104022 0.0001417
3-2 -0.209233333 -0.60607364 0.18760697 0.6823008
4-2 -0.291214286 -0.67654952 0.09412095 0.2537574
5-2  0.073575000 -0.36114177 0.50829177 0.9992370
6-2  0.002228571 -0.38310666 0.38756380 1.0000000
7-2  0.624700000  0.18998323 1.05941677 0.0012546
8-2  0.510300000  0.09789146 0.92270854 0.0073079
4-3 -0.081980952 -0.42401428 0.26005237 0.9932361
5-3  0.282808333 -0.11403197 0.67964864 0.3201178
6-3  0.211461905 -0.13057142 0.55349523 0.4958051
7-3  0.833933333  0.43709303 1.23077364 0.0000028
8-3  0.719533333  0.34726413 1.09180253 0.0000131
5-4  0.364789286 -0.02054595 0.75012452 0.0740278
6-4  0.293442857 -0.03517213 0.62205785 0.1078272
7-4  0.915914286  0.53057905 1.30124952 0.0000002
8-4  0.801514286  0.44153460 1.16149397 0.0000009
6-5 -0.071346429 -0.45668166 0.31398880 0.9986396
7-5  0.551125000  0.11640823 0.98584177 0.0056231
8-5  0.436725000  0.02431646 0.84913354 0.0317741
7-6  0.622471429  0.23713620 1.00780666 0.0002459
8-6  0.508071429  0.14809174 0.86805111 0.0015806
8-7 -0.114400000 -0.52680854 0.29800854 0.9840733
```

DMEM, col3a1

```
>col3a1=c(0.835,0.9108,0.9833,0.451,0.669,0.7899,0.6,0.626,0.791,0.526,0.824,1.288,0.439,0.3
73,0.434,0.343,0.397,1.201,1.288,1.521,1.534,0.563,0.753,0.817,0.917,0.861,1.07,1.663,1.711,1.
4923,1.24,1.46,2.33,2.21,2.193);
>  time=c(rep(1,3),rep(2,4),rep(3,5),rep(4,5),rep(5,4),rep(6,6),rep(7,3),rep(8,5));
> time=as.factor(time);
>  TukeyHSD(aov(col3a1~time),conf.level=0.95);
  Tukey multiple comparisons of means
    95% family-wise confidence level

Fit: aov(formula = col3a1 ~ time)

$time
          diff        lwr         upr     p adj
2-1 -0.28222500 -0.90518996  0.34073996 0.8081382
3-1 -0.09870000 -0.69436844  0.49696844 0.9992531
4-1 -0.51250000 -1.10816844  0.08316844 0.1311537
5-1  0.47630000 -0.14666496  1.09926496 0.2347101
6-1 -0.07953333 -0.65628682  0.49722015 0.9997762
7-1  0.71240000  0.04642244  1.37837756 0.0296937
8-1  0.97690000  0.38123156  1.57256844 0.0002622
3-2  0.18352500 -0.36363140  0.73068140 0.9512860
4-2 -0.23027500 -0.77743140  0.31688140 0.8582359
5-2  0.75852500  0.18177152  1.33527848 0.0041390
6-2  0.20269167 -0.32380982  0.72919316 0.9046333
7-2  0.99462500  0.37166004  1.61758996 0.0003803
8-2  1.25912500  0.71196860  1.80628140 0.0000010
4-3 -0.41380000 -0.92966400  0.10206400 0.1884983
5-3  0.57500000  0.02784360  1.12215640 0.0342531
6-3  0.01916667 -0.47473551  0.51306884 1.0000000
7-3  0.81110000  0.21543156  1.40676844 0.0028054
8-3  1.07560000  0.55973600  1.59146400 0.0000061
5-4  0.98880000  0.44164360  1.53595640 0.0000628
6-4  0.43296667 -0.06093551  0.92686884 0.1179899
7-4  1.22490000  0.62923156  1.82056844 0.0000077
8-4  1.48940000  0.97353600  2.00526400 0.0000000
6-5 -0.55583333 -1.08233482 -0.02933184 0.0330265
7-5  0.23610000 -0.38686496  0.85906496 0.9113407
8-5  0.50060000 -0.04655640  1.04775640 0.0912985
7-6  0.79193333  0.21517985  1.36868682 0.0025485
8-6  1.05643333  0.56253116  1.55033551 0.0000039
8-7  0.26450000 -0.33116844  0.86016844 0.8228921
```

M199, TGF-beta

```
>tgfbeta=c(1,1.206,1.4748,1.169,1.2014,1.174,1.727,2.7933,2.402,2.0718,1.349,1.717,1.536,1.5
36,1.037,1.156,1.198,1.145,0.7609,0.749,0.707562,0.987,0.79,1.107,0.743,1.070,0.8814);
> time=c(rep(1,4),rep(2,3),rep(3,3),rep(4,4),rep(5,3),rep(6,3),rep(7,3),rep(8,4));
> time=as.factor(time);
> TukeyHSD(aov(tgfbeta~time),conf.level=0.95);
Tukey multiple comparisons of means
   95% family-wise confidence level

Fit: aov(formula = tgfbeta ~ time)

$time
         diff       lwr        upr     p adj
2-1  0.15501667 -0.4028744  0.71290769 0.9774046
3-1  1.20991667  0.6520256  1.76780769 0.0000134
4-1  0.32205000 -0.1944567  0.83855672 0.4409338
5-1 -0.08211667 -0.6400077  0.47577435 0.9995276
6-1 -0.32748333 -0.8853744  0.23040769 0.5126691
7-1 -0.38426267 -0.9421537  0.17362835 0.3255497
8-1 -0.26210000 -0.7786067  0.25440672 0.6753356
3-2  1.05490000  0.4584894  1.65131059 0.0002016
4-2  0.16703333 -0.3908577  0.72492435 0.9662738
5-2 -0.23713333 -0.8335439  0.35927725 0.8689342
6-2 -0.48250000 -1.0789106  0.11391059 0.1691658
7-2 -0.53927933 -1.1356899  0.05713125 0.0941385
8-2 -0.41711667 -0.9750077  0.14077435 0.2395410
4-3 -0.88786667 -1.4457577 -0.32997565 0.0007129
5-3 -1.29203333 -1.8884439 -0.69562275 0.0000136
6-3 -1.53740000 -2.1338106 -0.94098941 0.0000011
7-3 -1.59417933 -2.1905899 -0.99776875 0.0000006
8-3 -1.47201667 -2.0299077 -0.91412565 0.0000007
5-4 -0.40416667 -0.9620577  0.15372435 0.2712610
6-4 -0.64953333 -1.2074244 -0.09164231 0.0158470
7-4 -0.70631267 -1.2642037 -0.14842165 0.0076021
8-4 -0.58415000 -1.1006567 -0.06764328 0.0200958
6-5 -0.24536667 -0.8417773  0.35104392 0.8488078
7-5 -0.30214600 -0.8985566  0.29426459 0.6770272
8-5 -0.17998333 -0.7378744  0.37790769 0.9504772
7-6 -0.05677933 -0.6531899  0.53963125 0.9999743
8-6  0.06538333 -0.4925077  0.62327435 0.9998954
8-7  0.12216267 -0.4357284  0.68005369 0.9942532
```

DMEM, TGF-beta

```
>tgfbeta=c(1.20144,1.5686,1.511,1.544,1.129,0.989,2.304,2.426,2.3835,1.397,2.124,1.639,1.383
,1.499,1.544,2.155,2.378,1.73,1.358,1.529,1.708,1.114212,1.1119,0.75585,1.0684,1.574,1.828,1.
292,1.876,1.342,2.193);
> time=c(rep(1,3),rep(2,3),rep(3,3),rep(4,3),rep(5,4),rep(6,5),rep(7,4),rep(8,6));
> time=as.factor(time);
> TukeyHSD(aov(tgfbeta~time),conf.level=0.95);
  Tukey multiple comparisons of means
    95% family-wise confidence level

Fit: aov(formula = tgfbeta ~ time)

$time
          diff        lwr         upr     p adj
2-1 -0.20634667 -1.04091430  0.62822096 0.9899351
3-1  0.94415333  0.10958570  1.77872096 0.0191074
4-1  0.29298667 -0.54158096  1.12755430 0.9333296
5-1  0.21823667 -0.56242987  0.99890320 0.9797350
6-1  0.31358667 -0.43287331  1.06004665 0.8496339
7-1 -0.41442283 -1.19508937  0.36624370 0.6478160
8-1  0.25715333 -0.46560344  0.97991010 0.9288632
3-2  1.15050000  0.31593237  1.98506763 0.0028000
4-2  0.49933333 -0.33523430  1.33390096 0.5094483
5-2  0.42458333 -0.35608320  1.20524987 0.6211529
6-2  0.51993333 -0.22652665  1.26639331 0.3272109
7-2 -0.20807617 -0.98874270  0.57259037 0.9844922
8-2  0.46350000 -0.25925677  1.18625677 0.4251161
4-3 -0.65116667 -1.48573430  0.18340096 0.2081928
5-3 -0.72591667 -1.50658320  0.05474987 0.0812501
6-3 -0.63056667 -1.37702665  0.11589331 0.1413358
7-3 -1.35857617 -2.13924270 -0.57790963 0.0001587
8-3 -0.68700000 -1.40975677  0.03575677 0.0705968
5-4 -0.07475000 -0.85541653  0.70591653 0.9999780
6-4  0.02060000 -0.72585998  0.76705998 1.0000000
7-4 -0.70740950 -1.48807603  0.07325703 0.0952030
8-4 -0.03583333 -0.75859010  0.68692344 0.9999998
6-5  0.09535000 -0.59031728  0.78101728 0.9997297
7-5 -0.63265950 -1.35541627  0.09009727 0.1164212
8-5  0.03891667 -0.62086698  0.69870031 0.9999992
7-6 -0.72800950 -1.41367678 -0.04234222 0.0320400
8-6 -0.05643333 -0.67536525  0.56249859 0.9999842
8-7  0.67157617  0.01179252  1.33135981 0.0440244
```

M199, alpha-sma

```
>Malphsma=c(1,0.8827,0.8062,0.7435,0.499,0.4503,0.4124,0.3578,0.249,0.2300,0.213009,0.07
1,0.134,0.294,0.2208,0.271,0.5432,0.2037,0.089,0.105,0.419,0.345,0.402,0.378,0.417,0.656861,
0.5491,0.491,0.3781,0.3978,0.4233);
> time=c(rep(1,4),rep(2,4),rep(3,3),rep(4,4),rep(5,3),rep(6,6),rep(7,3),rep(8,4));
> time=as.factor(time);
> TukeyHSD(aov(Malphsma~time),conf.level=0.95);
  Tukey multiple comparisons of means
    95% family-wise confidence level

Fit: aov(formula = Malphsma ~ time)

$time
          diff         lwr         upr     p adj
2-1 -0.42822500 -0.693077060 -0.16337294 0.0004211
3-1 -0.62743033 -0.913503254 -0.34135741 0.0000050
4-1 -0.67815000 -0.943002060 -0.41329794 0.0000004
5-1 -0.51880000 -0.804872921 -0.23272708 0.0000894
6-1 -0.56843333 -0.810209080 -0.32665759 0.0000016
7-1 -0.31711300 -0.603185921 -0.03104008 0.0226723
8-1 -0.43555000 -0.700402060 -0.17069794 0.0003382
3-2 -0.19920533 -0.485278254  0.08686759 0.3275188
4-2 -0.24992500 -0.514777060  0.01492706 0.0740012
5-2 -0.09057500 -0.376647921  0.19549792 0.9603848
6-2 -0.14020833 -0.381984080  0.10156741 0.5469328
7-2  0.11111200 -0.174960921  0.39718492 0.8929647
8-2 -0.00732500 -0.272177060  0.25752706 1.0000000
4-3 -0.05071967 -0.336792588  0.23535325 0.9986898
5-3  0.10863033 -0.197194483  0.41445515 0.9294310
6-3  0.05899700 -0.205855060  0.32384906 0.9945847
7-3  0.31031733  0.004492517  0.61614215 0.0450382
8-3  0.19188033 -0.094192588  0.47795325 0.3711982
5-4  0.15935000 -0.126722921  0.44542292 0.5940537
6-4  0.10971667 -0.132059080  0.35149241 0.7952409
7-4  0.36103700  0.074964079  0.64710992 0.0070021
8-4  0.24260000 -0.022252060  0.50745206 0.0891862
6-5 -0.04963333 -0.314485394  0.21521873 0.9981382
7-5  0.20168700 -0.104137817  0.50751182 0.3913691
8-5  0.08325000 -0.202822921  0.36932292 0.9747241
7-6  0.25132033 -0.013531727  0.51617239 0.0713842
8-6  0.13288333 -0.108892413  0.37465908 0.6093353
8-7 -0.11843700 -0.404509921  0.16763592 0.8585796
```

DMEM, alpha-sma

```
>Dasma=c(0.556,0.5456,0.60155,0.39,0.4354,0.3556,0.223,0.0138,0.007558,0.009328,0.035,0.0
34644,0.03255,0.017,0.0161,0.0184,0.009,0.0147,0.017,0.23,0.2255,0.2375,0.1357,0.02,0.036,0.
045,0.044,0.484,0.526605,0.45172,0.4329,0.41063,0.1546,0.15597,0.1654,0.1446,0.208);
> time=c(rep(1,3),rep(2,4),rep(3,6),rep(4,6),rep(5,4),rep(6,4),rep(7,5),rep(8,5));
> time=as.factor(time);
> TukeyHSD(aov(Dasma~time),conf.level=0.95);
  Tukey multiple comparisons of means
    95% family-wise confidence level

Fit: aov(formula = Dasma ~ time)

$time
          diff        lwr         upr     p adj
2-1 -0.21671667 -0.31564773 -0.11778560 0.0000019
3-1 -0.54557000 -0.63716237 -0.45397763 0.0000000
4-1 -0.55235000 -0.64394237 -0.46075763 0.0000000
5-1 -0.36054167 -0.45947273 -0.26161060 0.0000000
6-1 -0.53146667 -0.63039773 -0.43253560 0.0000000
7-1 -0.10654567 -0.20114186 -0.01194947 0.0188806
8-1 -0.40200267 -0.49659886 -0.30740647 0.0000000
3-2 -0.32885333 -0.41246535 -0.24524132 0.0000000
4-2 -0.33563333 -0.41924535 -0.25202132 0.0000000
5-2 -0.14382500 -0.23541737 -0.05223263 0.0004287
6-2 -0.31475000 -0.40634237 -0.22315763 0.0000000
7-2  0.11017100  0.02327885  0.19706315 0.0058985
8-2 -0.18528600 -0.27217815 -0.09839385 0.0000031
4-3 -0.00678000 -0.08156486  0.06800486 0.9999875
5-3  0.18502833  0.10141632  0.26864035 0.0000016
6-3  0.01410333 -0.06950868  0.09771535 0.9992035
7-3  0.43902433  0.36058931  0.51745935 0.0000000
8-3  0.14356733  0.06513231  0.22200235 0.0000430
5-4  0.19180833  0.10819632  0.27542035 0.0000008
6-4  0.02088333 -0.06272868  0.10449535 0.9908490
7-4  0.44580433  0.36736931  0.52423935 0.0000000
8-4  0.15034733  0.07191231  0.22878235 0.0000201
6-5 -0.17092500 -0.26251737 -0.07933263 0.0000314
7-5  0.25399600  0.16710385  0.34088815 0.0000000
8-5 -0.04146100 -0.12835315  0.04543115 0.7710476
7-6  0.42492100  0.33802885  0.51181315 0.0000000
8-6  0.12946400  0.04257185  0.21635615 0.0008693
8-7 -0.29545700 -0.37737971 -0.21353429 0.0000000
```

Mechanical testing of released gels, Figure 4.6

Welch Two Sample t-test – null hypothesis comparisons not included.

1. data: M199, 6hrs, elastic modulus, 5% vs. 10%
t = -3.6019, df = 3.448, p-value = 0.02917
alternative hypothesis: true difference in means is not equal to 0
95 percent confidence interval:
 -6622.3472 -646.9862
sample estimates:
mean of x mean of y
 18290.00 21924.67

2. data: M199, 6hrs, phase angle, 5% vs. 10%
t = -22.5061, df = 3.935, p-value = 2.636e-05
alternative hypothesis: true difference in means is not equal to 0
95 percent confidence interval:
 -21.17529 -16.49737
sample estimates:
mean of x mean of y
 18.29033 37.12667

6.3.2 Mechanical and biochemical stimulation of fibroblasts

Control conditions (1: initial, 2: 48hr, 3: 72hr), Figure 4.14

Post-hoc Tukey tests after one way ANOVAs

Col1a1

```
>Mcol1=c(1,1.082,1.4075,1,1.1578,1,0.684,1.494,1,1.017,1.7566,1.631,1.3775,1.118,0.966,0.89
7,1.188,1.218,1.166,1.338,1.535,2.542,2.541,2.225,1.795,1.796);
> time=c(rep(1,10),rep(2,11),rep(3,5));
> time=as.factor(time);
> TukeyHSD(aov(Mcol1~time),conf.level=0.95);
  Tukey multiple comparisons of means
    95% family-wise confidence level

Fit: aov(formula = Mcol1 ~ time)

$time
       diff       lwr       upr     p adj
2-1 0.20587 -0.0962987 0.5080387 0.2243602
3-1 1.09557  0.7167815 1.4743585 0.0000007
3-2 0.88970  0.5166949 1.2627051 0.0000125
```

Col3a1

```
>col3a1=c(1,0.972,1.017,0.767,1,0.955,1,0.811,1.234,1,0.843,2.027,1.552,1.419,1.8883,1.009,1.
416,1.347,2.818,3.095,3.99,4.492);
> time=c(rep(1,11),rep(2,7),rep(3,4));
> time=as.factor(time);
> TukeyHSD(aov(col3a1~time),conf.level=0.95);
  Tukey multiple comparisons of means
    95% family-wise confidence level

Fit: aov(formula = col3a1 ~ time)

$time
        diff       lwr      upr     p adj
2-1 0.5590688 0.09793706 1.020201 1.62e-02
3-1 2.6352045 2.07833503 3.192074 0.00e+00
3-2 2.0761357 1.47834181 2.673930 1.00e-07
```

TGF-beta

```
>tgfbeta=c(1,1.004,1.059,0.613,1,1.0798,1,0.745,1.096,1,0.735,0.245,0.525,0.333,0.385,0.5501,
0.667,0.626,0.404,0.3008,0.462,0.4402);
> time=c(rep(1,11),rep(2,7),rep(3,5));
> time=as.factor(time);
> TukeyHSD(aov(tgfbeta~time),conf.level=0.95);
  Tukey multiple comparisons of means
    95% family-wise confidence level

Fit: aov(formula = tgfbeta ~ time)

$time
         diff       lwr         upr     p adj
2-1 -0.3470688 -0.5346775 -0.15946013 0.0004054
3-1 -0.4926545 -0.7019408 -0.28336827 0.0000230
3-2 -0.1455857 -0.3727911  0.08161971 0.2601283
```

alpha-SMA

```
>alphasma=c(1,1.0613,1.2332,0.84556,1,1.465,1,0.6114,0.8978,1,0.712,3.24,2.965,2.993,3.552,
4.50,3.722);
> time=c(rep(1,11),rep(2,3),rep(3,3));
> time=as.factor(time);
> TukeyHSD(aov(alphasma~time),conf.level=0.95);
  Tukey multiple comparisons of means
    95% family-wise confidence level

Fit: aov(formula = alphasma ~ time)

$time
        diff       lwr      upr     p adj
2-1 2.0817945 1.6046771 2.558912 0.0000001
3-1 2.9404612 2.4633437 3.417579 0.0000000
3-2 0.8586667 0.2605682 1.456765 0.0056287
```

Flow/Strain/Hypoxia (1: initial, 2: control, 3: flow, 4: strain, 5: flow+strain, 6: hypoxia), Figure 4.15

Post-hoc Tukey tests after one way ANOVAs

Col1a1

```
>Mcol1=c(1,1.082,1.4075,1,1.1578,1,0.684,1.494,1,1.017,1.7566,1.631,1.3775,1.118,0.966,0.89
7,1.188,1.218,1.166,1.338,1.535,1.172,1.244,1.3402,1.608,1.6704,1.093765,0.8942,0.855258,1.0
8533,0.97,0.873,1.44593,1.25576,1.534882,0.828,0.96,1.266,1.103);
> time=c(rep(1,10),rep(2,11),rep(3,5),rep(4,6),rep(5,3),rep(6,4));
> time=as.factor(time);
> TukeyHSD(aov(Mcol1~time),conf.level=0.95);
  Tukey multiple comparisons of means
    95% family-wise confidence level

Fit: aov(formula = Mcol1 ~ time)

$time
          diff        lwr        upr     p adj
2-1  0.205870000 -0.08452120  0.49626120 0.2909117
3-1  0.322690000 -0.04133463  0.68671463 0.1065743
4-1 -0.122304500 -0.46551021  0.22090121 0.8867898
5-1  0.327960667 -0.10954249  0.76546383 0.2363029
6-1 -0.044980000 -0.43817154  0.34821154 0.9992833
3-2  0.116820000 -0.24164668  0.47528668 0.9193709
4-2 -0.328174500 -0.66547939  0.00913039 0.0602980
5-2  0.122090667 -0.31079897  0.55498031 0.9549126
6-2 -0.250850000 -0.63890156  0.13720156 0.3889342
4-3 -0.444994500 -0.84743887 -0.04255013 0.0232199
5-3  0.005270667 -0.48009551  0.49063684 1.0000000
6-3 -0.367670000 -0.81350730  0.07816730 0.1553525
5-4  0.450265167 -0.01968861  0.92021895 0.0666955
6-4  0.077324500 -0.35168264  0.50633164 0.9937711
6-5 -0.372940667 -0.88054876  0.13466743 0.2554467
```

Col3a1

```
>col3a1=c(1,0.972,1.017,0.767,1,0.955,1,0.811,1.234,1,0.843,2.027,1.552,1.419,1.8883,1.009,1.
416,1.347,2.668,2.191,2.686,1.829,1.797,1.958,2.29,1.94,1.328,2.874,2.628,2.883,2.553,2.337,3.
191,2.617);
>  time=c(rep(1,11),rep(2,7),rep(3,3),rep(4,6),rep(5,3),rep(6,4));
> time=as.factor(time);
>  TukeyHSD(aov(col3a1~time),conf.level=0.95);
  Tukey multiple comparisons of means
    95% family-wise confidence level
```

Fit: aov(formula = col3a1 ~ time)

$time

	diff	lwr	upr	p adj
2-1	0.5590688	0.1690900	0.9490476	0.0018925
3-1	1.5514545	1.0260943	2.0768148	0.0000000
4-1	0.8934545	0.4840972	1.3028119	0.0000043
5-1	1.8314545	1.3060943	2.3568148	0.0000000
6-1	1.7109545	1.2400104	2.1818987	0.0000000
3-2	0.9923857	0.4357892	1.5489822	0.0001098
4-2	0.3343857	-0.1143567	0.7831282	0.2366612
5-2	1.2723857	0.7157892	1.8289822	0.0000019
6-2	1.1518857	0.6463318	1.6574396	0.0000020
4-3	-0.6580000	-1.2283417	-0.0876583	0.0166656
5-3	0.2800000	-0.3785739	0.9385739	0.7829304
6-3	0.1595000	-0.4565394	0.7755394	0.9667357
5-4	0.9380000	0.3676583	1.5083417	0.0003411
6-4	0.8175000	0.2968516	1.3381484	0.0006265
6-5	-0.1205000	-0.7365394	0.4955394	0.9903398

TGF-beta

>tgfbeta=c(1,1.004,1.059,0.613,1,1.0798,1,0.745,1.096,1,0.735,0.245,0.525,0.333,0.385,0.5501,
0.667,0.784,0.6824,1.107,0.793,0.973,0.85,0.587,0.75778,0.502,0.445,0.241,0.348,0.548,0.336,0
.518,0.4035,0.9699,0.7066,0.722,0.305,0.341,0.422,0.3755);
> time=c(rep(1,11),rep(2,6),rep(3,8),rep(4,8),rep(5,3),rep(6,4));
> time=as.factor(time);
> TukeyHSD(aov(tgfbeta~time),conf.level=0.95);
Tukey multiple comparisons of means
95% family-wise confidence level

Fit: aov(formula = tgfbeta ~ time)

$time

	diff	lwr	upr	p adj
2-1	-0.4884045	-0.70833678	-0.26847231	0.0000015
3-1	-0.1224820	-0.32384142	0.07887733	0.4574023
4-1	-0.5215670	-0.72292642	-0.32020767	0.0000001
5-1	-0.1397545	-0.42201072	0.14250163	0.6699822
6-1	-0.5783795	-0.83140003	-0.32535906	0.0000009
3-2	0.3659225	0.13188805	0.59995695	0.0005275
4-2	-0.0331625	-0.26719695	0.20087195	0.9980146
5-2	0.3486500	0.04222697	0.65507303	0.0181286

6-2 -0.0899750 -0.36969967 0.18974967 0.9239981
4-3 -0.3990850 -0.61575880 -0.18241120 0.0000448
5-3 -0.0172725 -0.31065021 0.27610521 0.9999730
6-3 -0.4558975 -0.72126763 -0.19052737 0.0001351
5-4 0.3818125 0.08843479 0.67519021 0.0049207
6-4 -0.0568125 -0.32218263 0.20855763 0.9864718
6-5 -0.4386250 -0.76959970 -0.10765030 0.0040418

Alpha-SMA

>alphasma=c(1,1.0613,1.2332,0.84556,1,1.465,1,0.6114,0.8978,1,0.712,3.24,2.965,2.993,9.91,8.
119,10.802,1.13,0.899,1.507,0.938,0.909,3.022,2.8597,2.727,3.944,4.138,3.554);
> time=c(rep(1,11),rep(2,3),rep(3,3),rep(4,3),rep(5,5),rep(6,3));
> time=as.factor(time);
> TukeyHSD(aov(alphasma~time),conf.level=0.95);
  Tukey multiple comparisons of means
    95% family-wise confidence level

Fit: aov(formula = alphasma ~ time)

$time
         diff   lwr   upr   p adj
2-1 2.0817945   0.7644552 3.3991339 0.0007959
3-1 8.6261279   7.3087885 9.9434673 0.0000000
4-1 0.1944612 -1.1228782 1.5118006 0.9970660
5-1 1.1069345   0.0160739 2.1977952 0.0453819
6-1 2.8944612   1.5771218 4.2118006 0.0000096
3-2 6.5443333   4.8929610 8.1957057 0.0000000
4-2 -1.8873333 -3.5387057 -0.2359610 0.0189847
5-2 -0.9748600 -2.4518923 0.5021723 0.3448547
6-2 0.8126667 -0.8387057 2.4640390 0.6478785
4-3 -8.4316667 -10.0830390 -6.7802943 0.0000000
5-3 -7.5191933 -8.9962256 -6.0421610 0.0000000
6-3 -5.7316667 -7.3830390 -4.0802943 0.0000000
5-4 0.9124733 -0.5645590 2.3895056 0.4144502
6-4 2.7000000   1.0486277 4.3513723 0.0005324
6-5 1.7875267   0.3104944 3.2645590 0.0118167

Anti-TGFb and losartan (1: initial, 2: control, 3: ctrl+antiTGFb, 4: flow+antiTGFb, 5: ctrl+los., 6:flow+los.)- Figure 4.18

Post-hoc Tukey tests after one way ANOVAs

Col1a1

```
>col1a1=c(1,1.082,1.4075,1,1.1578,1,0.684,1.494,1,1.017,1.7566,1.631,1.3775,1.118,0.966,0.89
7,1.188,1.218,1.166,1.338,1.535,1.07,1.26,1.105,1.365,1.302,0.937,0.959,1.002,0.856,1.123,1.14
8,1.492,0.851,1.7966,1.748);
> time=c(rep(1,10),rep(2,11),rep(3,6),rep(4,3),rep(5,3),rep(6,3));
> time=as.factor(time);
> TukeyHSD(aov(col1a1~time),conf.level=0.95);
  Tukey multiple comparisons of means
    95% family-wise confidence level

Fit: aov(formula = col1a1 ~ time)

$time
          diff       lwr       upr     p adj
2-1  0.20587000 -0.1364277 0.5481677 0.4631918
3-1  0.08893667 -0.3156159 0.4934893 0.9840868
4-1 -0.14523000 -0.6609354 0.3704754 0.9538280
5-1  0.17010333 -0.3456021 0.6858087 0.9132110
6-1  0.38097000 -0.1347354 0.8966754 0.2470904
3-2 -0.11693333 -0.5145304 0.2806637 0.9448545
4-2 -0.35110000 -0.8613672 0.1591672 0.3178621
5-2 -0.03576667 -0.5460339 0.4745006 0.9999325
6-2  0.17510000 -0.3351672 0.6853672 0.8991278
4-3 -0.23416667 -0.7881231 0.3197898 0.7902696
5-3  0.08116667 -0.4727898 0.6351231 0.9975566
6-3  0.29203333 -0.2619231 0.8459898 0.6027020
5-4  0.31533333 -0.3243205 0.9549872 0.6672107
6-4  0.52620000 -0.1134538 1.1658538 0.1555334
6-5  0.21086667 -0.4287872 0.8505205 0.9134015
```

Col3a1

```
>col3a1=c(1,0.972,1.017,0.767,1,0.955,1,0.811,1.234,1,0.843,2.027,1.552,1.419,1.8883,1.009,1.
416,1.347,2.334,2.09,1.106,1.365,1.3016,2.01,1.271,1.502,1.588,1.36,1.239,1.529,1.322,1.319,1.
544,1.351,1.7,0.882);
> time=c(rep(1,7),rep(2,11),rep(3,5),rep(4,4),rep(5,6),rep(6,3));
> time=as.factor(time);
> TukeyHSD(aov(col3a1~time),conf.level=0.95);
  Tukey multiple comparisons of means
    95% family-wise confidence level

Fit: aov(formula = col3a1 ~ time)

$time
          diff        lwr       upr     p adj
2-1  0.36367662 -0.13815626 0.8655095 0.2655349
3-1  0.68060571  0.07285591 1.2883555 0.0211618
4-1  0.63403571 -0.01652158 1.2845930 0.0594788
5-1  0.42678571 -0.15066544 1.0042369 0.2466426
6-1  0.35228571 -0.36395429 1.0685257 0.6692948
3-2  0.31692909 -0.24288893 0.8767471 0.5287183
4-2  0.27035909 -0.33566169 0.8763799 0.7513685
5-2  0.06310909 -0.46366053 0.5898787 0.9990689
6-2 -0.01139091 -0.68743539 0.6646536 0.9999999
4-3 -0.04657000 -0.74283487 0.6496949 0.9999464
5-3 -0.25382000 -0.88231806 0.3746781 0.8196059
6-3 -0.32832000 -1.08631718 0.4296772 0.7732598
5-4 -0.20725000 -0.87723118 0.4627312 0.9324613
6-4 -0.28175000 -1.07448242 0.5109824 0.8850483
6-5 -0.07450000 -0.80842761 0.6594276 0.9995836
```

Tgf-beta

```
>tgfbeta=c(1,1.004,1.059,0.613,1,1.0798,1,0.745,1.096,1,0.735,0.245,0.525,0.333,0.385,0.5501,
0.667,0.6,0.474,0.427,0.4167,0.4526,0.417,0.549,0.510,0.672,0.689,0.45,0.516,0.685,0.72,0.527,
0.391,0.6,0.339);
> time=c(rep(1,11),rep(2,6),rep(3,6),rep(4,6),rep(5,3),rep(6,3));
> time=as.factor(time);
> TukeyHSD(aov(tgfbeta~time),conf.level=0.95);
  Tukey multiple comparisons of means
    95% family-wise confidence level

Fit: aov(formula = tgfbeta ~ time)

$time
          diff        lwr        upr     p adj
2-1 -0.488404545 -0.69473410 -0.28207499 0.0000009
```

3-1 -0.474704545 -0.68103410 -0.26837499 0.0000015
4-1 -0.374921212 -0.58125076 -0.16859166 0.0000771
5-1 -0.295254545 -0.56005333 -0.03045576 0.0220452
6-1 -0.495921212 -0.76072000 -0.23112243 0.0000485
3-2 0.013700000 -0.22101904 0.24841904 0.9999723
4-2 0.113483333 -0.12123570 0.34820237 0.6828164
5-2 0.193150000 -0.09432093 0.48062093 0.3412577
6-2 -0.007516667 -0.29498760 0.27995427 0.9999995
4-3 0.099783333 -0.13493570 0.33450237 0.7847610
5-3 0.179450000 -0.10802093 0.46692093 0.4205840
6-3 -0.021216667 -0.30868760 0.26625427 0.9999116
5-4 0.079666667 -0.20780427 0.36713760 0.9563017
6-4 -0.121000000 -0.40847093 0.16647093 0.7915500
6-5 -0.200666667 -0.53260951 0.13127618 0.4556610

Alpha-SMA

>alphasma=c(1,1.0613,1.2332,0.84556,1,1.465,1,0.6114,0.8978,1,0.712,3.24,2.965,2.993,1.477,
0.97,1.311,1.701,1.3171,1.06,1.371,1.626,1.3601,2.632,3.2268,2.764,3.4373,3.118,3.3771,4.07);
> time=c(rep(1,11),rep(2,3),rep(3,5),rep(4,4),rep(5,4),rep(6,3));
> time=as.factor(time);
> TukeyHSD(aov(alphasma~time),conf.level=0.95);
Tukey multiple comparisons of means
95% family-wise confidence level

Fit: aov(formula = alphasma ~ time)

$time
diff lwr upr p adj
2-1 2.0817945 1.5077428 2.6558463 0.0000000
3-1 0.3710145 -0.1043455 0.8463746 0.1913497
4-1 0.3700695 -0.1445228 0.8846619 0.2639715
5-1 2.0308195 1.5162272 2.5454119 0.0000000
6-1 2.5374945 1.9634428 3.1115463 0.0000000
3-2 -1.7107800 -2.3544205 -1.0671395 0.0000003
4-2 -1.7117250 -2.3848604 -1.0385896 0.0000006
5-2 -0.0509750 -0.7241104 0.6221604 0.9998898
6-2 0.4557000 -0.2639120 1.1753120 0.3938583
4-3 -0.0009450 -0.5921666 0.5902766 1.0000000
5-3 1.6598050 1.0685834 2.2510266 0.0000001
6-3 2.1664800 1.5228395 2.8101205 0.0000000
5-4 1.6607500 1.0375478 2.2839522 0.0000003
6-4 2.1674250 1.4942896 2.8405604 0.0000000
6-5 0.5066750 -0.1664604 1.1798104 0.2221292

shRNA (1: initial, 2: control+scmb, 3: flow+scmb, 4: control+AT1R, 5: flow+AT1R)- Figure 4.19

Post-hoc Tukey tests after one way ANOVAs

col1a1

```
>col1a1=c(1.043,1,0.821,1.664,1.9667,1.628,0.852,1.919,1.157,2.33,1.875,1.9225,1.132,1.851,1
.5852,1.375);
> time=c(rep(1,3),rep(2,3),rep(3,3),rep(4,3),rep(5,4));
> time=as.factor(time);
> TukeyHSD(aov(col1a1~time),conf.level=0.95);
  Tukey multiple comparisons of means
    95% family-wise confidence level

Fit: aov(formula = col1a1 ~ time)

$time
        diff        lwr       upr     p adj
2-1  0.7982333 -0.03936654 1.6358332 0.0640082
3-1  0.3546667 -0.48293320 1.1922665 0.6574672
4-1  1.0878333  0.25023346 1.9254332 0.0103489
5-1  0.5311333 -0.25236960 1.3146363 0.2512748
3-2 -0.4435667 -1.28116654 0.3940332 0.4650808
4-2  0.2896000 -0.54799987 1.1271999 0.7941475
5-2 -0.2671000 -1.05060293 0.5164029 0.8019700
4-3  0.7331667 -0.10443320 1.5707665 0.0957855
5-3  0.1764667 -0.60703627 0.9599696 0.9453213
5-4 -0.5567000 -1.34020293 0.2268029 0.2161338
```

Col3a1

```
>col3a1=c(1,1.107,1.186,1,1,1,0.837,2.723,3.071,4.208,1.209,2.70997,3.332,2.69,2.62,3.467,2.4
29,3.209,3.0357);
> time=c(rep(1,7),rep(2,3),rep(3,2),rep(4,3),rep(5,4));
> time=as.factor(time);
```

```
> TukeyHSD(aov(col3a1~time),conf.level=0.95);
  Tukey multiple comparisons of means
    95% family-wise confidence level

Fit: aov(formula = col3a1 ~ time)

$time
         diff       lwr        upr     p adj
2-1  2.3154286  1.2722608 3.358596392 0.0000597
3-1  0.9409136 -0.2711379 2.152965050 0.1670378
4-1  1.8620952  0.8189274 2.905263059 0.0005656
5-1  2.0166036  1.0690993 2.964107798 0.0000940
3-2 -1.3745150 -2.7544963 0.005466314 0.0511313
4-2 -0.4533333 -1.6876261 0.780959477 0.7810724
5-2 -0.2988250 -1.4534002 0.855750203 0.9243292
4-3  0.9211817 -0.4587996 2.301162981 0.2811910
5-3  1.0756900 -0.2334752 2.384855225 0.1323739
5-4  0.1545083 -1.0000669 1.309083536 0.9929367
```

TGFb

```
>tgfbeta=c(1,1.14,1,1.214,1,1,1.081,0.652,0.769,0.4353,0.8105,0.569,0.523,0.576,0.871,1.084,0.
599,0.559,0.505,0.56,0.539,0.469,0.668,0.568);
> time=c(rep(1,7),rep(2,7),rep(3,2),rep(4,4),rep(5,4));
> time=as.factor(time);
> TukeyHSD(aov(tgfbeta~time),conf.level=0.95);
  Tukey multiple comparisons of means
    95% family-wise confidence level

Fit: aov(formula = tgfbeta ~ time)

$time
          diff        lwr        upr     p adj
2-1 -0.44288571 -0.6078453 -0.2779261 0.0000013
3-1 -0.08464286 -0.3320822  0.1627965 0.8390401
4-1 -0.50639286 -0.6998251 -0.3129606 0.0000019
5-1 -0.50114286 -0.6945751 -0.3077106 0.0000023
3-2  0.35824286  0.1108035  0.6056822 0.0027911
4-2 -0.06350714 -0.2569394  0.1299251 0.8577177
5-2 -0.05825714 -0.2516894  0.1351751 0.8911913
4-3 -0.42175000 -0.6890151 -0.1544849 0.0011790
5-3 -0.41650000 -0.6837651 -0.1492349 0.0013424
5-4  0.00525000 -0.2129710  0.2234710 0.9999932
```

Alpha-SMA

```
>alphasma=c(1,1,1.2877,1,1,0.977,4.87,4.34,4.356,3.711,4.216,7.24,8.853,4.34,4.216,3.711,3.79
97,3.3975);
> time=c(rep(1,6),rep(2,5),rep(3,2),rep(4,3),rep(5,2));
> time=as.factor(time);
> TukeyHSD(aov(alphasma~time),conf.level=0.95);
  Tukey multiple comparisons of means
    95% family-wise confidence level

Fit: aov(formula = alphasma ~ time)

$time
        diff       lwr       upr     p adj
2-1  3.254483  2.442294  4.0666725 0.0000001
3-1  7.002383  5.907228  8.0975389 0.0000000
4-1  3.044883  2.096451  3.9933159 0.0000013
5-1  2.554483  1.459328  3.6496389 0.0000464
3-2  3.747900  2.625699  4.8701005 0.0000009
4-2 -0.209600 -1.189137  0.7699369 0.9587248
5-2 -0.700000 -1.822201  0.4222005 0.3343491
4-3 -3.957500 -5.181921 -2.7330788 0.0000012
5-3 -4.447900 -5.789186 -3.1066138 0.0000009
5-4 -0.490400 -1.714821  0.7340212 0.7178401
```

6.3.3 Effect of MSC injection on fibroblast phenotype

Message levels of adjacent fibroblasts (1: initial, 2: control, 3: hypoxia, 4: flow, 5: strain)

Post-hoc Tukey tests after one way ANOVAs

Col1a1

```
>col1a1=c(1,1,1,1.163,1,0.897,1,1.184,0.5256,0.543,0.578,0.336,0.32255,0.218,0.3568,0.541,0.
7046,0.238,0.2246,0.1495,0.4215,0.218,0.278,0.204,0.172,0.227,0.148,0.2155,0.328,0.197,0.403
,0.438,0.443,0.225);
> time=c(rep(1,8),rep(2,7),rep(3,7),rep(4,6),rep(5,6));
> time=as.factor(time);
> TukeyHSD(aov(col1a1~time),conf.level=0.95);
  Tukey multiple comparisons of means
    95% family-wise confidence level

Fit: aov(formula = col1a1 ~ time)

$time
```

	diff	lwr	upr	p adj
2-1	-0.61907857	-0.81598620	-0.422170945	0.0000000
3-1	-0.67375714	-0.87066477	-0.476849516	0.0000000
4-1	-0.82308333	-1.02855612	-0.617610542	0.0000000
5-1	-0.69150000	-0.89697279	-0.486027209	0.0000000
3-2	-0.05467857	-0.25804389	0.148686751	0.9339089
4-2	-0.20400476	-0.41567410	0.007664577	0.0630851
5-2	-0.07242143	-0.28409077	0.139247910	0.8556250
4-3	-0.14932619	-0.36099553	0.062343148	0.2683644
5-3	-0.01774286	-0.22941220	0.193926481	0.9991727
5-4	0.13158333	-0.08807632	0.351242987	0.4257841

Col3a1

>col3a1=c(1,1,1,1.054,1,1.027,1,1.069,0.74,0.755,0.4804,0.7778,0.48,0.676,0.308,0.45051,0.295,0.166,0.242,0.5134,0.122,0.3195,0.544,0.3174,0.428,0.35,0.367,0.889971);
> time=c(rep(1,8),rep(2,4),rep(3,4),rep(4,6),rep(5,6));
> time=as.factor(time);
> TukeyHSD(aov(col3a1~time),conf.level=0.95);
  Tukey multiple comparisons of means
    95% family-wise confidence level

Fit: aov(formula = col3a1 ~ time)

$time

	diff	lwr	upr	p adj
2-1	-0.3304500	-0.58626351	-0.07463649	0.0071135
3-1	-0.5401225	-0.79593601	-0.28430899	0.0000209
4-1	-0.7424333	-0.96803964	-0.51682702	0.0000000
5-1	-0.5360215	-0.76162781	-0.31041519	0.0000035
3-2	-0.2096725	-0.50506050	0.08571550	0.2546024
4-2	-0.4119833	-0.68163445	-0.14233222	0.0013299
5-2	-0.2055715	-0.47522262	0.06407962	0.1962204
4-3	-0.2023108	-0.47196195	0.06734028	0.2086726
5-3	0.0041010	-0.26555012	0.27375212	0.9999990
5-4	0.2064118	-0.03477146	0.44759512	0.1184695

TGF-beta

>tgfbeta=c(1,1,1,1,0.965,1.005,1,1.087,0.395,0.548,0.537,0.478,1.005,0.54,0.505,0.373,0.562,0.224,0.203,0.135,0.144,0.0924,0.2135,0.14412,0.447,0.478,0.574,0.488,0.419,0.387,0.4872,0.4213);
> time=c(rep(1,8),rep(2,9),rep(3,7),rep(4,4),rep(5,4));
> time=as.factor(time);
> TukeyHSD(aov(tgfbeta~time),conf.level=0.95);

```
  Tukey multiple comparisons of means
    95% family-wise confidence level

Fit: aov(formula = tgfbeta ~ time)

$time
          diff        lwr         upr     p adj
2-1 -0.45790278 -0.60921423 -0.30659133 0.0000000
3-1 -0.84197929 -1.00314223 -0.68081634 0.0000000
4-1 -0.51037500 -0.70106557 -0.31968443 0.0000002
5-1 -0.57850000 -0.76919057 -0.38780943 0.0000000
3-2 -0.38407651 -0.54100554 -0.22714747 0.0000010
4-2 -0.05247222 -0.23959817  0.13465372 0.9224597
5-2 -0.12059722 -0.30772317  0.06652872 0.3504739
4-3  0.33160429  0.13642626  0.52678231 0.0003030
5-3  0.26347929  0.06830126  0.45865731 0.0043122
5-4 -0.06812500 -0.28831550  0.15206550 0.8929961
```

Alpha-SMA

```
>
alphasma=c(1,1,1,1,1.011,1.423,1,1.0404,0.8,0.932,0.627,0.613,0.8677,0.606,0.698,0.755,0.133,
0.496224,1.165,0.7,1.2485,0.75868,0.898,0.7466,0.493);
> time=c(rep(1,8),rep(2,6),rep(3,4),rep(4,4),rep(5,3));
> time=as.factor(time);
> TukeyHSD(aov(alphasma~time),conf.level=0.95);
  Tukey multiple comparisons of means
    95% family-wise confidence level

Fit: aov(formula = alphasma ~ time)

$time
          diff        lwr         upr     p adj
2-1 -0.31835000 -0.64363614  0.006936138 0.0569316
3-1 -0.53874400 -0.90758381 -0.169904189 0.0024427
4-1 -0.09125500 -0.46009481  0.277584811 0.9442807
5-1 -0.34676667 -0.75453442  0.061001087 0.1200690
3-2 -0.22039400 -0.60918530  0.168397298 0.4582253
4-2  0.22709500 -0.16169630  0.615886298 0.4292398
5-2 -0.02841667 -0.45431619  0.397482861 0.9996127
4-3  0.44748900  0.02158947  0.873388528 0.0365239
5-3  0.19197733 -0.26804673  0.652001401 0.7238910
5-4 -0.25551167 -0.71553573  0.204512401 0.4778841
```

Bibliography

Ahamed J, et al. In vitro and in vivo evidence for shear-induced activation of latent transforming growth factor-beta1. Blood (2008) 112:3650-3660.

Aikawa Y, et al. Regional wall stress predicts ventricular remodeling after anteroseptal myocardial infarction in the Healing and Early Afterload Reducing Trial (HEART): An echocardiographybased structural analysis. Am Heart J (2001) 141:234-42.

Alemu Y, Girdhar G, Xenos M, Sheriff J, Jesty J, Einav S, Bluestein D. Design optimization of a mechanical heart valve for reducing valve thrombogenicity-A case study with ATS valve. ASAIO J. (2010) 56(5):389-96.

Amin P, Singh M, Singh K.J. β-Adrenergic Receptor-Stimulated Cardiac Myocyte Apoptosis: Role of β1 Integrins. Signal Transduct. (2011) 2011:179057.

Arts T, Costa KD, Covell JW, McCulloch AD. Relating myocardial laminar architecture to shear strain and muscle fiber orientation. Am J Physiol Heart Circ Physiol. (2001) 280: H2222–H2229.

Ashikaga T, et al. Changes in regional myocardial volume during the cardiac cycle: implications for transmural blood flow and cardiac structure Am J Physiol Heart Circ Physiol. (2008) 295:610-618.

Atance J, et al. Influence of the Extracellular Matrix on the Regulation of Cardiac Fibroblast Behavior by Mechanical Stretch. J Cell Phys. (2004) 200:377–386.

Avitabile, Crespi A, Brioschi C, Parente V, Toietta G, Devanna P, Baruscotti M, Truffa S, Scavone A, Rusconi F, Biondi A, D'Alessandra Y, Vigna E, Difrancesco D, Pesce M, Capogrossi MC, Barbuti A. Human cord blood CD34+ progenitor cells acquire functional cardiac properties through a cell fusion process. Am J Physiol Heart Circ. (2011) 300(5):H1875-84.

Baker DW, Einstadter D, Thomas C, Cebul RD. Mortality trends for 23,505 Medicare patients hospitalized with heart failure in Northeast Ohio, 1991 to 1997. Am Heart J (2003) 146: 258–64.

Banerjee I, et al. Dynamic Interactions between Myocytes, Fibroblasts, and Extracellular Matrix. Ann. N.Y. Acad. Sci. (2006) 1080: 76–84.

Bangalore S, Messerli FH, Kostis JB, Pepine CJ. Cardiovascular protection using beta-blockers: a critical review of the evidence J Am Coll Cardiol (2007) 50:563-572.

Barallobre-Barreiro J, de Ilárduya OM, Moscoso I, Calviño-Santos R, Aldama G, Centeno A, López-Pelaez E, Doménech N.. Gene expression profiles following intracoronary injection of mesenchymal stromal cells using a porcine model of chronic myocardial infarction. Cytotherapy (2011) 13(4): 407-418.

Barasch E, Gottdiener JS, Aurigemma G, Kitzman DW, Han J, Kop WJ, Tracy RP. Association between elevated fibrosis markers and heart failure in the elderly. Circulation: Heart Failure (2009) 2:303-310.

Barone FC, Campbell WG Jr, Nelson AH, Feuerstein GZ. Carvedilol prevents severe hypertensive cardiomyopathy and remodeling. J Hypertens. (1998) 6:871-84.
Baxter S, Morales M, Goldsmith E. Adaptive Changes in Cardiac Fibroblast Morphology and Collagen Organization as a Result of Mechanical Environment. Cell Biochem Biophys. (2008) 51:33–44.

Baudino T, Carver W, Giles W, Borg T. Cardiac fibroblasts: friend or foe?, Am J Physiol Heart Circ Physiol. (2006) 291:H1015-H1026.

Boudoulas KD, Hatzopoulos AK. Cardiac repair and regeneration: the Rubik's cube of cell therapy for heart disease. Dis Model Mech. (2009) 2(7-8):344-58.

Breitbach M, et al. Potential risks of bone marrow cell transplantation into infarcted hearts. Blood (2007) 110: 1362-1369.

Brown M, Iyer R, Radisic M. Pulsatile Perfusion Bioreactor for Cardiac Tissue Engineering. Biotechnol. Prog. (2008) 24: 907-920.

Brown R, et al. Enhanced Fibroblast Contraction of 3D Collagen Lattices and Integrin Expression by TGF-beta1 and -beta3: Mechanoregulatory Growth Factors? Experimental Cell Research (2002) 274:310–322.

Bupha-Intr T, Holmes J, Janssen P. Induction of hypertrophy in vitro by mechanical loading in adult rabbit myocardium. Am J Physiol Heart Circ Physiol. (2007) 293: H3759–H3767.

Butt RP, Bishop JE. Mechanical Load Enhances the Stimulatory Effect of Serum Growth Factors on Cardiac Fibroblast Procollagen Synthesis. J Mol Cell Cardiol. (1997) 29: 1141–1151.

Cavallari LH, Momary KM, Groo VL, Viana MA, Camp JR, Stamos TD. Association of beta-blocker dose with serum procollagen concentrations and cardiac response to spironolactone in patients with heart failure. Pharmacotherapy. (2007) 27(6):801-12.

Chee Ping N, Swartz MA. Fibroblast alignment under interstitial fluid flow using a novel 3-D tissue culture model. Am J Physiol Heart Circ Physiol. (2003) 284: H1771.

Chee Ping N, Hinz B, Swartz MA. Interstitial fluid flow induces myofibroblast differentiation and collagen alignment in vitro. J Cell Science (2005) 118: 4731.

Chen JB, Tao R, Sun HY, Tse HF, Lau CP, Li GR. Multiple Ca2+ signaling pathways regulate intracellular Ca2+ activity in human cardiac fibroblasts. J Cell Physiol. 2010 Apr;223(1):68-75.

Chen K, et al. Transforming Growth Factor beta Receptor Endoglin Is Expressed in Cardiac Fibroblasts and Modulates Profibrogenic Actions of Angiotensin II. Circ Res. (2004) 95:1167-1173.

Chilton L, et al. K_ currents regulate the resting membrane potential, proliferation, and contractile responses in ventricular fibroblasts and myofibroblasts. Am J Physiol Heart Circ Physiol. (2005) 288: H2931–H2939.

Cucoranu I, et al. NAD(P)H Oxidase 4 Mediates Transforming Growth Factor-beta1–Induced Differentiation of Cardiac Fibroblasts Into Myofibroblasts. Circ Res. (2005) 97:900-907.

Desai RV, Guichard JL, Mujib M, Ahmed MI, Feller MA, Fonarow GC, Meyer P, Iskandrian AE, Bogaard HJ, White M, Aban IB, Aronow WS, Deedwania P, Waagstein F, Ahmed A. Reduced right ventricular ejection fraction and increased mortality in chronic systolic heart failure patients receiving beta-blockers: Insights from the BEST trial. Int J Cardiol. 2011 Jun 23. [Epub ahead of print]

Díez J, Laviades C, Varo N, Querejeta R, López B. Biochemical diagnosis of hypertensive myocardial fibrosis. Rev Esp Cardiol. (2000) 53(1):8-13.

Discher DE, Mooney DJ, Zandstra PW. Growth Factors, Matrices, and Forces Combine and Control Stem Cells, Science (2009) 324:1673-1676.

Doyle AM, Nerem RM, Ahsan T. Human Mesenchymal Stem Cells Form Multicellular Structures in Response to Applied Cyclic Strain. Ann Biomed Eng (2009) 37(4): 783-793.

Drakos SG, Kfoury AG, Hammond EH, Reid BB, Revelo MP, Rasmusson BY, Whitehead KJ, Salama ME, Selzman CH, Stehlik J, Clayson SE, Bristow MR, Renlund DG, Li DY. Impact of mechanical unloading on microvasculature and associated central remodeling features of the failing human heart. J Am Coll Cardiol. (2010) 56(5):382-91.

Drobic V, et al. Differential and combined effects of cardiotrophin-1 and TGF-beta1 on cardiac myofibroblast proliferation and contraction. Am J Physiol Heart Circ Physiol. (2007) 293: H1053–H1064.

Dvir Tal, et al. Activation of the ERK1/2 Cascade via Pulsatile Interstitial Fluid Flow Promotes Cardiac Tissue Assembly. Tissue Engineering (2007) 13(9), 2007.

Duty A, Oest M, Guldberg R. Cyclic Mechanical Compression Increases Mineralization of Cell-Seeded Polymer Scaffolds In Vivo. J Biomech Engrg. (2007) 129:531-539.

Engelmayr G, Sales V, Mayer J, Sacks M. Cyclic flexure and laminar flow synergistically accelerate mesenchymal stem cell-mediated engineered tissue formation: Implications for engineered heart valve tissues. Biomaterials (2006) 27:6083–6095.

Essick EE, Sam F. Cardiac hypertrophy and fibrosis in the metabolic syndrome: a role for aldosterone and the mineralocorticoid receptor. Int J Hypertens. (2011) 2011:346985.

Farng E, et al. The Effects of GDF-5 and Uniaxial Strain on Mesenchymal Stem Cells in 3-D Culture. Clin Orthop Relat Res. (2008) 466:1930–1937.

Flack EC, et al. Alterations in cultured myocardial fibroblast function following the development of left ventricular failure. Journal of Molecular and Cellular Cardiology (2006) 40: 474–483.

Fujita K, et al. Adiponectin Protects Against Angiotensin II–Induced Cardiac Fibrosis Through Activation of PPAR-alpha. Arterioscler Thromb Vasc Biol. (2008) 28:863-870.
Olson E, et al. Angiotensin II–Induced Extracellular Signal–Regulated Kinase 1/2 Activation Is Mediated by Protein Kinase C and Intracellular Calcium in Adult Rat Cardiac Fibroblasts. Hypertension. (2008) 51:704-711.

Fuseler JW, et al. Fractal and Image Analysis of Morphological Changes in the Actin Cytoskeleton of Neonatal Cardiac Fibroblasts in Response to Mechanical Stretch. Microsc. Microanal. (2007) 13:133–143.

Germain P, Roul G, Baruthio J, Jahn C, Coulbois PM, Dumitresco B, Dietemann JL, Bareiss P, Constantinesco A. Myocardial flow reserve parametric map, assessed by first-pass MRI compartmental analysis at the chronic stage of infarction. J Magn Reson Imaging (2001) 13(3): 352-360.

Gnecchi M, Zhang Z, Ni A, Dzau VJ. Paracrine Mechanisms in Adult Stem Cell Signaling and Therapy. Circulation Research. (2008) 103:1204-1219.

Goldsmith E, et al. Organization of Fibroblasts in the Heart. Developmental dynamics (2004) 230:787–794.

Gregory SD, Timms D, Gaddum N, Mason DG, Fraser JF. Biventricular Assist Devices: A Technical Review. Ann Biomed Eng. 2011 Jul 8. [Epub ahead of print]

Gudi S, et al. Equibiaxial strain and strain rate stimulate early activation of G proteins in cardiac fibroblasts. Am. J. Physiol. (1998) 274: C1424–C1428.

Gyöngyösi M, Hemetsberger R, Posa A, Charwat S, Pavo N, Petnehazy O, Petrasi Z, Pavo IJ, Hemetsberger H, Benedek I, Benedek T, Benedek I Jr, Kovacs I, Kaun C, Maurer G. Hypoxia-inducible factor 1-alpha release after intracoronary versus intramyocardial stem cell therapy in myocardial infarction. J Cardiovasc Transl Res. (2010) 3(2): 114-121.

Gyöngyösi M, Hemetsberger R, Wolbank S, Pichler V, Kaun C, Posa A, Petrasi Z, Petnehazy O, Hofer-Warbinek R, de Martin R, Gruber F, Benedek I, Benedek T, Kovacs I, Benedek I Jr, Plass CA, Charwat S, Maurer G. Delayed Recovery of Myocardial Blood Flow After Intracoronary Stem Cell Administration. Stem Cell Rev. (2011) 7(3):616-23.

Hamilton D, Maul T, Vorp D. Characterization of the Response of Bone Marrow-Derived Progenitor Cells to Cyclic Strain: Implications for Vascular Tissue-Engineering Applications. Tissue Engineering (2004) 10(3/4).

Habashi JP, Doyle JJ, Holm TM, Aziz H, Schoenhoff F, Bedja D, Chen Y, Modiri AN, Judge DP, Dietz HC. Angiotensin II Type 2 Receptor Signaling Attenuates Aortic Aneurysm in Mice Through ERK Antagonism, Science (2011) 332(6027): 361-365.

Harrington K, et al. Direct measurement of transmural laminar architecture in the anterolateral wall of the ovine left ventricle: new implications for wall thickening mechanics. Am J Physiol Heart Circ Physiol. (2005) 288:1324-1330.

Herrmann HJ, Fiedler U, Blodner R. Pathogenesis of myocardial fibrosis in spontaneously hypertensive rats (SHR) Eur Heart J (1995) 16 (2): 243-252.

Holmes J, Borg T, Covell J. Structure and mechanics of healing myocardial infarcts. Annu. Rev. Biomed. Eng. (2005) 7: 223–253.

Hu BS, et al. An analysis of the effects of stretch on IGF-I secretion from rat ventricular fibroblasts. Am J Physiol Heart Circ Physiol. (2007) 293: H677–H683.

Hu X, Wei L, Taylor TM, Wei J, Zhou X, Wang JA, Ping Yu S. Hypoxic preconditioning enhances bone marrow mesenchymal stem cell migration via Kv2.1 channel and FAK activation. Am J Physiol Cell Physiol. (2011) 31(2):C362-72.

Hu X, Yu SP, Fraser JL, Lu Z, Ogle ME, Wang JA, Wei L. Transplantation of hypoxia-preconditioned mesenchymal stem cells improves infarcted heart function via enhanced survival of implanted cells and angiogenesis. J Thoracic Cardiovasc Surgery (2008) 135(4): 799-808.

Husse B, et al. Cyclical mechanical stretch modulates expression of collagen I and collagen III by PKC and tyrosine kinase in cardiac fibroblasts. Am J Physiol Regul Integr Comp Physiol (2007) 293: R1898–R1907.

Kawano H, et al. Angiotensin II Enhances Integrin and alpha-Actinin Expression in Adult Rat Cardiac Fibroblasts. Hypertension (2000) 35(2):273-279.

Klapholz M. Beta-blocker Use for the Stages of Heart Failure. Mayo Clinic Proceedings (2009) 84(8): 718-729.

Kobayashi N, et al. Mechanical stress promotes the expression of smooth muscle-like properties in marrow stromal cells. Experimental Hematology (2004) 32:1238–1245.

Konstam MA, Neaton JD, Dickstein K, Drexler H, Komajda M, Martinez FA, Riegger GAJ, Malbecq W, Smith RD, Guptha S, Poole-Wilson PA. Effects of high-dose versus low-dose losartan on clinical outcomes in patients with heart failure (HEAAL study): a randomised, double-blind trial, Lancet (2004) 374(9704): 1840-1848.

Lal H, et al. Stretch-induced regulation of angiotensinogen gene expression in cardiac myocytes and fibroblasts: Opposing roles of JNK1/2 and p38α MAP kinases. Journal of Molecular and Cellular Cardiology (2008) 45:770–778.

Lee A, et al. Differential Responses of Adult Cardiac Fibroblasts to in vitro Biaxial Strain Patterns. J Mol Cell Cardiol. (1999) 31:1833–1843.

Lee D, et al. Magnetic Resonance Versus Radionuclide Pharmacological Stress Perfusion Imaging for Flow-Limiting Stenoses of Varying Severity. Circulation (2004) 110:58-65.

LeGrice IJ, Takayama Y, Covell JW. Transverse Shear Along Myocardial Cleavage Planes Provides a Mechanism for Normal Systolic Wall Thickening. Circulation Research (1995) 77:182-193.

LeGrice IJ, et al. Laminar structure of the heart: ventricular myocyte arrangement and connective tissue architecture in the dog. Am. J. Physiol. (1995) 269: H571-H582.

Leicht M, et al. Serum depletion induces cell loss of rat cardiac fibroblasts and increased expression of extracellular matrix proteins in surviving cells. Cardiovascular Research (2001) 52:429–437.

Leicht M, et al. Mechanism of cell death of rat cardiac fibroblasts induced by serum depletion. Molecular and Cellular Biochemistry (2003) 251: 119–126.

Leosco D, Rengo G, Iaccarino G, Filippelli A, Lymperopoulos A, Zincarelli C, Fortunato F, Golino L, Marchese M, Esposito G, Rapacciuolo A, Rinaldi B, Ferrara N, Koch WJ, Rengo F. Exercise training and beta-blocker treatment ameliorate age-dependent impairment of beta-adrenergic receptor signaling and enhance cardiac responsiveness to adrenergic stimulation. Am J Physiol Heart Circ Physiol. (2007) 293(3):H1596-603.

Liang CS, Mao W, Liu J. Pro-apoptotic effects of anti-beta1-adrenergic receptor antibodies in cultured rat cardiomyocytes: actions on endoplasmic reticulum and the prosurvival PI3K-Akt pathway. Autoimmunity (2008) 41(6):434-41.

Liang F, et al. Integrin Dependence of Brain Natriuretic Peptide Gene Promoter Activation by Mechanical Strain. (2000) 275(27):20355–20360.

Lijnen P, et al. Transforming growth factor-beta1-mediated collagen gel contraction by cardiac fibroblasts. J Renin Angiotensin Aldosterone Syst. (2003) 4:113.

Liu X, et al. Smad3 Mediates the TGF-beta-Induced Contraction of Type I Collagen Gels by Mouse Embryo Fibroblasts. Cell Motility and the Cytoskeleton (2003) 54:248–253.

Lloyd-Jones D, Adams RJ, Brown TM, et al. Heart Disease and Stroke Statistics—2010 Update. A Report from the American Heart Association Statistics Committee and Stroke Statistics Subcommittee: Circulation. (2010) 121:e1-e170.

Lopez B, et al. Alterations in the Pattern of Collagen Deposition May Contribute to the Deterioration of Systolic Function in Hypertensive Patients With Heart Failure. Journal of the American College of Cardiology (2006) 48(1).
Lorenzen-Schmidt I, et al. Chronotropic response of cultured neonatal rat ventricular myocytes to short-term fluid shear. Cell Biochemistry and Biophysics (2006) 46(2).

Lu T, Pelacho B, Hao H, Luo M, Zhu J, Verfaillie CM, Tian J, Liu Z. Cardiomyocyte Differentiation of Rat Bone Marrow Multipotent Progenitor Cells Is Associated with Downregulation of Oct-4 Expression. Tissue Engineering Part A (2010) 16(10):3111-3117.

McMurray JVJ, Granger CB, Östergren J, Yusuf S, Pfeffer MAJ. Dual Renin-Angiotensin System Blockade in Heart Failure. Am. Coll. Cardiol. (2009) 54:278.

McMurray JVJ, Pfeffer MA. Heart Failure. Lancet (2005) 365:1877–89.

Mehlhom U, Geissler H, Laine G, Allen S. Myocardial Fluid Balance. European Journal of Cardio-thoracic Surgery (2001) 20: 1220–1230.

Meluzin J, Vlasín M, Groch L, Mayer J, Kren L, Rauser P, Tichý B, Hornácek I, Sitar J, Palsa S, Klabusay M, Korístek Z, Doubek M, Pospísilová S, Lexmaulová L, Dusek L. Intracoronary Delivery of Bone Marrow Cells to the Acutely Infarcted Myocardium. Cardiology (2009) 112:98–106.

Merryman WD, et al. Differences in Tissue-Remodeling Potential of Aortic and Pulmonary Heart Valve Interstitial Cells. Tissue Engineering (2007) 13.

Messerli FH. The Sudden Demise of Dual Renin-Angiotensin System Blockade or the Soft Science of the Surrogate End Point. J Am Coll Cardiol (2009) 53:468-470.

Mias C, Lairez O, Trouche E, Roncalli J, Calise D, Seguelas MH, Ordener C, Piercecchi-Marti MD, Auge N, Salvayre AN, Bourin P, Parini A, Cussac D. Mesenchymal stem cells promote matrix metalloproteinase secretion by cardiac fibroblasts and reduce cardiac ventricular fibrosis after myocardial infarction. Stem Cells (2009) 27(11):2734-43.

Miyahara Y, Nagaya N, Kataoka M, Yanagawa B, Tanaka K, Hao H, Ishino K, Ishida H, Shimizu T, Kangawa K, Sano S, Okano T, Kitamura S, Mori H. Monolayered mesenchymal stem cells repair scarred myocardium after myocardial infarction. Nature Medicine (2006) 12(4):459-465.

Moscato F, Danieli GA, Schima H. Dynamic modeling and identification of an axial flow ventricular assist device. Int J Artif Organs. (2009) 32(6):336-43.

Nagaya N, Kangawa K, Itoh T, Iwase T, Murakami S, Miyahara Y, Fujii T, Uematsu M, Ohgushi H, Yamagishi M, Tokudome T, Mori H, Miyatake K, Kitamura S. Model of Dilated Cardiomyopathy Transplantation of Mesenchymal Stem Cells Improves Cardiac Function in a Rat. Circulation. (2005) 112: 1128-1135.

Naugle J, et al. Type VI collagen induces cardiac myofibroblast differentiation: implications for postinfarction remodeling. Am J Physiol Heart Circ Physiol. (2006) 290: H323–H330.

Nanjo S, Yoshikawa K, Harada M, Inoue Y, Namiki A, Nakano H, Yamazaki. Correlation between left ventricular diastolic function and ejection fraction in dilated cardiomyopathy using magnetic resonance imaging with late gadolinium enhancement. J. Circ (2009) 73(10):1939-44.

Nappi JM, Sieg A. Aldosterone and aldosterone receptor antagonists in patients with chronic heart failure. Vasc Health Risk Manag. (2011) 7:353-63.

Neuvonen AM, Palo JU, Sajantila A. Post-mortem ABCB1 genotyping reveals an elevated toxicity for female digoxin users. Int J Legal Med. (2011) 125(2):265-9.

Ng CP, Hinz B, Swartz MA. Interstitial fluid flow induces myofibroblast differentiation and collagen alignment in vitro, Journal of Cell Science (2005) 118:4731-4739.

Novotny N, Ray R, Markel TA, Wang M, Wang Y, Meldrum DR. Stem Cell Therapy in Myocardial Repair and Remodeling. J Am Coll Surg. (2008) 207(3): 423-434.

O'Cearbhaill ED, et al. Response of mesenchymal stem cells to the biomechanical environment of the endothelium on a flexible tubular silicone substrate. Biomaterials (2008) 29:1610-1619.

Okada T, Nagai M, Taniguchi I, Kuno M, Imamoto S, Seki S, Taniguchi M, Mochizuki S. Combined treatment with valsartan and spironolactone prevents cardiovascular remodeling in renovascular hypertensive rats. Int Heart J. (2006) 47(5):783-93.

Packer M, Bristow MR, Cohn JN, Colucci WS, Fowler MB, Gilbert EM, et al. The effect of carvedilol on morbidity and mortality in patients with chronic heart failure. U.S. Carvedilol Heart Failure Study Group. N Engl J Med (1996) 334:1349-55.

Park J, et al. Differential Effects of Equiaxial and Uniaxial Strain on Mesenchymal Stem Cells. Biotechnology and Bioengineering. (2004) 88(3).

Perin EC, Dohmann HF, Borojevic R, Silva SA, Sousa AL, Mesquita CT, Rossi MI, Carvalho AC, Dutra HS, Dohmann HJ, Silva GV, Belém L, Vivacqua R, Rangel FO, Esporcatte R, Geng YJ, Vaughn WK, Assad JA, Mesquita ET, Willerson JT.. Transendocardial, autologous bone marrow cell transplantation for severe, chronic ischemic heart failure. Circulation (2003) 107(18):2294-2302.

Petrov V, et al. TGF-β1-induced cardiac myofibroblasts are nonproliferating functional cells carrying DNA damages. Experimental Cell Research (2008) 314: 1480 – 1494.

Prante C, et al. Transforming Growth Factor beta1-regulated Xylosyltransferase I Activity in Human Cardiac Fibroblasts and Its Impact for Myocardial Remodeling. JBC (2007) 282(36): 26441–26449,

Prinz C, Hering D, Bitter T, Horstkotte D, Faber L. Left atrial size and left ventricular hypertrophy correlate with myocardial fibrosis in patients with hypertrophic cardiomyopathy. Acta Cardiol. (2011) 66(2):153-7.

Poobalarahi F, et al. Cardiac myofibroblasts differentiated in 3D culture exhibit distinct changes in collagen I production, processing, and matrix deposition. Am J Physiol Heart Circ Physiol. (2006) 291: H2924–H2932.

Raizman JE, et al. The Participation of the Na+–Ca2+ Exchanger in Primary Cardiac Myofibroblast Migration, Contraction, and Proliferation. J. Cell. Physiol. (2007) 213: 540–551.

Ramanujan S, Pluen A, McKee TD, Brown EB, Boucher Y, Jain RK. Diffusion and Convection in Collagen Gels: Implications for Transport in the Tumor Interstitium. Biophysical Journal (2002) 83: 1650.

Rosenkranz S, et al. Alterations of β-adrenergic signaling and cardiac hypertrophy in transgenic mice overexpressing TGF-beta1. Am J Physiol Heart Circ Physiol. (2002) 283: H1253–H1262.

Roy S, et al. Oxygen Sensing by Primary Cardiac Fibroblasts: A Key Role of p21 Waf1/Cip1/Sdi1. Circ. Res. (2003) 92:264-271.

Roy S, et al. p21waf1/cip1/sdi1 as a Central Regulator of Inducible Smooth Muscle Actin Expression and Differentiation of Cardiac Fibroblasts to Myofibroblasts. Molecular Biology of the Cell Vol. (2007) 18: 4837–4846.

Schneider F, Fellner T, Wilde J, Wallrabe U. Mechanical properties of silicones for MEMS. J. Micromech. Microeng. (2009) 18:065008.

Scolletta S, Miraldi F, Romano SM, Muzzi L. Continuous cardiac output monitoring with an uncalibrated pulse contour method in patients supported with mechanical pulsatile assist device. Interact Cardiovasc Thorac Surg. (2011) 13(1):52-7.

Serpooshan V, Julien M, Nguyen O, Wang H, Li A, Muja N, Henderson JE, Nazhat SN. Reduced hydraulic permeability of three-dimensional collagen scaffolds attenuates gel contraction and promotes the growth and differentiation of mesenchymal stem cells. Acta Biomaterialia (2010) 6:3978.

Simpson D, Liu H, Fan TH, Nerem R, Dudley SC Jr. A Tissue Engineering Approach to Progenitor Cell Delivery Results in Significant Cell Engraftment and Improved Myocardial Remodeling. Stem Cells (2007) 25:2350–2357.

Sinay R, et al. Intramyocardial pressure: interaction of myocardial fluid pressure and fiber stress. Am J. Physiol. (1989) 257: H357-H364, 1989.

Song G, et al. Mechanical stretch promotes proliferation of rat bone marrow mesenchymal stem cells. Colloids and Surfaces B: Biointerfaces (2007) 58:271–277.

Stewart S, Jenkins A, Buchan S, et al. The current cost of heart failure to the National Health Service in the UK. Eur J Heart Fail (2002) 4: 361–71.

Sukumaran V, Watanabe K, Veeraveedu PT, Thandavarayan RA, Gurusamy N, Ma M, Yamaguchi K, Suzuki K, Kodama M, Aizawa Y. Telmisartan, an angiotensin-II receptor blocker ameliorates cardiac remodeling in rats with dilated cardiomyopathy. Hypertens Res. (2010) 33(7):695-702.

Sumanasinghe R, Bernacki S, Loboa E. Osteogenic Differentiation of Human Mesenchymal Stem Cells in Collagen Matrices: Effect of Uniaxial Cyclic Tensile Strain on Bone Morphogenetic Protein (BMP-2) mRNA Expression. Tissue Engineering (2006) 12(12): 3459-3465.

Sun M, et al. Tumor Necrosis Factor-alpha Mediates Cardiac Remodeling and Ventricular Dysfunction After Pressure Overload State. Circulation (2007) 115:1398-1407.

Swaney J, et al. Inhibition of cardiac myofibroblast formation and collagen synthesis by activation and overexpression of adenylyl cyclase. PNAS (2005) 102:2:437-442.

Tamura N, Ogawa Y, Chusho H, Nakamura K, Nakao K, Suda M, Kasahara M, Hashimoto R, Katsuura G, Mukoyama M, Itoh H, Saito Y, Tanaka I, Otani H, Katsuki M, Nakao K. Cardiac fibrosis in mice lacking brain natriuretic peptide. PNAS (2000) 97(8):4239-4244.

Tan S, et al. Viscoelastic behavior of human mesenchymal stem cells. BMC Cell Biology (2008) 9:40.

Tanaka T, et al. Marked Elevation of Brain Natriuretic Peptide Levels in Pericardial Fluid Is Closely Associated With Left Ventricular Dysfunction. JACC (1998) 31(2):399–403.

Teramoto N, Koshino K, Yokoyama I, Miyagawa S, Zeniya T, Hirano Y, Fukuda H, Enmi J, Sawa Y, Knuuti J, Iida H. Experimental pig model of old myocardial infarction with long survival leading to chronic left ventricular dysfunction and remodeling as evaluated by PET. J Nucl Med. (2011) 52(5):761-8.

Thibault G, et al. Upregulation of a8b1-integrin in cardiac fibroblast by angiotensin II and transforming growth factor-b1. Am J Physiol Cell Physiol. (2001) 281: C1457–C1467.

Vallakati A, Chandra PA, Pednekar M, Frankel R, Shani J. Dronedarone-Induced Digoxin Toxicity: New Drug, New Interactions. Am J Ther. 2011 Apr 23. [Epub ahead of print]

Voge CM, Kariolis M, MacDonald RA, Stegemann JP. Directional conductivity in SWNT-collagen-fibrin composite biomaterials through strain-induced matrix alignment. J Biomed Mat Res. (2008) 86A(1): 269.

Walcher T, Steinbach P, Spieß J, Kunze M, Gradinger R, Walcher D, Bernhardt P. Detection of long-term progression of myocardial fibrosis in Duchenne muscular dystrophy in an affected family: A cardiovascular magnetic resonance study. Eur J Radiol. 2010 Aug 2. [Epub ahead of print]

Wang B, Borazjani A, Tahai M, Curry AL, Simionescu DT, Guan J, To F, Elder SH, Liao J. Fabrication of cardiac patch with decellularized porcine myocardial scaffold and bone marrow mononuclear cells. J Biomed Mat Res A (2010) 94A(4):1100-1110.

Wang D, Tarbell J. Modeling interstitial flow in an artery wall allows estimation of wall shear stress on smooth muscle cells. Ann Biomed Eng. (1995) 117: 358–363.

Wang D, Zhang F, Shen W, Chen M, Yang B, Zhang Y, Cao K. Mesenchymal stem cell injection ameliorates the inducibility of ventricular arrhythmias after myocardial infarction in rats. J Cardiology 2010; epub ahead of print.

Wang H, et al. Shear Stress Induces Endothelial Differentiation From a Murine Embryonic Mesenchymal Progenitor Cell Line. Arterioscler. Thromb. Vasc. Biol. (2005) 25: 1817-1823.

Wang J, et al. Left Ventricular Twist Mechanics in a Canine Model of Reversible Congestive Heart Failure: A Pilot Study. J Am Soc Echocardiogr (2009) 22:95-98.

Wang J, et al. Force regulates smooth muscle actin in cardiac fibroblasts. Am J Physiol Heart Circ Physiol. (2000) 279: H2776–H2785.

Wang J, et al. Mechanical force activates eIF-2a phospho-kinases in fibroblast. Biochemical and Biophysical Research Communications (2005) 330:123–130.

Watanabe H, et al. Multiphysics Simulation of Left Ventricular Filling Dynamics Using Fluid-Structure Interaction Finite Element Method. Biophysical Journal (2004) 87: 2074–2085.

Wipff PJ, et al. Myofibroblast contraction activates latent TGF-β1 from the extracellular matrix. The Journal of Cell Biology (2007) 179(6):1311-1323.

Wu J, Paden BE, Borovetz HS, Antaki JF. Computational fluid dynamics analysis of blade tip clearances on hemodynamic performance and blood damage in a centrifugal ventricular assist device. Artif Organs. (2010) 34(5):402-11.

Zhang GE, Hu Q, Braunlin EA, Suggs LJ, Zhang J. Enhancing Efficacy of Stem Cell Transplantation to the Heart with a PEGylated Fibrin Biomatrix. Tissue Engineering: Part A. (2008) 14(6).

Zhao F, Grayson WL, Ma T, Irsigler A. Perfusion Affects the Tissue Developmental Patterns of Human Mesenchymal Stem Cells in 3D Scaffolds. J. Cell. Physiol. (2009) 219: 421–429.

Zhao XH, et al. Force activates smooth muscle -actin promoter activity through the Rho signaling pathway. Journal of Cell Science (2007) 120: 1801-1809.

Zhou X, Yun JL, Han ZQ, Gao F, Li H, Jiang TM, Li YM. Postinfarction healing dynamics in the mechanically unloaded rat left ventricle. Am J Physiol Heart Circ Physiol. (2011) 300(5):H1863-74.

Zlochiver S, Munoz V, Vikstrom K, Taffet S, Berenfeld O, Jalife J. Electrotonic myofibroblast-to-myocyte coupling increases propensity to reentrant arrhythmias in two-dimensional cardiac monolayers, Biophysical Journal (2008) 95:4469–4480.

Zou Y, Akazawa H, Qin Y, Sano M, Takano H, Minamino T, Makita N, Iwanaga K, Zhu W, Kudoh S, Toko H, Tamura K, Kihara M, Nagai T, Fukamizu A, Umemura S, Iiri T, Fujita T,

Komuro I. Mechanical stress activates anngiotensin II type 1 receptor without involvement of angiotensin II, Nature: Cell Biology (2004) 6(6):499-506.

NCT ID: NCT01150461

Cardiac Insufficiency Bisoprolol Study II (CIBIS-II): a randomised trial. Lancet (1999) 353:9-13.

Effect of metoprolol CR/XL in chronic heart failure: Metoprolol CR/XL Randomised Intervention Trial in Congestive Heart Failure (MERIT-HF). Lancet (1999) 353:2001-7.